Laser Cooling of a Magnetically Guided Ultra Cold Atom Beam

Von der Fakultät Mathematik und Physik der Universität Stuttgart
zur Erlangung der Würde eines Doktors der Naturwissenschaften
(Dr. rer. nat.) genehmigte Abhandlung

Vorgelegt von

Anoush Aghajani-Talesh

aus Rasht

Hauptberichter:	Prof. Dr. Tilman Pfau
Mitberichter:	Prof. Dr. Peter Michler
Tag der mündlichen Prüfung:	19. September 2013

5. Physikalisches Institut der Universität Stuttgart

2014

Thesis abstract

This thesis examines two complimentary methods for the laser cooling of a magnetically guided ultra-cold atom beam. If combined, these methods could serve as a starting point for high-through put and possibly even continuous production of Bose-Einstein condensates.

First, a mechanism is outlined to harvest ultra cold atoms from a magnetically guided atom beam into an optical dipole trap. A continuous loading scheme is described that dissipates the directed kinetic energy of a captured atom via deceleration by a magnetic potential barrier followed by optical pumping to the energetically lowest Zeeman sublevel. The application of this scheme to the transfer of ultra cold chromium atoms from a magnetically guided atom beam into a deep optical dipole trap is investigated via numerical simulations of the loading process. Based on the results of the theoretical studies the feasibility and the efficiency of our loading scheme, including the realisation of a suitable magnetic field configuration, are analysed.

Second, experiments were conducted on the transverse laser cooling of a magnetically guided beam of ultra cold chromium atoms. Radial compression by a tapering of the guide is employed to adiabatically heat the beam. Inside the tapered section heat is extracted from the atom beam by a two-dimensional optical molasses perpendicular to it, resulting in a significant increase of atomic phase space density. A magnetic offset field is applied to prevent optical pumping to untrapped states. Our results demonstrate that by a suitable choice of the magnetic offset field, the cooling beam intensity and detuning, atom losses and longitudinal heating can be avoided. Final temperatures below 65 μK have been achieved, corresponding to an increase of phase space density in the guided beam by more than a factor of 30.

Zusammenfassung der Arbeit

In dieser Dissertation werden zwei komplementäre Methoden für die Laserkühlung eines magnetisch geführten, ultrakalten Atomstrahls untersucht. Kombiniert könnten diese Methoden den Ausgangspunkt für eine, möglicherweise sogar kontinuierliche, Hochdurchsatzproduktion von Bose-Einstein-Kondensaten darstellen.

Als erstes wird ein Mechanismus vorgestellt, mit dem sich ultrakalte Atome aus einem magnetisch geführten Atomstrahl in eine optische Dipolfalle umladen lassen. Es wird ein kontinuierliches Ladeschema beschrieben, das die Dissipation der gerichteten kinetischen Energie eines eingefangenen Atoms durch Abbremsung an einer magnetischen Potentialbarriere, gefolgt von optischen Umpumpen in den energetisch niedrigsten Zeeman-Zustand, ermöglicht. Die Anwendung dieses Ladeschemas auf den Transfer von ultrakalten Chromatomen aus einem magnetisch geführten Atomstrahl in eine tiefe optische Dipolfalle wird mittels numerischer Simulationen untersucht. Basierend auf den Ergebnissen der theoretischen Untersuchungen wird die Machbarkeit und die zu erwartende Effizienz des Ladeschemas, sowie die Realisierung einer geeigneten Magnetfeldkonfiguration analysiert.

Als zweites wurde die transversale Laserkühlung eines magnetisch geführten ultrakalten Chromatomstrahls im Experiment untersucht. Hierfür wurde der Atomstrahl durch eine Verjüngung der magnetischen Strahlführung radial komprimiert und so adiabatisch erwärmt. Inmitten des verjüngten Strahlabschnitts wurde senkrecht zum Strahl eine zweidimensionale optische Molasse erzeugt, welche Wärme aus dem Strahl extrahierte, was zu einem signifikanten Anstieg der atomaren Phasenraumdichte führte. Durch das Anlegen eines magnetischen Offsetfeldes wird optischen Pumpen in magnetisch nicht einschließbare Zustände verhindert. Unsere Ergebnisse zeigen, das Atomverluste und eine longitudinale Aufheizung durch geeignet gewählte Werte des magnetisches Offsetfeldes, der Kühlstrahlintensität und -verstimmung verhindert werden können. Es konnten Endtemperaturen unter 65 µK erreicht werden, was einem Anstieg der Phasenraumdichte im geführten Strahl um mehr als einen Faktor 30 entspricht.

Acknowledgements

It would not have been possible to write this dissertation without the help and the encouragement from a great number of individuals to whom I am greatly indebted.

First of all I would like to express my deepest appreciations to Prof. Dr. Tilman Pfau for his guidance, support and enthusiasm throughout this challenging project in his role as my doctoral advisor and as the head of 5. Physikalisches Institut. I also wish to convey my utmost gratitude to Prof. Dr. Peter Michler for reviewing my thesis manuscript as second referee, and to Prof. Dr. Günter Wunner, for kindly acting as the Chairman of my doctoral examination committee.

I am extremely grateful to my colleagues, the academic and the administrative staff at 5. Physikalisches Institut for their assistance and cooperation in overcoming the everyday obstacles big and small that come with an academic project of this scale. In particular, I would like to mention the members of the chromium atom guide project: Axel Griesmaier, who joined the experiment as a Postdoc, and fellow doctoral students Markus Falkenau, Valentin Volchkov, Paul Rehme, Jimmy Sebastian und Alexander Greiner.

I owe very special and heartfelt thanks to my family and to my beloved Nicola for their support and affection throughout the last years, as well as to my friends Björn and Johannes for providing valuable feedback and sharing their time and ideas with me during the final stages of my work.

Finally, I would like to gratefully acknowledge financial support in the form of dissertation fellowships from Studienstiftung des Deutschen Volkes and Landesgraduiertenförderung Baden-Württemberg.

Contents

Thesis abstract 3

Zusammenfassung der Arbeit 5

Acknowledgements 7

1 Introduction 11
- 1.1 Effusive atom beams 11
- 1.2 Laser cooled atom beams 13
- 1.3 Quantum degenerate atom beams 14
- 1.4 Magnetically guided ultra cold atom beams 14
- 1.5 Laser cooling of a magnetically guided ultra cold atom beam 15
- 1.6 Thesis outline 16

2 Physical preliminaries 17
- 2.1 Spectroscopic properties of Cr-52 17
  - 2.1.1 Nuclear properties 17
  - 2.1.2 Electronic configuration of the ground state 18
  - 2.1.3 Important optical transitions 18
  - 2.1.4 Zeeman splitting in an external magnetic field 19
- 2.2 Laser cooling and trapping of Cr-52 20
  - 2.2.1 The definition of temperature in laser cooling 20
  - 2.2.2 Magnetic forces for guiding and trapping 21
  - 2.2.3 Magnetic quadrupole guide for atoms 21
  - 2.2.4 The radiation scattering force 22
  - 2.2.5 Optical pumping and stretched states 23
  - 2.2.6 Zeeman slowing of an atom beam 25
  - 2.2.7 Doppler cooling and optical molasses 28
  - 2.2.8 Magneto-optical trap 31
  - 2.2.9 The optical dipole force 33
  - 2.2.10 Optical trapping of Cr-52 35

3 Experimental apparatus and methods 37
- 3.1 Laser systems setup 37
  - 3.1.1 Laser source for the cooling transition at 425.6 nm 37
  - 3.1.2 Chromium spectroscopy cell 40
  - 3.1.3 Laser source for the repumping transition at 663.2 nm 42
  - 3.1.4 Passively stable transfer cavity 43
- 3.2 Vacuum apparatus 44
  - 3.2.1 Chromium oven chamber 44
  - 3.2.2 Zeeman slower 46

3.2.3 Atom guide chamber 47
3.3 Preparation of a magnetically guided ultra cold atom beam 48
3.4 Atom beam characterisation 49
3.4.1 Imaging system 49
3.4.2 Radial beam temperature 51
3.4.3 Beam velocity 53
3.4.4 Atom flux 56
3.4.5 Phase space density 57

4 Continuous loading of an optical dipole trap 59
4.1 Principle of the ODT loading mechanism 59
4.2 Magnetic field configuration and trap potentials 61
4.3 Simulation of the loading process 64
4.4 Conclusion 67

5 Laser cooling of a magnetically guided beam of ultra cold chromium atoms 69
5.1 Experimental implementation of the transverse cooling scheme 69
5.2 Experimental observation of transverse laser cooling 72
5.2.1 Laser cooling with magnetic offset field 72
5.2.2 Intensity dependence of the laser cooling process 75
5.3 Conclusion 75

6 Summary and outlook 77

Bibliography 79

1 Introduction

In this introductory chapter the role of ultra-cold atom beams in the field of atomic physics is approached from a historical perspective. Early atom beam experiments delivered seminal insights about atomic structures, and were followed by the commonplace application of atom beams in a variety of disciplines. The development of laser cooling allowed the preparation of ultra-cold atom beams and their employment for the generation of quantum degenerate gases, atom optics, atom lithography, and atom interferometry. In recent years, magnetically guided ultra-cold atom beams have generated considerable interest as intense sources of slow atoms, holding great promise for the realisation of a continuously pumped atom laser. This thesis presents experimental and theoretical studies on a magnetically guided beam of chromium atoms that are aimed at bridging the gap between the ultra-cold and the quantum degenerate regime. The organisation of this thesis is outlined at the conclusion of this chapter.

1.1 Effusive atom beams

The advancement of modern atomic, molecular and optical physics has been nurtured by a growing ability of experimentalists to prepare atoms in specific motional as well as electronic states, and to observe the evolution of these states under isolated conditions [1]. Atom beams, or atomic beams, as they are also referred too, have been a significant part of this development almost since its beginnings, by providing the means of generating samples of isolated atoms with specific distributions of atomic velocities, positions and electronic states, which can then be further manipulated and studied in an experimental setup. Over time, many different types of atom beams have been conceived [2]. Likewise, the capabilities of atom beam devices have evolved, in terms of available atomic species, as well as in terms of attainable degree of control over and range of various beam specifications such as, for example, atom flux, beam shapes and velocity distributions.

The earliest and arguably most basic type of atom beam is the effusive atom beam, which, nevertheless, continues to represent the backbone of many advanced contemporary atom beam experiments. An effusive atom beam is obtained by releasing a low pressurised atomic gas though a small entrance aperture into a high vacuum environment, where it forms an expanding stream of entering atoms. Through a second aperture, this stream can then be shaped into a collimated beam of atoms that propagates through the vacuum. Via the collimation, control is exercised over both the trajectory of the atoms as well as their transverse velocity spread, while the vacuum shields the atom beam from collisions with background gas constituents.

The first atom beam, which corresponded in essence to the above given description, was realised almost exactly one century ago by Dunoyer, who observed the ballistic propagation of Na atoms inside an evacuated glass tube [3]. His discovery occurred shortly after the first rotary mercury pump had become commercially available, which had been invented by

Gaede [4] in 1905. By employing this novel high vacuum pump, Dunoyer was able to generate sufficiently low pressures inside his glass tube such that Na atoms could travel along the tube without colliding with background gas molecules. In the following years, the atom beam technology was refined and consolidated most notably by Stern [5, 6], who together with Gerlach, famously discovered space quantisation [7] and directly measured the magnetic moments of atoms [8] by observing a discrete splitting of a silver atom beam that had passed through an inhomogeneous magnetic field. These two studies became the first in a series of ground breaking atom beam experiments that revealed information about fundamental structure of the atoms [9] and that were awarded with Nobel prizes in physics.

The invention of the nuclear magnetic resonance (NMR) method [10] by Rabi constituted another major advancement along these lines. Based on the interaction of the atom with microwave and radio frequency radiation, for which compared to optical radiation far superior coherent radiation source were available at the time, it allowed for the first time coherent control of the atomic states, and opened the possibility to investigate the structure of atomic nuclei by measuring nuclear magnetic moments with unprecedented precision [11]. High resolution NMR spectroscopy performed on an atomic hydrogen beam by Lamb lead in the following to the discovery of the Lamb-shift in the hydrogen atom[12]. In addition, precise atom beam magnetic resonance measurements of nuclear magnetics moments for different states of ^{69}Ga, ^{71}Ga, and ^{23}Na allowed Kusch [13] to determine the anomalous gyromagnetic ratio of the electron. By contradicting the Dirac theory of the electron, both results paved the way for the development of quantum electrodynamics.

A significant obstacle for atomic beam NMR measurements was imposed the by requirement of a uniform phase over the entire interaction area, which requires the area's dimensions to be smaller than the employed NMR wavelength. Due to a the lack of slow atom beam sources of sufficient intensity, which came into being only about three decades later with the help of the laser cooling methods discussed further below, this length limitation restricted the effective measurement time and thus the attainable spectroscopic resolution. It was vanquished by the separated oscillatory field method invented by Ramsey [14], which found, among many others, important applications in metrology, where it provided a basis for the realisation of highly accurate cæsium atomic beam frequency standards [15], which shortly after became reference standards of the International System of Units (SI) [16].

Attempts to further increase the accuracy of atomic beam NMR lead, inspired by the earlier invented molecular beam based ammoniac maser [17], to the development of the atomic hydrogen maser [18] by Ramsey. It was the first atomic maser and was based on an atomic hydrogen beam, which served as a source of hydrogen atoms in the upper hyperfine ground state level that were focused by a state selecting hexapole magnet into a tunable microwave cavity. A coating allowed the hydrogen atoms to bounce off the interior walls of the cavity without change of the hyperfine state. The cavity thus acted as a trap for the hydrogen atoms, which, compared to a bare atomic beam setup, resulted in an increased effective interaction time and higher atom densities, thereby narrowing and intensifying the emitted microwave band.

1.2 Laser cooled atom beams

The high intensity and spectral purity of laser sources propelled the establishment of high resolution optical spectroscopy during the 1970s, which is characterised by the elimination of first-order Doppler broadening of spectral lines due to Doppler free spectroscopic methods, such as saturation spectroscopy [19, 20], two-photon spectroscopy [21, 22, 23] and polarisation spectroscopy [24]. Much like in the case of NMR spectroscopy, the attainable optical resolution was then constrained by the line broadening due to the limited transit time of atoms during a spectroscopic measurement, as underscored by the efforts undertaken by Hall and Chebotayev to reduce transit time broadening through the construction of wide diameter radiation field spectrometers [25, 26, 27, 28].

Research on the laser manipulation of atomic motion in atomic beams by light forces initiated by the work of Ashkin [29] in 1970 offered a route to much anticipated slow atom beam sources. In the following years different experiments succeeded in demonstrating atom beam deflection by a travelling wave[30], as well as focusing [31] and deflection by a standing wave [32]. In addition, atom beam deflection by classical resonant radiation had been studied by [33] based on early observations by Frisch made in the 1930s [34].

The production of a slow atom beam source [35], and ultimately stopping of atoms in the laboratory frame [36], was achieved by the mid-1980s with the Zeeman slower. By combining resonant radiation with a magnetic field varying along the atom beam axis the decreasing Doppler shift of the atomic resonance frequency due to the deceleration could be compensated for. Similarly, frequency chirping of the decelerating laser beam was successfully employed around the same time for slowing and stopping [37] of atom beams.

Once atomic samples could be prepared with arbitrarily low averages velocities in the laboratory, the concept of Doppler cooling with counter-propagating resonant laser beam pairs, which had been demonstrated earlier with trapped ions [38, 39] , could be employed to reduce the spread of atomic velocities in all spatial dimensions, as demonstrated by the first realisation of an optical molasses [40].

Laser cooling of atoms achieved unprecedented low temperatures, thereby enabling the confinement of atomic samples in a variety of atom trap configurations. Important steps along this direction were the first demonstration of trapping of atoms in a magnetic trap[41], in an optical dipole trap [42] and in an magneto-optical trap[43]. Trapping of atoms could be employed to implement cooling methods that transcend laser cooling such as evaporative cooling [44].

Cooling and trapping techniques have profoundly impacted the generation of slow and cold atom beams and vice versa. While atom traps have been loaded from atom beams, traps have also served as reservoir of cold atoms for the generation of atom beams. Methods for the generation and manipulation of laser cooled atom beams include focusing, compression, deflection, reflection, cooling [45].

1.3 Quantum degenerate atom beams

The statistical mechanics of a gas consisting of indistinguishable quantum particles, such as atoms, differs at low temperatures from that of classical gas, as first pointed out in 1924 by Bose [46]. Together with Einstein he worked out the first statistical description of an ideal quantum gas [47, 48]. Now known as *Bose-Einstein statistic*, it applies to a fundamental class of quantum particles named *bosons*. A seminal scientific achievement based on the laser cooling and trapping techniques discussed earlier was the first experimental realisation of a peculiar prediction of the Bose-Einstein theory, the condensation of bosonic atoms in the motional ground state of a trap, which was accomplished just about 70 years later in 1995 [49, 50]. A Bose-Einstein-condensate (BEC) represents a quantum system described by a macroscopic wave function. In this respect it resembles photons stored inside a laser resonator. Unlike photons however, atoms in a BEC possess mass and interact both with each other and with external fields, which entails a large variety of quantum phenomena that can be explored by employing experiments on the basis of BECs.

An especially feature rich class of BECs are dipolar BECs, which are formed from atoms that possess a large magnetic dipole moment in the ground state, which results in a significant contribution of the anisotropic and long range dipole-dipole interaction in addition to the prevalent isotropic, short range *s-wave* interaction [51]. The first and most prominent example of a dipolar BECs is obtained from atoms of the element chromium, whose condensation first succeeded 2005 in Stuttgart [52, 53]. Tuning of the s-wave scattering length using Feshbach resonances [54] was employed to reveal and to isolate its distinct dipolar properties [55, 56, 57, 58].

By releasing atoms from a trapped BEC, a coherent quantum matter beam can be generated, which, in close analogy to a laser beam that is outcoupled from an optical cavity, is termed *atom laser* [59]. The first such novel type of atom beam was prepared in 1997 [60]. A number of alternative outcoupler schemes were developed shortly after by different research groups [61, 62, 63, 64]. All these outcoupler schemes have in common that the length of the atom laser wave train is ultimately constrained by the number of a condensed atoms that are stored inside the trap from which the atom laser is released. The generated atom lasers thus possess rather short wave trains, and thus resemble pulsed optical laser beam. Although much desired, a truly continuous atom laser, quantum matter analogue to a cw laser beam therefore still remains to be realised.

1.4 Magnetically guided ultra cold atom beams

A magnetic potential configuration that confines atoms in two dimensions and while permitting them to propagate along the third dimension can be employed as a magnetic guide for an atom beam. Initial experiments with atom beams passing through magnetic guide configuration, which investigated the focussing of an atom beam by a 2D static magnetic hexapole field, were performed in the 1950s [65, 66]. Due to the rather shallow depth of magnetic potentials for atoms, true guiding of atoms requires sufficiently low transverse kinetic energies, corresponding to temperatures below 10 K (see section 2.2.2), which could be realised decades later by employing laser cooling methods (see also [67, 68]).

Magnetic guides loaded with ultra cold atoms from a magneto-optical trap (MOT) have in recent years been successfully established as intense sources of ultra cold atom beams [69, 70], with maximum loading rates of up to $7 \cdot 10^9$ atoms s^{-1} at temperatures below 400 μK have been demonstrated [71]. For chromium, our group has recently reported the continuous loading of over 10^9 atoms s^{-1}, albeit at somewhat higher temperatures than in [71], by operating a moving molasses MOT in the field of a magnetic guide [72].

Considerable effort has been invested in concepts for the exploitation of magnetic guides as ultra cold atom sources for the production of Bose-Einstein-Condensates (BECs) [73], which is typically performed by a time sequence of cooling steps leading to an average yield of 10^4 to 10^6 atoms/sec for the best alkali experiments and 10^3 atoms/sec for chromium BEC [52]. Magnetic guides allow to spatially separate and to perform simultaneously otherwise interfering cooling steps. They offer thus the prospect to prepare BECs in continuous manner with considerably increased production rates.

A main driving force behind these efforts to overcome the limits of current BEC production methods in terms of both, the maximum numbers of atoms in the condensate and the maximum production rate, is the prospective realisation of a truly continuous atom laser. Two conceptually different pathways towards a coherent and continuous source of quantum matter have been proposed. The first pathway is based on the direct condensation of a guided atom beam via evaporative cooling inside a magnetic guide [71, 73]. The second pathway employs a constantly refilled reservoir of ultra cold atoms from which atoms are transferred into a continuously maintained condensate [74, 75].

1.5 Laser cooling of a magnetically guided ultra cold atom beam

In this thesis, we address two questions regarding the laser cooling of atoms inside a magnetically guided atom beam that are of relevance for both pathways.

First, we study from a theoretical viewpoint, how chromium atoms from a guided atom beam can be transferred most efficiently into a superimposed optical dipole trap, which would open the possibility to reach quantum degeneracy via evaporative cooling. In order to solve the underlying problem of dissipating the kinetic energy associated with the longitudinal motion of the guided atoms, we propose a deceleration scheme that uses a magnetic potential barrier in combination with a fast optical pumping process. Through numerical simulations of atomic trajectories we determine the fraction of the atom beam population that can be trapped inside the ODT depending on the beam velocity, radial and the longitudinal beam temperature. If implemented, the proposed loading scheme would constitute a direct precursor for the production of large Cr BECs with considerably increased production rates. As it is fully continuous in nature, it could, in principle, be used to operate the ODT as pump reservoir for a pumped continuous atom laser.

Second, we investigate experimentally, how the transverse temperature of an ultra cold atom beam inside a magnetic guide can be reduced by laser cooling in such a way that the overall phase density of the beam is increased. In our above mentioned theoretical studies we have identified the radial beam temperature as the most critical parameter to make the transfer of atoms from the guided atom beam to the ODT more efficient. However, the loading of the guide via imposes a lower limit on the initial atom beam temperatures. We have implemented a continuous laser cooling scheme that allows to reduce the radial beam temperature below this limit, by combining transverse compression of the atom beam together with Doppler cooling in a magnetic offset field. We describe the experimental conditions under which we achieve cooling below the Doppler limit, while the initial high atom flux is preserved.

1.6 Thesis outline

This thesis consists of six chapters, which are organised as follows:

Chapter 2 lays out the essential physical concepts that are underlying the theoretical and experimental investigations presented in this thesis. The main topics covered are the laser cooling, the guiding and the trapping of neutral atoms. A key aspect of the treatment is the application of the presented methods to atoms of the chromium isotope ^{52}Cr.

Chapter 3 covers the experimental apparatus that we employ for our studies. It describes the vacuum chambers and the laser systems that are required for the generation of a magnetically guided beam of ultra-cold chromium atoms. It also details the imaging system and the analysis methods that permit the physical characterisation of the atom beam.

Chapter 4 presents our theoretical investigations regarding the loading of atoms from the magnetic guide into an optical dipole trap. Using numerical simulations of the loading process we have studied the transfer efficiency depending on the initial velocity and temperature of the atom beam.

Chapter 5 reports on our experimental investigations on the transverse laser cooling of atoms that are launched into the atom guide from a moving molasses magneto-optical trap. By using a two-dimensional optical molasses configuration, Doppler cooling can be performed on atoms that are passing through a tapering of the atom guide. Final transverse temperatures of the atom beam below the Doppler temperature can be achieved, which result in significant increases of its phase space density.

Chapter 6 summarises the results of our investigations.

2 Physical preliminaries

The precise control of both internal and external atomic degrees of freedom constitutes the basis for our studies on ultra-cold ^{52}Cr atoms that are presented in this thesis. The physical foundations of the experimental methods that we employ in this context are the subject of this chapter. Emphasis is laid on those aspects of the theory that are particular relevant and readily applicable to the presentation and the discussion of our studies in the remaining chapters of this thesis. A large part of the material in this chapter is also covered by a number of excellent textbooks, to which we refer the reader for a more comprehensive and more general treatment of the matter. [76, 77, 78, 79].

2.1 Spectroscopic properties of ^{52}Cr

The interactions of atoms with external electromagnetic fields that we use for the manipulation of our samples, as outlined in section 2.2, are determined by their respective spectroscopic properties. In the framework of this thesis we are exclusively concerned with atoms of the chromium isotope ^{52}Cr, to which we refer in the following occasionally also by the term *chromium atom*, assuming that it is understood that some of our statements might in the strict sense only be valid for the ^{52}Cr isotope.

2.1.1 Nuclear properties

The element chromium has four stable isotopes, which are listed in table 2.1.1 together with their respective nuclear spins and natural abundances. Out of these, the ^{53}Cr isotope, possessing a half-integer nuclear spin of $I = 3/2$, is the only one which obeys a fermionic quantum statistic. The other three isotopes, namely ^{50}Cr, ^{52}Cr and ^{54}Cr, are of bosonic kind with zero nuclear spin. Possessing a magic neutron number $N = 28$, the isotope ^{52}Cr is the most abundant one, with a natural abundance of 83.79 %,

The differences in size and mass of the nuclei between the isotopes lead to distinct line shifts in their atomic spectra [81, 82]. The experimental procedures that we employ for our studies are by design susceptible to these isotope shifts and can be used to prepare and to investigate isotopically pure samples.

Isotope	Nuclear spin	Nat. abundance
^{50}Cr	0	4.35 %
^{52}Cr	0	83.79 %
^{53}Cr	3/2	9.50 %
^{54}Cr	0	2.37 %

Table 2.1: Stable isotopes of the element chromium: nuclear spins and natural abundances [80].

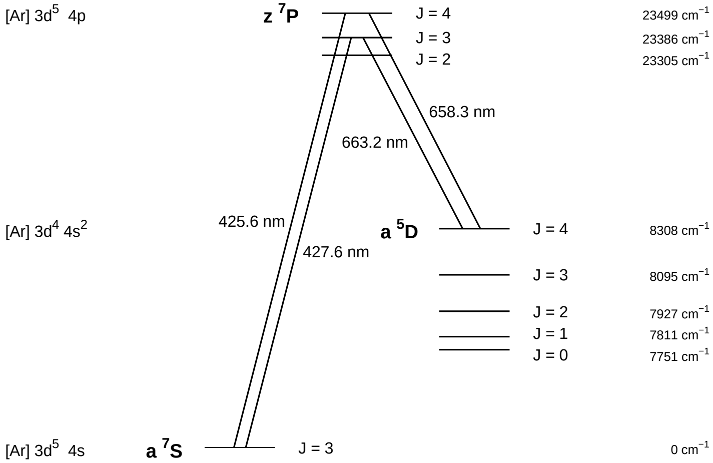

Figure 2.1: Selected electronic levels of ^{52}Cr. The interconnecting lines represent optical transitions that are relevant to our studies.

2.1.2 Electronic configuration of the ground state

Chromium is the element with the atom number 24. Its electronic ground state is composed of a filled argon shell and six valence electrons, which together constitute a [Ar] $3d^5$ $4s^1$ configuration. The incomplete *d* sub-shell identifies chromium as a transition metal. The coupling of the valence shell electron spins and orbital angular momenta is well described by the *LS*-coupling scheme [76], which yields the $^7S_3$ level as ground state level. Due to the absence of nuclear spin, the energy levels of ^{52}Cr exhibit no hyperfine splitting.

2.1.3 Important optical transitions

Figure 2.1 displays a schematic representation of selected energy levels. The lines connecting different levels represent optical transitions that are relevant for our studies. Basic properties of these transitions are listed in table 2.1.3, including the saturation intensity I_S, which is derived using

$$I_S = \frac{\pi h c \Gamma}{3\lambda} . \tag{2.1}$$

Here, h denotes Planck's constant, Γ the natural linewidth and λ the vacuum wavelength of the respective transition.

The $^7S_3 \longrightarrow {}^7P_4$ transition is the principal transition used for laser cooling [83, 84, 85, 86]. It has a sufficiently large natural line width Γ of 31.5 MHz to allow appreciable scattering rates. In addition, it is a practically closed transition, as its upper $^7P_4$ level decays with a branching ratio of about $2 \cdot 10^5$:1 back to the ground state.

Transition	λ/nm	$\Gamma/(2\pi\cdot\mathrm{s})^{-1}$	$I_\mathrm{S}/(\mathrm{mW\,cm^{-2}})$	Description
${}^7\mathrm{S}_3 \longrightarrow {}^7\mathrm{P}_4$	425.555	$31.5\cdot10^6$	8.50	Cooling transition
${}^7\mathrm{S}_3 \longrightarrow {}^7\mathrm{P}_3$	427.600	$30.7\cdot10^6$	8.17	Optical pumping
${}^5\mathrm{D}_4 \longrightarrow {}^7\mathrm{P}_4$	658.274	127	$9.26\cdot10^{-6}$	Decay to meta stable state
${}^5\mathrm{D}_4 \longrightarrow {}^7\mathrm{P}_3$	663.185	$6\cdot10^3$	$0.4\cdot10^{-3}$	Repumping transition

Table 2.2: Optical transitions in ^{52}Cr that are of relevance for the work presented in this thesis. Quoted are vacuum wavelength λ, natural line width Γ and saturation intensity I_S.

In a situation, where a large number of photons is scattered, such as in a magneto-optical trap (see section 2.2.8), optical leaking from the cooling transition can, nevertheless, become relevant. Optical leaking occurs in this case predominantly via the ${}^7\mathrm{P}_4 \longrightarrow {}^5\mathrm{P}_4$ transition. As the state associated with the ${}^5\mathrm{D}_4$ term is a long lived metastable state, optical leaking from the cooling transition allows the accumulation of sizable numbers of metastable state atoms.

Effective transfer from the metastable to the ground state is possible via optical pumping to the ${}^7\mathrm{P}_3$ level, from which a decay into the ground state occurs with a high probability. This decay is marked by the emission of a single photon at a wavelength of 427 nm, which plays a crucial role for the measurement of the absolute flux of atoms discussed in section 3.4.4.

2.1.4 Zeeman splitting in an external magnetic field

In the presence of a static magnetic field $\mathbf{B}$, the spectral lines of an atom exhibit characteristic splittings, which are described by the Zeeman effect. They are caused by the interaction of the field with the intrinsic magnetic moment of the atom. In the case of ^{52}Cr, only electronic spins and orbital angular momenta contribute to the magnetic moment. Its corresponding operator $\hat{\boldsymbol{\mu}}$ can be expressed in terms of the total spin operator $\hat{\mathbf{S}}$ and the total orbital angular momentum operator $\hat{\mathbf{L}}$ by

$$\hat{\boldsymbol{\mu}} = -\mu_\mathrm{B}\,\hat{\mathbf{L}} - g_\mathrm{s}\,\mu_\mathrm{B}\,\hat{\mathbf{S}}, \tag{2.2}$$

where μ_B denotes the Bohr magneton and g_s the gyromagnetic ratio of the electron. The Hamiltonian $\hat{\mathbf{H}}_\mathrm{zm}$ of the interaction with the field depends on the projection of $\hat{\boldsymbol{\mu}}$ on $\mathbf{B}$ and is given by $\hat{\mathbf{H}}_\mathrm{zm} = -\hat{\boldsymbol{\mu}}\cdot\mathbf{B}$. Using equation (2.2) a simple expression for its time averaged expectation value E_zm can be obtained by including the Land factor g_J and by choosing the axis for the quantisation of the total angular momentum such that it is aligned with $\mathbf{B}$ [76]:

$$E_\mathrm{zm} = \left\langle -\hat{\boldsymbol{\mu}}\cdot\mathbf{B} \right\rangle = g_\mathrm{J}\, m_\mathrm{J}\, \mu_\mathrm{B}\, |\mathbf{B}|\,. \tag{2.3}$$

States with different magnetic quantum numbers m_J that belong to the same spectroscopic term are commonly termed Zeeman substates. Without magnetic field these states are degenerate. The Zeeman interaction described by equation (2.3) lifts the degeneracy by dividing each level into $2\,J+1$ evenly spaced Zeeman sublevels, which are centred around the original zero field level.

Due to the Zeeman interaction, a single transition between two degenerate levels converts under the influence of a static magnetic field into a manifold of transitions between two sets of Zeeman sublevels. As a consequence, a spectroscopic line with frequency ω_0 splits up into Zeeman components with respective frequencies $\omega_0 + \omega_{\text{zm}}$. For a transition between two given Zeeman sublevels, the Zeeman line shift ω_{zm} depends on the difference between the Zeeman energy of the upper level $\left(E^*_{\text{zm}}\right)$ and of the lower level (E_{zm}). With equation (2.3) holds:

$$\hbar\,\omega_{\text{zm}} = E^*_{\text{zm}} - E_{\text{zm}} = \left(g^*_{\text{J}}\,(m_{\text{J}} + \Delta m_{\text{J}}) - g_{\text{J}}\,m_{\text{J}}\right)\mu_{\text{B}}\,|\mathbf{B}| = \Delta\mu\,|\mathbf{B}|\,. \tag{2.4}$$

Here we have introduced the quantity $\Delta\mu$ in order to denote the change in the magnetic moment's projection on $\mathbf{B}$ due to the transition. The change in the magnetic quantum number is denoted by Δm_{J}. For σ^+ and σ^--transitions Δm_{J} is equal to $+1$ and -1, respectively, while for π-transitions m_{J} is equal to 0. Depending on magnetic quantum number m_{J} of the initial state and on the value of Landé-factors g^*_{J} and g_{J} the Zeeman line shift described by equation (2.4) can take both positive and negative values.

2.2 Laser cooling and trapping of ^{52}Cr

The interactions of an chromium atom with external fields produce different types of mechanical forces that can be used to tightly control its state of motion and its position in space. For the preparation of ultra-cold samples of atoms a variety of methods have been devised that combine these forces in sophisticated and often ingenious ways. Thereby, reductions of sample temperatures from above 1000 K (thermal effusion) to well below 1 mK (ultra cold gases) can be achieved. Even lower temperatures and, ultimately, quantum degeneracy are reached by employing atom-atom interactions in addition to the interaction with external fields [52, 87].

2.2.1 The definition of temperature in laser cooling

The conventional thermodynamic definition of temperature applies to a system in a state of thermal equilibrium. In the field of laser cooling the conventional temperature definition is extended such that a temperature can in specific cases also be attributed to atomic samples that are far from thermal equilibrium [77]. Typical examples for such non-equilibrium samples comprise atoms that exchange energy with a radiation field, as well as atoms that are in a dilute state, where the thermalisation time due to a low collision rate exceeds the experimentally relevant time scales. Such atomic samples can, nevertheless, exist in a steady-state and exhibit momentum and energy distributions that resemble those of proper thermal distributions [1].

In this thesis, we follow the usual convention to attribute to such samples a temperature T that is derived from the mean energy per kinetic degree of freedom in accordance with the equipartition theorem via

---

[1] It can be shown, in fact, that certain laser cooling methods, such as Doppler cooling (see also section 2.2.7), inherently produce these type of quasi-thermal distributions[77].

$$\frac{k_\mathrm{B} T}{2} = \frac{m \langle v_\mathrm{k}^2 \rangle}{2}, \tag{2.5}$$

where k_B represents Boltzmann's constant, m the mass of the atom and v_k the component of the atomic velocity along the considered degree of freedom.

2.2.2 Magnetic forces for guiding and trapping

In an inhomogeneous static magnetic field $\mathbf{B(r)}$, the Zeeman effect described in section 2.1.4 accounts for a conservative magnetic force $\mathbf{F}_\mathrm{m}(\mathbf{r})$ that is associated with a magnetic potential $U_\mathrm{m}(\mathbf{r})$ derived directly from equation (2.3):

$$\mathbf{F}_\mathrm{m} = -\nabla U_\mathrm{m} = -g_\mathrm{J}\, m_\mathrm{J}\, \mu_\mathrm{B}\, \nabla\, |\, \mathbf{B(r)}\, |\,. \tag{2.6}$$

From equation (2.6) follows that atoms in a Zeeman-substate with magnetic quantum number $m_\mathrm{J} > 0$ are attracted toward lower values of the field magnitude $|\,\mathbf{B(r)}\,|$. They are thus commonly termed *low-field seekers*, whereas atoms with $m_\mathrm{J} < 0$ are termed *high-field seekers*.

In order to create a potential suitable for the trapping or the guiding of atoms we require a field that yields either a local minimum or a local maximum of the field magnitude. From Maxwell's equations it can be shown, however, that the magnitude of the magnetic field cannot possess a local maximum. A purely magnetic trap can therefore only be realised for low-field seekers [88], whereas trapping of high field seekers requires in general some kind of additional non-magnetic confinement.

Another important requirement is that the magnetic field strength is sufficiently large such that the trap depth exceeds the thermal energy of the atoms that are to be trapped. Assuming a maximum practical field strength of about 10 T, this limits the application of magnetic traps in the case of chromium atoms to samples with temperatures below about 10 K [2]. Magnetic trapping and guiding of atoms thus typically requires preceding cooling steps such as, for example, Zeeman slowing (section 2.2.6), Doppler cooling (section 2.2.7), and magneto-optical trapping (section 2.2.8).

2.2.3 Magnetic quadrupole guide for atoms

Magnetic quadrupole fields are widely used as static field geometries that yield confining potentials for low-field seeking atoms. They are also commonly used in conjunction with optical fields in order to form different types of magneto-optical traps. The magnetic guide for ultra cold atoms used in our studies is based on a two-dimensional quadrupole field that confines atoms radially, while allowing them to propagate freely along the axis of the guide.

Figure 2.2 a) illustrates the operating principle of such a magnetic quadrupole guide. Four parallel bars, with centres arranged in a square and spaced a distance d apart, carry the static

---

[2] Linear trap potential in three dimensions. Mean internal energy per atom $E_\mathrm{int} = 9/2\, k_\mathrm{B}\mathrm{T}$.

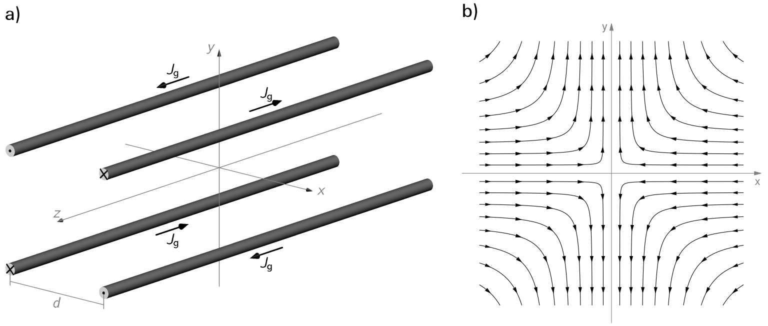

Figure 2.2: a) Magnetic atom guide consisting of four parallel bars with quadratically arranged centres. A current J_g flows through the bars in alternating opposing directions, thereby generating a transverse two-dimensional magnetic quadrupole field near the z-axis. b) Corresponding magnetic field lines.

electrical current J_g in alternating opposing directions. Adopting the Cartesian coordinate system defined in figure 2.2 a), the radial distance r from the central guide axis is given by $r = (x^2 + y^2)^{1/2}$. For $r \ll d$ and for infinitely long bars the generated guide field $\mathbf{B}_g$ is in excellent approximation described by a magnetic quadrupole field [78], with

$$\mathbf{B}_g = \left(-b_g\, x, b_g\, y, 0\right). \tag{2.7}$$

The corresponding field lines are shown in figure 2.2 b). The variable b_g represents the absolute value of the magnetic field gradient. Its value can be derived from the Biot-Savart law and yields, with the vacuum permeability denoted by μ_0,

$$b_g = \frac{4\, J_g\, \mu_0}{d^2 \pi}. \tag{2.8}$$

Using equation (2.6) and (2.7) we obtain for the guiding potential U_g as a function of r

$$U_g(r) = m_J\, g_J\, \mu_B\, b_g\, r. \tag{2.9}$$

2.2.4 The radiation scattering force

Electromagnetic radiation carries momentum. Scattering of resonant light by an atom transfers momentum between the light field and the atom. By doing so it exerts a mechanical force on the atom, which is the basis for a number experimental methods introduced in this chapter, such as the Zeeman slower, the optical molasses and the magneto-optical trap.

In the following, we consider the case of a two-level atom with line width Γ and resonance frequency ω_0 that is subject to a monochromatic plane wave with frequency ω_L, wave vector $\mathbf{k}_L$ and intensity I_L. The transfer of momentum is mediated via the repeated absorption of a single photon with momentum $\hbar\,\mathbf{k}_L$ followed by the spontaneous emission of a new photon into a random direction. The scattering thus changes the atomic momentum in a stochastic manner. Since the radiation pattern of spontaneous emission exhibits point symmetry with respect to the position of the atom, the average change in momentum from spontaneous emission is equal zero. The total average momentum transferred per scattered photon is therefore equal to the momentum $\hbar\mathbf{k}_L$ of each absorbed photon. The associated average change in velocity per photon is equal to the recoil velocity v_{rec}, which for the main $^7S_3 \longrightarrow {}^7P_4$ cooling transition of ^{52}Cr evaluates to $\text{v}_{\text{rec}} = 1.8\,\text{cm}\,\text{s}^{-1}$.

The recoil velocity is small compared to the mean atomic velocities that we encounter in our experiments. A large number of scattered photons is therefore necessary to induce a noticeable change in the atomic velocity. This means that a valid deterministic expression for the scattering force $\mathbf{F}_{\text{sc}}$ can be derived by regarding only its average over many cycles of absorption and emission, which is proportional to average photon scattering rate R_{sc}. For a two level atom with saturation intensity I_S the scattering rate is given by

$$R_{\text{sc}} = \frac{\Gamma}{2}\,\frac{I_L/I_S}{1 + I_L/I_S + 4\delta_{\text{eff}}^2/\Gamma^2}\,. \tag{2.10}$$

Here, δ_{eff} denotes the effective detuning of the laser light, which is the detuning of the laser light frequency from the atomic resonance in the rest frame of the atom. For an atom moving with a velocity $\mathbf{v}$ in the laboratory frame the Doppler shift [89] contributes to δ_{eff}, resulting in

$$\delta_{\text{eff}} = \omega_L - \omega_0 - \mathbf{k}_L \cdot \mathbf{v}. \tag{2.11}$$

We can state $\mathbf{F}_{\text{sc}}$ as a function of $\mathbf{k}_L$ and δ_{eff} using equation (2.10), which yields

$$\mathbf{F}_{\text{sc}}\left(\mathbf{k}_L, \delta_{\text{eff}}\right) = \hbar\mathbf{k}_L \cdot \frac{\Gamma}{2}\,\frac{I_L/I_S}{1 + I_L/I_S + 4\delta_{\text{eff}}^2/\Gamma^2}\,. \tag{2.12}$$

The scattering force is maximal on resonance, when $\delta_{\text{eff}} = 0$. It saturates when the light intensity becomes large compared to the saturation intensity I_s.

The scattering force is capable of delivering enormous accelerations to an atom. Equation (2.12) yields, for instance, in the case of the ^{52}Cr $^7S_3 \longrightarrow {}^7P_4$ cooling transition a maximum possible acceleration of about $3 \cdot 10^5\,\text{m}\,\text{s}^{-2}$. However, this strong acceleration can for a given laser frequency due to the Doppler shift only be applied to atoms within a limited velocity range. The width Δv of the effective velocity range can be estimated from $\Delta v \approx \Gamma/k_L$, which for the main cooling transition of ^{52}Cr evaluates to $\Delta v \approx 2\,\text{m}\,\text{s}^{-1}$.

2.2.5 Optical pumping and stretched states

The Zeeman substates with $m_J = |J|$ are also known as *stretched states*. In a stretched state, the magnetic moment of the atom is maximally aligned with the external magnetic field, being orientated either along ($m_J = -J$) or opposite to it ($m_J = J$). An atomic ensemble in which all atoms are in the same stretched state is therefore magnetically polarised. In

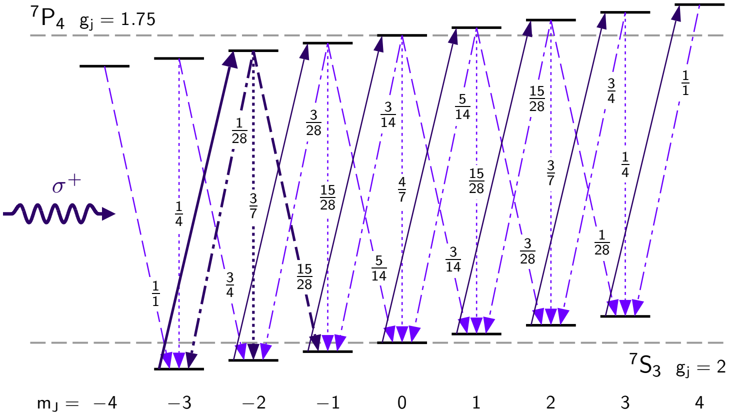
$^7P_4$ $g_j = 1.75$
σ^+
$\frac{1}{1}$
$\frac{1}{4}$
$\frac{3}{4}$
$\frac{1}{28}$
$\frac{3}{7}$
$\frac{15}{28}$
$\frac{3}{28}$
$\frac{15}{28}$
$\frac{5}{14}$
$\frac{3}{14}$
$\frac{4}{7}$
$\frac{3}{14}$
$\frac{5}{14}$
$\frac{15}{28}$
$\frac{3}{28}$
$\frac{15}{28}$
$\frac{3}{7}$
$\frac{1}{28}$
$\frac{3}{4}$
$\frac{1}{4}$
$\frac{1}{1}$
$^7S_3$ $g_j = 2$
$m_J =$ -4 -3 -2 -1 0 1 2 3 4

Figure 2.3: Magnetic polarisation of the ^{52}Cr ground state via optical pumping on the $^7S_3 \longrightarrow {}^7P_4$ transition with σ^+-polarised light. A weak magnetic field has lifted the degeneracy of the respective Zeeman substates. Dashed horizontal lines indicate the positions of the degenerate levels in the absence of the field. The pumping light exclusively excites transitions with $\Delta m_J = +1$, which are represented by the upward arrows. The respective relative strength of the decay channels are indicated by the labels of the corresponding downward arrows. In the course of many iterated excitation cycles the atom is eventually pumped to the stretched $^7S_3$ $m_J = +3$ substate. Together with the $^7P_4$ $m_J = +4$ substate this state forms a closed optical cycle with respect to the pumping light.

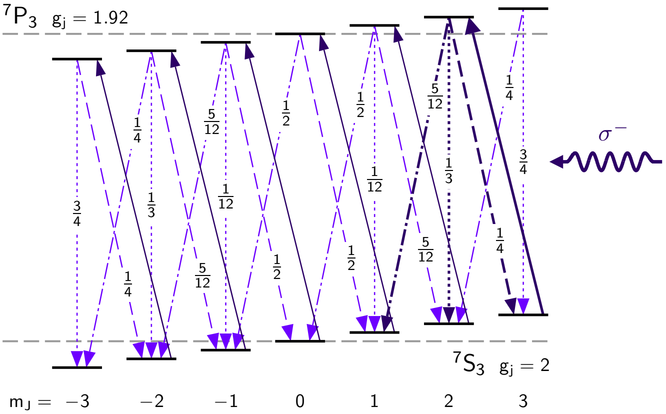
$^7P_3$ $g_j = 1.92$
σ^-
$\frac{3}{4}$
$\frac{1}{4}$
$\frac{1}{4}$
$\frac{1}{3}$
$\frac{5}{12}$
$\frac{5}{12}$
$\frac{1}{12}$
$\frac{1}{2}$
$\frac{1}{2}$
$\frac{1}{2}$
$\frac{1}{2}$
$\frac{1}{12}$
$\frac{5}{12}$
$\frac{5}{12}$
$\frac{1}{3}$
$\frac{1}{4}$
$\frac{3}{4}$
$\frac{1}{4}$
$^7S_3$ $g_j = 2$
$m_J =$ -3 -2 -1 0 1 2 3

Figure 2.4: Optical pumping with σ^--polarised light on the $^7S_3 \longrightarrow {}^7P_3$ transition. The pumping light drives the atom into the stretched $m_J = -3$ substate, which is dark state.

contrast, an ensemble in thermal equilibrium at high temperatures possesses almost evenly occupied Zeeman sublevels and is therefore unpolarised.

Optical pumping with circular polarised light can be used to prepare an ensemble of atoms in a stretched state. Figure 2.3 illustrates the polarisation of the ^{52}Cr ground state via optical pumping on the $^7\mathrm{S}_3 \longrightarrow {}^7\mathrm{P}_4$ transition with σ^+-polarised light. A weak magnetic field lifts the degeneracy of the upper and the lower Zeeman sublevels. The transitions to the upper sublevels that are excited by the pumping light must fulfil $\Delta m_\mathrm{J} = +1$. Subsequent decays back to the ground state sublevels proceed, by contrast, stochastically with $\Delta m_\mathrm{J} \in \{+1, 0, -1\}$ according to probabilities that are proportional to the absolute squares of the corresponding Clebsch-Gordan coefficients. Thus, repeated excitations by the pumping light will eventually drive the atom to the stretched $^7\mathrm{S}_3$ $m_\mathrm{J} = +3$ substate.

The optical pumping process presented in 2.3 has two properties that are of specific interest in the framework of this thesis. First, it transfers the atom to a magnetically trappable state (see also section 2.2.2). Second, together with the $^7\mathrm{P}_4$ $m_\mathrm{J} = +4$ sublevel the $m_\mathrm{J} = +3$ ground state sublevel forms a closed optical cycle that is strongly coupled to the σ^+-polarised pumping light. This permits the scattering of photons without altering the orientation of the magnetic moment with respect to the magnetic field. Thus it is of considerable significance for Zeeman slowing (see section 2.2.6) , as well as for the Doppler cooling inside the magnetic atom guide, which is presented in chapter 5.

Figure 2.4 illustrates optical pumping into a stretched state that is, in contrast to the earlier discussed $m_\mathrm{J} = +3$ substate in figure 2.3, decoupled from the pumping light. Here, the pumping light is resonant on $^7\mathrm{S}_3 \longrightarrow {}^7\mathrm{P}_3$ transition and σ^--polarised. It drives the atom much in the same way into stretched $^7\mathrm{S}_3$ $m_\mathrm{J} = -3$ as explained in the previous example. The $m_\mathrm{J} = -3$ substate can, however, not be excited by the pumping light, as the upper level has no $m_\mathrm{J} = -4$ sublevel. Since it does therefore not interact with the pumping light, this type of state is also denoted as *dark state* with respect to the pumping light. An application of the optical pumping into a dark state is the loading of an optical dipole trap (ODT) that is discussed at length in chapter 4. Once atoms inside the ODT have reached a dark state they can no longer be heated by the pumping light, which permits a reduction of the temperature inside the ODT via evaporative cooling.

2.2.6 Zeeman slowing of an atom beam

By directing resonant laser light opposite to the atomic motion, the scattering force can be employed for the deceleration of atoms. In order to decelerate atoms effectively it is, however, necessary to compensate the Doppler shift in equation (2.11). Zeeman slowing is a deceleration method that uses the Zeeman shift in a spatially varying magnetic field to fulfil the resonance condition of the scattering force along the trajectory of the atom. An important implementation of it is the Zeeman slower [35], which is a device commonly employed in the framework of ultra cold atom experiments for the deceleration of hot atoms beams emitted from thermal atom sources. Zeeman slowers are capable of slowing atom beams from initial velocities v_0 above hundreds of meters per second to final velocities v_f of only few meters per second. Thus, they allow to bridge the gap between the velocity regime of thermal atom beam sources and the capture velocities of magneto-optical traps (see section 2.2.8).

The geometry of the magnetic field $\mathbf{B}_\mathrm{ZS}$ of a Zeeman slower is critical for its performance. For the description of the spatial dependence of $\mathbf{B}_\mathrm{ZS}$, we assume that atoms from an atom beam propagate through the slower along the positive z-axis[3]. Laser light with wave vector $\mathbf{k}_\mathrm{L}$ opposes the atom beam, such that for atoms with velocity $\mathbf{v}$ holds $\mathbf{k}_\mathrm{L}{\cdot}\mathbf{v} = -k_\mathrm{L} v$. The frequency of the slower light is described by a detuning δ_L from the laboratory frame atomic resonance frequency ω_0 in the absence of additional external fields. The strength of the decelerating force exerted by the laser light is determined by the effective detuning δ_eff in equation (2.12). In the presence of a magnetic field δ_eff has to reflect the Zeeman line shift ω_M expressed in equation (2.4). Equation (2.11) thus has to be extended, yielding

$$\delta_\mathrm{eff} = \delta_\mathrm{L} + k_\mathrm{L} v + \frac{\Delta\mu\,|\mathbf{B}_\mathrm{ZS}|}{\hbar}\,. \tag{2.13}$$

From equation (2.13) it can be seen that the effective detuning and thus the decelerating force depends on the Zeeman substate of the atom. The slower field is usually oriented parallel to the beam, either along or opposite to it, such that circularly polarised light can be used to selectively drive cycling transitions between two stretched states, thereby preventing optical pumping to other Zeeman substates.

Atoms with velocity v experience the maximum deceleration a_ZS, when the resonance condition $\delta_\mathrm{eff} = 0$ is met. Starting at $z = 0$ the magnetic field $\mathbf{B}(z)$ of the slower along the z-axis shall compensate the Doppler shift such that atoms with an initial velocity v_0 are always decelerated with the maximum scattering force. In this case the velocity $v(z)$ inside the slower is for $0 \le z \le z_\mathrm{f}$ given by

$$v(z) = \left(v_0^2 - 2a_\mathrm{ZS}\,z\right)^{1/2}, \tag{2.14}$$

where z_f denotes the distance after which the atom is expected to come to a halt. Equation (2.14) yields for the halt position z_f :

$$z_\mathrm{f} = v_0^2\,(2a_\mathrm{ZS})^{-1}\,. \tag{2.15}$$

In order to meet the resonance condition, it follows from equation (2.13), (2.14) and (2.15) that the slower field must obey

$$|\mathbf{B}(z)| - |\mathbf{B}(z_\mathrm{f})| = \frac{\hbar\delta_\mathrm{L}}{\Delta\mu} + \frac{\hbar k_\mathrm{L} v_0}{\Delta\mu}\left(1 - \frac{z}{z_\mathrm{f}}\right)^{1/2} \tag{2.16}$$

---

[3] It is assumed that the ballistic propagation of an atom beam inside the Zeeman slower can be approximated by a linear trajectory. This would be the case for a sufficiently short slower or one that is oriented parallel to gravity.

The requirements on the Zeeman slower field are stated in equation (2.16) in terms of a single initial atomic velocity v_0. A typical application of a Zeeman slower might, however, comprise the slowing of an atom beam with a broad range of initial atomic velocities, such as one emitted by a thermal atom source.

Let us, therefore, consider the implications of equation (2.16) on the Zeeman slowing of an atom beam with an initially broad atomic velocity distribution. Atoms with initial velocity $v_\mathrm{i} > v_0$ are going to pass virtually unaffected through the slower, as there is no position inside the Zeeman slower where the resonance condition can be fulfilled. In contrast, low velocity atoms with initial velocities $v_\mathrm{i} < v_0$ will, while passing through the slower, eventually reach a position where the resonance condition is met. From then on, they will be decelerated in same way as atoms with initial velocity v_0. From an atom beam with a broad velocity distribution the slower thus collects all atoms with velocities below v_0 and bunches them into the same velocity class. Zeeman slowing does for atoms with $v_\mathrm{i} < v_0$ not only result in substantial reductions of laboratory frame velocities, but also in a squeezing of the velocity distribution, which is commonly referred to as one-dimensional cooling of the beam.

The velocity v_0 in equation (2.16) thus represents the upper threshold velocity of the slower. In order to maximise the slower output it often desirable to aim for a high value v_0, if permitted by technical constraints on the magnetic field strength, the length of the slower or the light intensity. Equation (2.16) describes the three most common magnetic field configurations used in Zeeman slowers, which are as follows:

1. *Decreasing field (σ^+) Zeeman slower* [35]
   The Zeeman slower light is tuned on resonance ($\delta_\mathrm{L} = 0$) and drives σ^+ transitions, thus $\Delta\mu > 0$. The Zeeman slower field decreases from the initial value $|\mathbf{B}(0)| = \hbar k_\mathrm{L} v_0 / \Delta\mu$ to the final value $|\mathbf{B}(z_\mathrm{f})| = 0$.

2. *Increasing field (σ^-) Zeeman slower* [90]
   The Zeeman slower light is red detuned, such that it fully compensates the initial Doppler shift seen by the undecelerated atoms ($\delta_\mathrm{L} = -k_\mathrm{L} v_0$). It drives σ^- transitions, thus $\Delta\mu < 0$. The Zeeman slower field increases from the initial value $|\mathbf{B}(0)| = 0$ to the final value $|\mathbf{B}(z_\mathrm{f})| = \hbar k_\mathrm{L} v_0 / \left|\Delta\mu\right|$.

3. *Spin-flip (σ^+/σ^-) Zeeman slower* [91, 92]
   This configuration is derived from the decreasing field slower. It uses, however, red detuned slower light ($-k_\mathrm{L} v_0 < \delta_\mathrm{L} < 0$). The spin-flip slower magnetic field equals that of the decreasing field slower with an additional opposing constant magnetic offset field of magnitude $|\delta_\mathrm{L}|\,\Delta\hbar/\mu$. The resulting slower field has an initial magnitude of $|\mathbf{B}(0)| = (\delta_\mathrm{L} + k_\mathrm{L} v_0)\,\hbar/\Delta\mu$. Its magnitude decreases until the field crosses zero, thereby reversing its direction. The polarisation of the slower light thus changes during the zero crossing from σ^+ to σ^-. While passing through the zero crossing atoms are optically pumped from the stretched state with $\Delta\mu > 0$ to the opposing one with $\Delta\mu < 0$, such that equation (2.16) remains valid.

The decreasing field Zeeman slower was the first slower to be realised. It has the disadvantage that the slower light is resonant with the atoms at the exit of the slower, which potentially obstructs the extraction of slowed atoms. The increasing field slower avoids this disadvantage. Its high field at the exit of the slower, interferes, however, with the operation of a magneto-optical trap at the end of the slower, which is a frequently employed configuration. The spin-flip slower, which corresponds to the Zeeman slower configuration used in our experimental setup (see section 3.2.2), combines off-resonant slower light with moderate magnetic field strength at its exit. It is in general considered to be much more compatible with the operation of a magneto-optical trap. In addition, its maximum field strength is lower than either one of the decreasing or increasing field slower, which significantly reduces the technical challenge of producing sufficiently strong magnetic fields.

2.2.7 Doppler cooling and optical molasses

By irradiating an atomic sample from different directions with resonant laser beams it is possible to establish a dissipative light force within the intersection of the beams that hinders the atomic motion and drastically reduces the atomic velocities inside the sample. This process, which was independently proposed in [93, 94], is known as *Doppler cooling*, as it relies on the velocity dependence of the scattering force, which originates from the Doppler effect. The radiative damping of the atomic motion is under optimal conditions strong enough to coerce the atoms into a diffusive Brownian motion, resulting in a quasi-confinement of the atoms. Due to the resemblance of the atomic motion to the motion of an extended object in a viscous fluid, such a configuration has been termed *optical molasses* [40, 95].

In its simplest form an optical molasses consists of a single pair of counter-propagating laser beams with intensity I_B and detuning δ_L from an atomic resonance. Such a configuration is known as one-dimensional molasses. An atom passing through the beams with velocity $\mathbf{v}$ is subject to the scattering forces exerted by each of the molasses beams. Suppose that the two laser beams are aligned with the z-axis, having wave vectors $\mathbf{k}_1 = k_\mathrm{L} \cdot \mathbf{e}_\mathrm{z}$ and $\mathbf{k}_2 = -\mathbf{k}_1$, respectively. For the respective effective detunings δ_1 and δ_2 of the beams holds with (2.11)

$$\delta_1 = \delta_\mathrm{L} - k_\mathrm{L} v_\mathrm{z} \tag{2.17}$$

$$\delta_2 = \delta_\mathrm{L} + k_\mathrm{L} v_\mathrm{z} \tag{2.18}$$

Here, v_z denotes the z-component of the atomic velocity $\mathbf{v}$, which represents the component of the atomic motion that is directed along the optical molasses. Inserting $\mathbf{k}_1$, $\mathbf{k}_2$, δ_1 and δ_2 in the expression of the scattering force stated in equation (2.12), one obtains for the resulting molasses force $\mathbf{F}_\mathrm{mo}$:

$$\mathbf{F}_\mathrm{mo} = \mathbf{F}_\mathrm{sc}(\mathbf{k}_1, \delta_1) \ + \ \mathbf{F}_\mathrm{sc}(\mathbf{k}_2, \delta_2) \tag{2.19}$$

$$= \hbar \mathbf{k}_\mathrm{L} \frac{\Gamma}{2} \frac{I_\mathrm{B}}{I_\mathrm{S}} \left[\left(1 + \frac{I_\mathrm{B}}{I_\mathrm{S}} + 4 \frac{(\delta_\mathrm{L} - k_\mathrm{L} v_\mathrm{z})^2}{\Gamma^2} \right)^{-1} - \left(1 + \frac{I_\mathrm{B}}{I_\mathrm{S}} + 4 \frac{(\delta_\mathrm{L} + k_\mathrm{L} v_\mathrm{z})^2}{\Gamma^2} \right)^{-1} \right]. \tag{2.20}$$

This approach is only accurate for small laser intensities ($I_\mathrm{B} \ll I_\mathrm{S}$) or uncorrelated laser beams, as it requires that the interaction of an atom with each of the light fields can be treated independently. Assuming low atomic velocities, thus $(k_\mathrm{L} v_\mathrm{z})^2 \ll \delta_\mathrm{L}^2$, (2.20) above can be simplified via an expansion in powers of $(k_\mathrm{L} v_\mathrm{z})/\Gamma$, which yields [95]

$$F_\mathrm{mo} \approx -\alpha v_\mathrm{z}, \tag{2.21}$$

with the damping constant α given by

$$\alpha = 4\hbar\, k_\mathrm{L}^2 \,\frac{I_\mathrm{B}}{I_\mathrm{S}} \,\frac{-2\,\delta_\mathrm{L}/\Gamma}{\left(1+(2\,\delta_\mathrm{L}/\Gamma)^2\right)^2}\,. \tag{2.22}$$

When the molasses beams are red-detuned ($\delta_\mathrm{L} < 0$), equation (2.21) and (2.22) describe a force that is linear in and opposite to v_z. Thus, $\mathbf{F}_\mathrm{mo}$ acts as an one-dimensional damping force, which dissipates the kinetic energy E_z that is associated with v_z. If the molasses beams are, on the other hand, blue-detuned ($\delta_\mathrm{L} > 0$), $\mathbf{F}_\mathrm{mo}$ will always accelerate the atoms. In the following, the latter case will be omitted by requiring $\delta_\mathrm{L} < 0$. The rate by which $\mathbf{F}_\mathrm{mo}$ dissipates kinetic energy is given by

$$\left(\frac{\mathrm{d}E_\mathrm{z}}{\mathrm{d}t}\right)_\mathrm{diss} = \frac{m}{2}\,\frac{\mathrm{d}v_\mathrm{z}^2}{\mathrm{d}t} = v_\mathrm{z}\,\frac{\mathrm{d}p_\mathrm{z}}{\mathrm{d}t} = \mathbf{v}\cdot\mathbf{F}_\mathrm{mo} = -\alpha v_\mathrm{z}^2. \tag{2.23}$$

Equation (2.23) constitutes a differential equation that describes an exponential decay of the kinetic energy. The decay is governed by the molasses damping time τ_mo, for which holds

$$\tau_\mathrm{mo} = \frac{m}{2\alpha}. \tag{2.24}$$

In the limit of low velocity values of v_z, equation (2.23) does no longer adequately describe the evolution of the kinetic energy inside the optical molasses. As outlined in section 2.2.4, the scattering force, on which the molasses force is based, represents merely an average over many cycles of photon absorption and re-emission. The stochastic nature of both processes induces inherent fluctuations in the momentum transfer rate, which have to be taken into account for an improved description of the optical molasses. Analogue to diffusion in momentum space, these force fluctuations cause a broadening of the momentum distribution that counteracts the dissipative removal of kinetic energy described in equation (2.23).

A treatment of the broadening that describes the fluctuations as random forces as part of a Fokker-Planck-equation is provided in [77]. The fluctuation can also be understood to cause the atom to undergo a random walk in momentum space [78, 95]. The absorption of a photon from one of the molasses beams changes the atomic momentum along the molasses axis p_z by an amount $\hbar k_\mathrm{L}$. The recoil from the spontaneous emission of a photon changes p_z by an amount between 0 and $\hbar k_\mathrm{L}$, depending on the actual direction of the emission. The rate of displacement in momentum space scales with the square root of the photon scattering rate R_sc, which is obtained from equation (2.12) by inserting $2I_\mathrm{B}$ as light intensity

I_L in order to account for two laser beams. The gain in kinetic energy due to the broadening of the momentum distribution can then by written as

$$\left(\frac{\mathrm{d}E_z}{\mathrm{d}t}\right)_{\mathrm{fluc}} = \underbrace{R_{\mathrm{sc}}\frac{\hbar^2 k_L^2}{2m}}_{\text{absorption}} + \underbrace{\chi R_{\mathrm{sc}}\frac{\hbar^2 k_L^2}{2m}}_{\text{spont. emission}} . \tag{2.25}$$

The dimensionless factor χ depends on the emission characteristic of the spontaneous emission. It is given by the average over the angular distribution of the emission. For isotropic emission in three-dimensional space χ evaluates to 1/3, for dipole emission to 2/5 and for truly one-dimensional emission to 1 [95].

Provided that the retention time inside the molasses is sufficiently long compared to the damping time τ_{mo}, it can be expected that the atoms reach a steady state, in which the loss of kinetic energy compensates the gain in kinetic energy such that the kinetic energy E_z remains constant. The condition for a steady state demands

$$\left(\frac{\mathrm{d}E_z}{\mathrm{d}t}\right)_{\mathrm{fluc}} + \left(\frac{\mathrm{d}E_z}{\mathrm{d}t}\right)_{\mathrm{diss}} = \left(1+\chi\right) R_{\mathrm{sc}}\frac{\hbar^2 k_L^2}{2m} - \alpha v_z^2 \overset{!}{=} 0 . \tag{2.26}$$

It can be shown that in the steady-state of the optical molasses, v_z is distributed according to a Maxwell-Boltzmann distribution [77]. The associated steady-state temperature T_z can be derived from equation (2.26) by solving for v_z^2. It should be noted here that T_z describes only the velocity distribution along the z-axis, devoid of any propositions about the other degrees of freedom. In the truly one-dimensional case it follows with $\chi = 1$ from equation (2.12), (2.22) and (2.26)

$$k_B T = \frac{\hbar\Gamma}{4}\,\frac{1+(2\delta_L/\Gamma)^2}{2\,|\delta_L|\,/\Gamma} . \tag{2.27}$$

As with the derivation of the damping constant α, it is assumed here that $I_B \ll I_S$. The right hand side of equation (2.27) is minimal for $\delta_L = -\Gamma/2$. Its minimum value defines the Doppler temperature T_D, which reads

$$T_D = \frac{\hbar\Gamma}{2k_B} \tag{2.28}$$

For the main cooling transition of ^{52}Cr, T_D evaluates to 120 μK , which corresponds to an rms velocity of $0.14\,\mathrm{m\,s^{-1}}$.

The Doppler temperature T_D, which is defined by equation (2.28), has been derived from a strictly one-dimensional scenario, where the respective recoils from absorption and spontaneous emission has been restricted to the axis of the molasses. The obtained result is, however, identical with the minimum temperature achievable by Doppler cooling in a three-dimensional molasses that is formed by three intersecting and mutual orthogonal pairs of molasses beams.

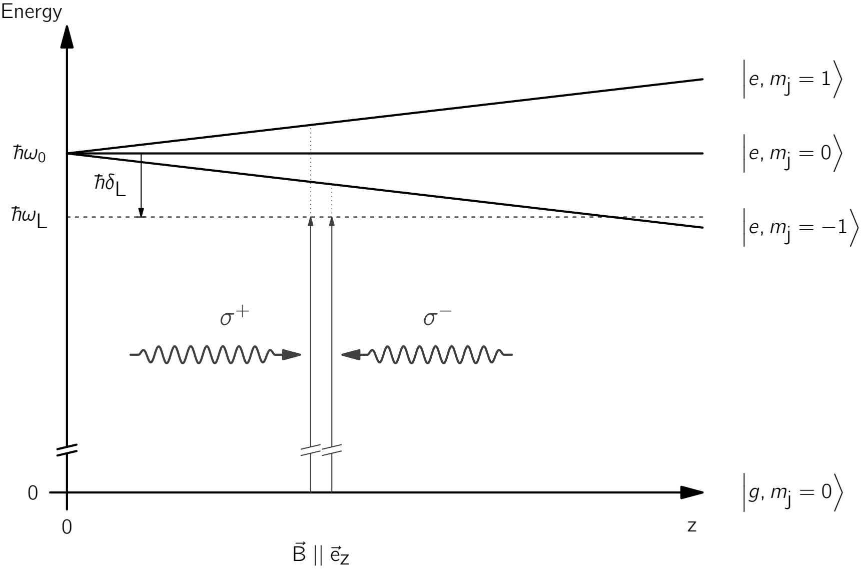

Figure 2.5: Illustration of the operating principle of a magneto-optical trap (MOT). Along the z-axis, a magnetic field $\mathbf{B}\,||\,\mathbf{e}_z$ with constant magnitude of the field gradient lifts the degeneracy of Zeeman substates that belong to a cooling transition with resonance ω_0. The field has a zero crossing at $z=0$, which marks the centre of the trap. A pair of counter propagating circular polarised laser beams with detuning $\delta_L < 0$ forms a radiation field in which radiation that is directed away from the MOT is σ^+-polarised, while radiation directed toward the MOT centre is σ^--polarised. The σ^--line is shifted by the magnetic field closer to the frequency of the MOT beams, while the σ^+-line is shifted away from it. This leads to an imbalance of the scattering forces exerted by the each of the MOT beams. Thereby, a net optical force is generated that has a velocity dependent dissipative and a spatially dependent confining component.

In practise, it is possible to observe in an optical molasses temperatures that are lower than T_D. The processes that lead to these temperatures are, however, different from the low intensity Doppler cooling discussed so far. They are denoted by the term *Sub-Doppler cooling* and require higher light intensities and suitable polarisations of the light field such that the degeneracy between different Zeeman sublevels is lifted by the dipole force [95].

2.2.8 Magneto-optical trap

The magneto-optical trap (MOT) can be regarded as an extension of the optical molasses concept discussed in section 2.2.7. Depending solely on the atomic velocity, and thus lacking a spatially dependent restoring force component, the optical molasses force represented by equation (2.21) is insufficient for a true confinement of atoms. The MOT, in contrast, allows confinement and cooling of atoms at the same location, resulting in a vastly improved accumulation and atom yield as compared to a conventional optical molasses. The MOT has been realised shortly after the first optical molasses [43], and has since become a versatile standard tool for the preparation of ultra-cold atom samples for a wide range of atomic species.

Similar to the Zeeman-slower presented in section 2.2.6, the MOT uses Zeeman-shifts inside a static magnetic field in conjunction with a resonant radiation field in order to produce a spatially dependent confining optical force component. Figure 2.5 illustrates the generation of the confining force component in the case of a one-dimensional MOT, which is oriented along the z-axis and centred at the origin. The MOT comprises a magnetic field $\mathbf{B}(z)$ with

$$\mathbf{B}(z) = b|z| \cdot \mathbf{e}_{\mathrm{z}}\,, \tag{2.29}$$

where b is a constant.

The MOT field lifts the degeneracy of Zeeman-sublevels along the z-axis. In the figure, the respective energies of the $m_{\mathrm{J}} = 0$ ground state and the $m_{\mathrm{J}} = \{-1, 0, 1\}$ excited states that belong to a cooling transition with resonance ω_0 are plotted over the atomic position z. The induced shift ω_{zm} of a Zeeman-line with angular momentum transfer Δm_{J} is proportional to $|z|$ and can with equation (2.4) and (2.29) be expressed as

$$\omega_{\mathrm{zm}} = \Delta m_{\mathrm{J}}\, \beta\, z\,, \tag{2.30}$$

with

$$\beta = \frac{g_{\mathrm{J}}^{*}\, \mu_{\mathrm{B}}\, |b|}{\hbar}\,. \tag{2.31}$$

The radiation field of the MOT is generated by a laser beam configuration which is akin to that of a one-dimensional optical molasses, in that it consists of a pair of counter-propagating laser beams with detuning $\delta_{\mathrm{L}} < 0$. These MOT beams, denoted with indices 1 and 2, are aligned with the z-axis and possess wave vectors $\mathbf{k}_1 = k_{\mathrm{L}} \cdot \mathbf{e}_{\mathrm{z}}$ and $\mathbf{k}_2 = -\mathbf{k}_1$, respectively.

A key difference to an optical molasses [4] is that we require the MOT beams to possess distinct circular polarisations, such that the radiation that propagates toward the centre of the MOT (at $z = 0$) is σ^{-}-polarised and the opposing, outward oriented radiation, σ^{+}-polarised. This condition can be met by exploiting that $\mathbf{B}(\mathrm{z})$ has a zero crossing at the origin, where it reverses its direction. As a result, the projection of the helicity of a photon travelling along the z-axis, on the magnetic field, which determines the kind of Zeeman transition that can be excited, reverses its sign at the origin.

At a given position z each of the MOT beams interacts by design only with a single distinct Zeeman-transition. We can therefore resort to the expression for the scattering force of the two-level atom stated in equation (2.12) in order to represent the net optical MOT force $\mathbf{F}_{\mathrm{mot}}$. For $\mathbf{F}_{\mathrm{mot}}$, which is given by the sum of the scattering forces exerted by each beam, respectively, thus holds

---

[4] Assuming that the effect of polarisation gradients can be neglected, as, for example, in the case of low light intensities.

$$\mathbf{F}_{\mathrm{mot}} = \mathbf{F}_{\mathrm{sc}}(\mathbf{k}_1, \delta_1) \;+\; \mathbf{F}_{\mathrm{sc}}(\mathbf{k}_2, \delta_2)\,. \tag{2.32}$$

Here, the effective detunings δ_1 and δ_2 depend not only on the velocity but also on the local Zeeman-shift induced by the magnetic field, expressed by equation (2.31). Thus we obtain

$$\delta_1 = \delta_{\mathrm{L}} - \beta z - k_{\mathrm{L}} v_{\mathrm{z}} \tag{2.33}$$

$$\delta_2 = \delta_{\mathrm{L}} + \beta z + k_{\mathrm{L}} v_{\mathrm{z}}\,. \tag{2.34}$$

Inserting the above expressions for the effective detunings into equation (2.32) and assuming low laser intensities ($I_{\mathrm{B}} \ll I_{\mathrm{S}}$) as well as small effective detunings, such that holds $\left(k_{\mathrm{L}} v_{\mathrm{z}} + \beta z\right)^2 \ll \delta_{\mathrm{L}}^2$, a simplified expression for F_{mot} can be obtained, such that

$$F_{\mathrm{mot}} \approx -\alpha v_{\mathrm{z}} - \frac{\alpha\beta}{k_{\mathrm{L}}} z\,. \tag{2.35}$$

The above equation describes the force of a damped harmonic oscillator, with the damping constant α defined by equation (2.22). In a typical configuration the motion of the atom is over-damped. Atoms entering the MOT thus quickly loose kinetic energy, while drifting toward the centre of the trap to be confined by the harmonic potential. As in the case of the optical molasses the stochastic nature of the scattering force imposes a limit on the cooling inside a MOT that is comparable to the Doppler limit.

An extension of the simple one-dimensional model provided in figure 2.5 to a two or three dimensional MOT is possible by adding complimentary MOT beams along the other coordinate axes. In addition, the magnetic MOT-field has to be extended in a manner that permits the existence of a suitably polarised radiation field. The standard choice of the MOT-field is a 2D or 3D quadrupole field. A quadrupole field has with the one-dimensional field in common, that its magnitude increases linear with the distance from the origin and that the field is invariant under a 180° rotation (C_2-Symmetry).

2.2.9 The optical dipole force

Off-resonant electromagnetic radiation interacts with an atom via a dynamic electric dipole moment that is induced by the oscillating electric field of the radiation. The interaction energy, which depends on the local intensity of the optical field, constitutes a potential $U_{\mathrm{d}}(\mathbf{r})$, from which a conservative optical force, the optical dipole force $\mathbf{F}_{\mathrm{d}}(\mathbf{r})$, is derived.

In the following, we consider an atom that is subject to monochromatic radiation with frequency ω and intensity I_{L}. The radiation comprises an oscillating electric field $\mathbf{E}(\mathbf{r}, t)$ with local electric field amplitude $E_0(\mathbf{r})$ and unit vector of polarisation $\mathbf{e}_{\mathrm{p}}$. Using the dipole approximation for the electric field, thus neglecting the spatial variation of its phase, we can represent $\mathbf{E}(\mathbf{r}, t)$ by

$$\mathbf{E}(\mathbf{r}, t) = E_0(\mathbf{r}) \cos(\omega t)\, \mathbf{e}_{\mathrm{p}} \tag{2.36}$$

The interaction between the electric field and the dipole moment of the atom is described by an interaction Hamiltonian $\hat{H}_{\text{int}}$. Using the electric dipole operator $\hat{\mathbf{D}} = e\,\hat{\mathbf{r}}$, $\hat{H}_{\text{int}}$ can be expressed as

$$\hat{H}_{\text{int}} = -\mathbf{E}(\mathbf{r},t)\cdot\hat{\mathbf{D}} = -e\,E_0(\mathbf{r})\cos(\omega t)\,\mathbf{e}_{\text{p}}\cdot\hat{\mathbf{r}} \tag{2.37}$$

It should be noted here, that the position operator $\hat{\mathbf{r}}$ is defined in the rest frame of the atom, acting on the atomic wave function. It must not be confused with the atomic position $\mathbf{r}$ in the laboratory frame.

The interaction Hamiltonian $\hat{H}_{\text{int}}$ constitutes a perturbation of the atomic zero field Hamiltonian $\hat{H}_0$. An atom initially in an undisturbed eigen state $|\iota\rangle$ of $\hat{H}_0$ with eigen energy E_ι that is then subject to the perturbing electric field is transferred to an amended state $|\tilde{\iota}\rangle$, which in general is no longer an eigen state of $\hat{H}_0$. The resulting shift ΔE_ι^{ac} of the atomic energy, is, being caused by an oscillating electric field, termed AC-Stark shift, in analogy to the conventional Stark shift [76], which is induced by a static electric field. It is given by the expectation value of the interaction Hamiltonian with respect to the amended state $|\tilde{\iota}\rangle$

$$\Delta E_\iota^{ac} = \langle\tilde{\iota}|\,\hat{H}_{\text{int}}\,|\tilde{\iota}\rangle\,. \tag{2.38}$$

The temporal evolution of $|\tilde{\iota}\rangle$ is governed by the time dependent Schrödinger equation with an effective Hamiltonian $\hat{H}_{\text{eff}} = \hat{H}_0 + \hat{H}_{\text{int}}$. Perturbation theory can be used to express the unknown disturbed wave function $|\tilde{\iota}\rangle$ in terms of an undisturbed basis of eigen vectors $|\kappa\rangle$, $\kappa \in \mathbb{N}$ of $\hat{H}_0$, with eigen energies E_κ, such that equation (2.38) can eventually be evaluated on the basis of known properties of $|\kappa\rangle$. For this purpose, we rely in the following on an approach outlined in [96] that is based on a Floquet state expansion of $\hat{H}_{\text{int}}$. Exploiting the periodicity of the perturbation, this treatment allows to apply the formalism of time independent perturbation theory to the dynamics induced by $\hat{H}_{\text{int}}$. Evaluating equation (2.38) with this approach, one finds that, due to the parity of atomic wave functions, all contributions to ΔE_ι^{ac} in the first order of the perturbation vanish. Considering also the second order contributions, one obtains

$$\Delta E_\iota^{ac} \approx -\frac{|\mathbf{E}_0(\mathbf{r})|^2}{4}\sum_{\kappa\neq\iota}\left|\langle\iota|\,e\,\mathbf{e}_{\text{p}}\cdot\hat{\mathbf{r}}\,|\kappa\rangle\right|^2\left(\frac{1}{E_\kappa - E_\iota - \hbar\omega} + \frac{1}{E_\kappa - E_\iota + \hbar\omega}\right). \tag{2.39}$$

The local intensity $I_{\text{L}}(\mathbf{r})$ of the light field is related to local electric field amplitude $\mathbf{E}_0(\mathbf{r})$ via

$$I_{\text{L}}(\mathbf{r}) = \frac{1}{2}\epsilon_0 c\,|\mathbf{E}_0(\mathbf{r})|^2\ , \tag{2.40}$$

where the field has been averaged over a full oscillation cycle. The AC-Stark shift thus defines an optical potential $U_{\text{d}}(\mathbf{r})$ and an associated optical dipole force $\mathbf{F}_{\text{d}}(\mathbf{r})$ that are proportional to the local light intensity and the gradient of the intensity, respectively, such that

$$U_{\text{d}}(\mathbf{r}) = \Phi_\iota(\omega,\mathbf{e}_{\text{p}})\;I_{\text{L}}(\mathbf{r}) \tag{2.41}$$

$$\mathbf{F}_{\text{d}}(\mathbf{r}) = -\Phi_\iota(\omega,\mathbf{e}_{\text{p}})\;\nabla I_{\text{L}}(\mathbf{r}) \tag{2.42}$$

The proportionality is defined by the coupling constant $\Phi_\iota(\omega,\mathbf{e}_\mathrm{p})$, which depends on the polarisation and the frequency of the radiation. It is derived from equation (2.39) and (2.40) and given by

$$\Phi_\iota(\omega,\mathbf{e}_\mathrm{p}) = -\frac{1}{2\epsilon_0 c\hbar}\sum_{\kappa\neq\iota}\left|\langle\iota|\, e\,\mathbf{e}_\mathrm{p}\cdot\hat{\mathbf{r}}\,|\kappa\rangle\right|^2\left(\frac{\sigma_{\iota\kappa}}{\omega_{\iota\kappa}-\omega}+\frac{\sigma_{\iota\kappa}}{\omega_{\iota\kappa}+\omega}\right) \tag{2.43}$$

Here, $\omega_{\iota\kappa}$ denotes the transition frequency obtained from $|E_\kappa - E_\iota| = \hbar\omega_{\iota\kappa}$. The symbol $\sigma_{\iota\kappa}$ represents the sign of the energy difference $E_\kappa - E_\iota$. It is defined by

$$\sigma_{\iota\kappa} = \begin{cases} +1, & \text{for } E_\kappa > E_\iota \\ -1, & \text{for } E_\kappa < E_\iota \end{cases} \tag{2.44}$$

2.2.10 Optical trapping of ^{52}Cr

The optical dipole potential presented in section 2.2.9 can be employed to trap atoms at the local intensity maximum of an optical field [42, 97], such as, for example, the focus of a Gaussian laser beam, provided that the coupling constant $\Phi_\iota(\omega,\mathbf{e}_\mathrm{p})$ given by (2.43) has the appropriate (negative) sign, and that the respective kinetic energies of the atoms do not exceed the effective depth of the trapping potential.

Traps that are based on the optical dipole potential are known as *optical dipole traps* (ODT). They have an advantage over magnetic traps, in that they are insensitive to an atom's magnetic polarisation, thus allowing the trapping of atoms in both high-field and low-field seeking states. This property plays a key role in the Bose-Einstein-condensation of ^{52}Cr, which due to the occurrence of strong atom losses that are induced by dipolar relaxation processes [98] can not be achieved in a purely magnetic trap [52]. Central to the understanding and the prediction of the properties of an ODT is the evaluation of the coupling constant $\Phi_\iota(\omega,\mathbf{e}_\mathrm{p})$, which in the following shall be outline for the case of ^{52}Cr.

In order to take the sum over the states represented by the wave functions $|\iota\rangle$ and $|\kappa\rangle$ in equation (2.43) we need to specify a suitable set of basis functions. As we are primarily interested in the case of ^{52}Cr, we choose atomic states that are according to the *LS*-coupling scheme represented in the usual manner by angular quantum numbers L, S, J and m_J, and by a radial wave function $\phi(r)$. Thus, we expand the initial wave function $|\iota\rangle$ into $|L^{(\iota)}, J^{(\iota)}, m_\mathrm{J}^{(\iota)}; \phi^{(\iota)}\rangle$ and in the same way $|\kappa\rangle$.

In addition, we can express the unit vector of polarisation $\mathbf{e}_\mathrm{p}$ in a spherical basis represented by a set of vectors $\mathbf{e}_\mathrm{q}$ with $q \in \{-1, 0, +1\}$ that in terms of Cartesian unit vectors are given by

$$\mathbf{e}_{+1} = -\frac{1}{\sqrt{2}}(\mathbf{e}_\mathrm{x} + i\mathbf{e}_\mathrm{y}) \qquad \mathbf{e}_0 = \mathbf{e}_\mathrm{z} \qquad \mathbf{e}_{-1} = \frac{1}{\sqrt{2}}(\mathbf{e}_\mathrm{x} - i\mathbf{e}_\mathrm{y}) \tag{2.45}$$

In this spherical representation $q = 0$ corresponds to linear π-polarised radiation, whereas $q = \pm 1$ corresponds to circular $\sigma^\pm$-polarised radiation, respectively.

It can be shown that, the operator $\mathbf{e}_\mathrm{p}\cdot\mathbf{r}$ transforms as a vector under rotations [77]. We can therefore apply the Wigner-Eckard theorem for vector operators [99] in order to evaluate the matrix element $\langle\iota|\mathbf{e}_\mathrm{p}\cdot\mathbf{r}|\kappa\rangle$ in equation (2.39). For the sake of clarity and brevity we assume in the following, that the radiation that generates the dipole trap is either π-, σ^+-, or σ^--polarised, such that its unit vector of polarisation is equal to $\mathbf{e}_\mathrm{q}$ with $q\in\{-1,0,+1\}$. In this special case the matrix element can be expressed in a compact form as

$$\langle\iota|\mathbf{e}_\mathrm{p}\cdot\mathbf{r}|\kappa\rangle = \left\langle L^{(\iota)}, J^{(\iota)}, m_\mathrm{J}^{(\iota)}; \phi^{(\iota)} \middle| e\,\mathbf{e}_\mathrm{q}\cdot\mathbf{r} \middle| L^{(\kappa)}, J^{(\kappa)}, m_\mathrm{J}^{(\kappa)}; \phi \right\rangle \tag{2.46}$$

$$= \underbrace{\left\langle J^{(\iota)}, m_\mathrm{J}^{(\iota)} \middle| J^{(\kappa)}, 1, m_\mathrm{J}^{(\kappa)}, q \right\rangle}_{=\,c_{\iota\kappa}} \underbrace{\left\langle \phi^{(\iota)}, J^{(\iota)} \middle| e\,r \middle| \phi^{(\kappa)}, J^{(\kappa)} \right\rangle}_{=\,d_{\iota\kappa}} \tag{2.47}$$

In the equation above the factor to the left abbreviated by $c_{\iota\kappa}$ represents a Clebsch-Gordan coefficient in the usual notation [99]. The other factor to the right, abbreviated by $d_{\iota\kappa}$, is known as *reduced matrix element* and does only depend on the radial extension of the wave function. It is connected with the line width $\Gamma_{\iota\kappa}$ and the resonance frequency $\omega_{\iota\kappa}$ of the transition between $|\iota\rangle$ and $|\kappa\rangle$ via

$$|d_{\iota\kappa}|^2 = 3\pi\epsilon_0\hbar c^3\,\frac{\Gamma_{\iota\kappa}}{\omega_{\iota\kappa}} \tag{2.48}$$

The corresponding values of the $\Gamma_{\iota\kappa}$ and $\omega_{\iota\kappa}$ can, in principle, be derived from numerical calculations. Alternatively, they might be obtained from spectroscopic measurements. The NIST Atomic Spectra Database maintained by the National Institute of Standards and Technology (NIST) provides a comprehensive listing of experimentally observed transitions [100].

Using equation (2.47) and (2.48) one obtains from equation (2.43) for the coupling constant of the optical dipole force

$$\Phi_\iota(\omega,p) = -\sum_{\kappa\neq\iota}\frac{3\pi c^2}{2}\,\frac{\sigma_{\iota\kappa}\,|c_{\iota\kappa}|^2}{\omega_{\iota\kappa}^3}\left(\frac{\Gamma_{\iota\kappa}}{\omega_{\iota\kappa}-\omega}+\frac{\Gamma_{\iota\kappa}}{\omega_{\iota\kappa}+\omega}\right). \tag{2.49}$$

The above expression can be readily evaluated for a given laser frequency ω and polarisation $\mathbf{e}_\mathrm{q}$ using tabulated spectroscopic data. With regard to our experimental work the case of the ^{52}Cr ground state subject to a an optical dipole trap laser with a wavelength of 1070 nm ($\omega = 1760\,\mathrm{THz}$) is of special interest. As the detuning of the trap laser from the principle resonances that can be excited from ground state is much larger than the fine-structure splitting of the associated levels, one finds that the final result for $\Phi_\iota(\omega,p)$, after summing over all J-levels, displays only a weak dependence on the angular properties of both the initial state and the trap laser. We therefore obtain from equation (2.49) a result, which is within the quoted 2σ-precision valid for all initial m_J-levels of the ground state and all laser polarisations. It is denoted by $\Phi_{|g\rangle}$ and reads

$$\Phi_{|g\rangle}\Big|_{\omega=1760\,\mathrm{THz}} = (\text{-}2.76 \pm 0.13)\cdot 10^{\text{-}37}\,\mathrm{m}^2\,\mathrm{s}\,. \tag{2.50}$$

3 Experimental apparatus and methods

The following chapter presents the preparation and the characterisation of the magnetically guided ultra cold ^{52}Cr atom beam that constitutes the starting point of the experimental and the theoretical studies presented in this thesis. The experimental apparatus employed for our experiments is in part based on an earlier setup, which has been described in number of publications [72, 101, 102]. It should be noted, however, that in preparation for our experimental studies significant changes have been implemented in order to enhance the performance of the beam preparation and the measurement process that allowed us to successfully perform the experimental studies presented in chapter 5.

3.1 Laser systems setup

Our experiments require laser light for the excitation of the cooling transition and the repumping transition, which corresponds to wavelengths of 425.6 nm and at 663 nm, respectively. The light is provided by two different laser systems, one for each respective wavelength. In order to deliver optical radiation with precisely defined frequencies, polarisations and intensity distributions, both laser systems are stabilised to external frequency references derived from a chromium spectroscopy cell and from a passively stable optical resonator.

3.1.1 Laser source for the cooling transition at 425.6 nm

A schematic overview of the laser system for the excitation of the $^7\mathrm{S}_3 \longrightarrow {}^7\mathrm{P}_4$ cooling transition is presented in figure 3.1. As a primary light source we employ a commercial laser system consisting of a Coherent MBR 110 titanium-sapphire (Ti:sapph) laser that is optically pumped by a Coherent Verdi V18, a diode pumped solid state (DPSS) laser, which is based on a $\mathrm{Nd{:}YVO_4}$ laser crystal.

The Verdi pump laser delivers continuous wave (cw) radiation with a fixed wavelength of 532 nm and a total optical power of 17.8 W to the MBR laser, which in turn outputs cw laser light with a power of 3.2 W. The wavelength of the MBR is tunable and adjusted to 852 nm, at exactly twice the required final wavelength of 425.6 nm.

Second harmonic generation (SHG) is used to convert the radiation emitted by the MBR into radiation with half of the original wavelength. The conversion process takes places inside an self-built frequency doubling cavity, which contains a nonlinear lithium triborate (LBO) crystal. A comprehensive description of this cavity is provided by [103]. The mode of the doubling cavity is actively stabilised via a Hänsch-Couillaud locking scheme [104], which employs the reflection of the entering beam on the outer surface of the injection mirror to control the cavity length via a piezo mounted cavity mirror.

The frequency doubling cavity generates three outgoing beams, a main beam and two weaker side beams, with a combined total output power of about 1.1 W. The main beam, which

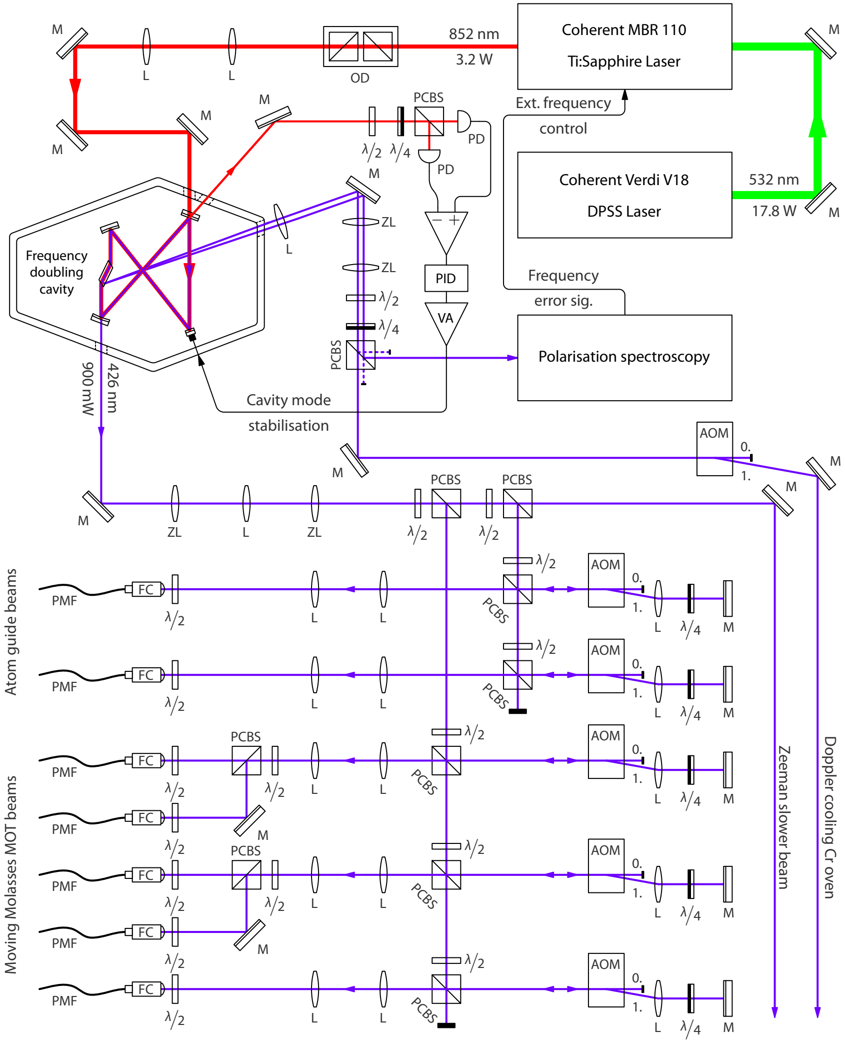
M
L
L
OD
852 nm
3.2 W
Coherent MBR 110
Ti:Sapphire Laser
M
M
M
M
PCBS
λ/2
λ/4
PD
PD
Ext. frequency
control
Coherent Verdi V18
DPSS Laser
532 nm
17.8 W
M
M
Frequency doubling cavity
L
ZL
ZL
λ/2
λ/4
PCBS
PID
VA
Frequency
error sig.
Polarisation spectroscopy
900 mW
426 nm
Cavity mode
stabilisation
AOM
0.
1.
M
M
M
M
ZL
L
ZL
PCBS
PCBS
λ/2
λ/2
Atom guide beams
Moving Molasses MOT beams
PMF
FC
λ/2
L
L
PCBS
AOM
0.
1.
λ/4
M
Zeeman slower beam
Doppler cooling Cr oven

Figure 3.1: Schematic overview of the laser system for the excitation of the cooling transition at 425.6 nm.

contains about 900 mW, is coupled out from the cavity through a partially transmissive dichroic cavity mirror. The two side beams, each with about 100 mW, emerge from internal reflections inside the LBO doubling crystal. They have mutually orthogonal polarisation states and are separated using a polarising cube beam splitter (PCBS).

One of the side beams is used to generates a frequency error signal via polarisation spectroscopy on a chromium spectroscopy cell, as outlined in see section 3.1.2. The spectroscopy cell serves as an absolute frequency reference to which the frequency of the side beam is compared. that is fed to the MBR in order to stabilise its the internal reference cavity. Via the MBR the frequency of the frequency doubling cavity thus locked to an atomic transition.

The other side beam is directed to the oven chamber at the bottom of the Zeeman slower in order to perform transverse Doppler cooling on the chromium atoms emerging from the chromium oven. An acousto-optical modulator (AOM) in single pass configuration is used to impose a fixed required frequency offset with respect to the atomic resonance. The transverse Doppler cooling reduces the transverse spread of atoms during the passage through the Zeeman-slower. It thus increases the atom yield of the moving molasses MOT (MMMOT) that is used to load the atom guide as outlined in section 3.3 by about a factor 20.

The remaining beams for the experiment are obtained output by dividing the main cavity beam into several sub-beams by means of rotatable half wave plates and PCBSs. Out of these sub beams, the Zeeman slower beam is the only one that is used without any modification of its frequency.

A total of five Acousto-optical modulators (AOMs) in double pass configurations are used to apply tunable frequencies offsets to the other sub beams. The double pass configuration avoids the frequency dependent deflection of the modulated beam that is present in the single pass configuration. The double pass AOMs thus offer five independently tunable frequency offsets for the experiments, three of which are used for the MMMOT, one which is used for the Doppler cooling inside the atom guide and one which is used for the imaging of the beam. In addition, the AOMs can be used to modulate the intensities of the passing light beams with bandwidths $> 10^5$ kHz via the power of the applied radio-frequency signal.

Polarisation maintaining optical fibres (PMFs) are used to deliver radiation from these beams to the experiment chamber, which is installed on a different optical table than the laser systems. In addition to eliminating beam pointing instabilities, the optical fibre's provide at the output well defined Gaussian intensity distributions, which proved to be critical for the operation of the MMMOT and for the Doppler cooling inside the guide . The alignment of the input polarisation with respect to the optical axis of a PMF is critical for the stability of the output polarisation. It is carried out using an alignment method presented in [105], which uses a rotating linear polariser. Monitoring the output of our PMFs under the influence of moderate temperature changes, as suggested in [106], we estimate that we can align the polarisation axis better than 2 °.

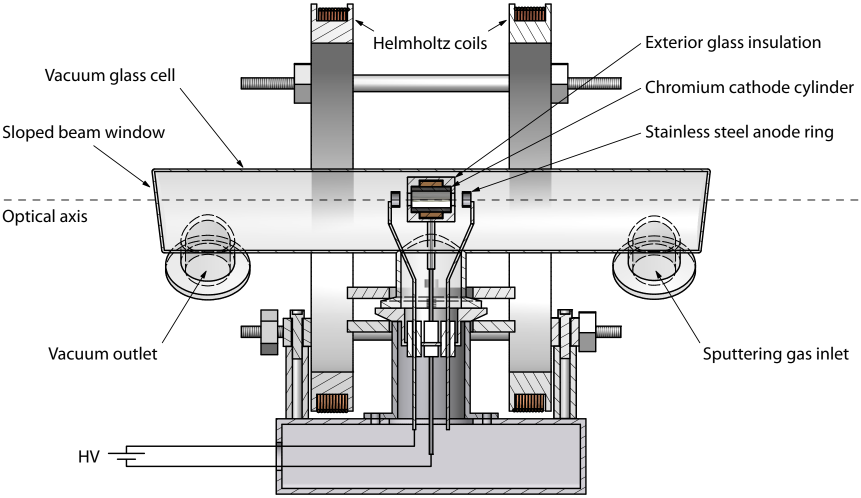

Figure 3.2: Illustration of the self-built chromium see-through hollow cathode lamp depicting a cross section along its optical axis. The glass cell contains argon or neon under low pressure. An electric voltage between the cylindrical cathode and the ring shaped anode ignites a plasma containing positively charged gas ions. The cathode is electrically insulated on the outside, such that the plasma can extend into the interior of the chromium cylinder. There, ions are accelerated toward the inner wands of cathode. Upon their impact, they sputter Cr atoms out of the surface, resulting in the formation of a chromium vapour that can be used to perform polarisation spectroscopy. For this purpose, the Helmholtz coils permit the application of a magnetic field along the optical axis.

3.1.2 Chromium spectroscopy cell

The MBR used for the generation of the cooling light features an internal reference cavity to which its mode can be locked via an internal servo. The locking results in a laser line width below 500 kHz, less than 10 % of the linewidth of the cooling transition, which is sufficiently narrow for our experiments.

The length of the internal reference cavity, and thus the central frequency of the laser, is, however, not sufficiently stable against thermal drifts. It is therefore actively stabilised via an external frequency error signal that is fed to the MBR through an external reference input, which controls the length of the reference cavity via an piezo mounted cavity mirror. We obtain an error signal by comparing the frequency of the light emitted by the doubling resonator with an absolute external frequency reference provided by the $^7S_3 \longrightarrow {}^7P_4$ transition in ^{52}Cr. Doppler free polarisation spectroscopy [79] on atomic vapour allows to perform a frequency comparison that yields an dispersive electronic signal proportional to the deviation of the light frequency from the atomic resonance.

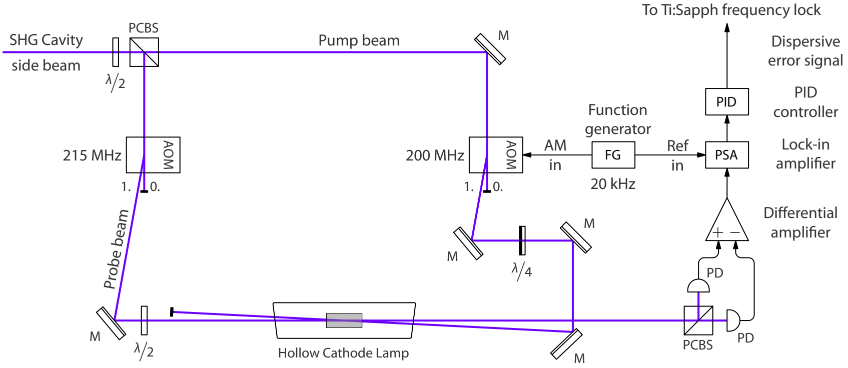
To Ti:Sapph frequency lock
SHG Cavity
side beam
PCBS
Pump beam
M
Dispersive
error signal
λ/2
PID
PID
controller
Function
generator
215 MHz
AOM
200 MHz
AOM
AM
in
FG
Ref
in
PSA
Lock-in
amplifier
1.
0.
1.
0.
20 kHz
Probe beam
M
M
Differential
amplifier
+
−
λ/4
PD
M
λ/2
Hollow Cathode Lamp
M
PCBS
PD

Figure 3.3: Polarisation spectroscopy on chromium vapour generated inside a hollow cathode lamp. The birefringence induced by optical pumping with a circularly polarised probe beam is queried by a linearly polarised probe beam and a pair balanced photo diodes after a polarising cube beam splitter. It yields a dispersive frequency error signal which is fed to the Ti:sapph laser in order to stabilise the output of the SHG cavity to the $^7S_3 \longrightarrow {}^7P_4$ transition in ^{52}Cr .

As a source of chromium atomic vapour we use a self-built hollow cathode lamp, shown in figure 3.2, which replaced a commercial hollow cathode lamp, which was reaching the end of its life time. The design of our self-built lamp corresponds to an earlier design described in [107]. An advantage of this design over the commercial lamp is that it features KF vacuum fittings, such that the pressure and the composition of the sputter gas can be varied in order to optimise the width and the signal to noise ration of the spectroscopy signal [108]. The glass cell is removable, which allows the cleaning of the cathode surface in order to restore a reliable ignition and a stable operation of the lamp.

Our experimental implementation for the polarisation spectroscopy is depicted in figure 3.3. We use a side beam from the frequency doubling cavity (see also figure 3.1), which is split into a pump and a probe beam. Both beams are passed through AOMs, which leads to a frequency offset between the resonance frequency in the hollow cathode lamp and the light emanating from the SHG cavity. For purely technical reasons the pump and the probe AOM operate at different frequencies, such that the frequency offset is given by the mean of the AOM frequencies.

In the vicinity of the atomic resonance, the circularly polarised pump beam induces a frequency dependent birefringence in the Cr-vapour that is produced inside the hollow cathode lamp. The induced birefringence is queried by the linearly polarised probe beam, whose polarisation axis is adjusted such that after the PCBS each of the two photo diodes picks up exactly the same amount of transmitted light. It can be shown [79], that the differential signal from the photo diodes then yields a dispersive error signal, which can be used to stabilise the reference cavity via the PID controller.

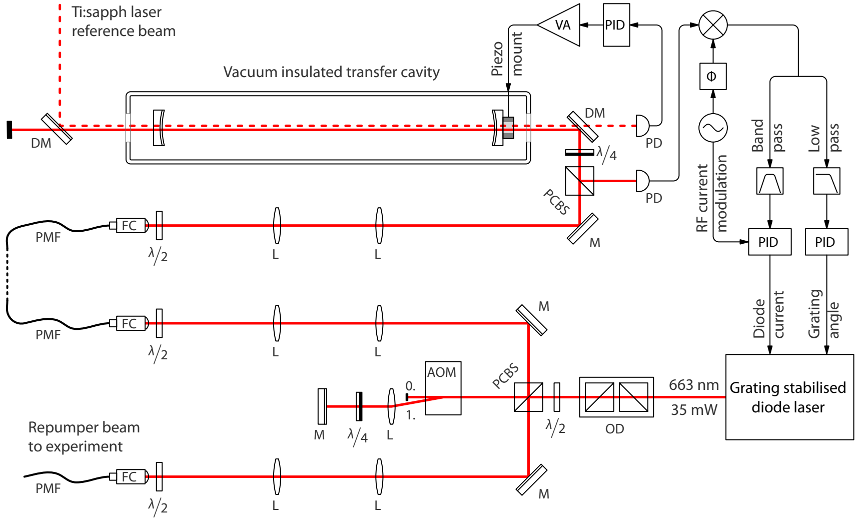
Ti:sapph laser
reference beam
Vacuum insulated transfer cavity
Piezo mount
VA
PID
DM
DM
PD
λ/4
PCBS
PD
M
FC
PMF
λ/2
L
L
FC
PMF
λ/2
L
L
M
RF current modulation
Φ
Band pass
Low pass
PID
PID
Diode current
Grating angle
AOM
0.
1.
PCBS
M
λ/4
L
λ/2
OD
663 nm
35 mW
Grating stabilised diode laser
Repumper beam to experiment
FC
PMF
λ/2
L
L
M

Figure 3.4: Schematic illustration of the repumper laser system. Laser light is delivered by an external cavity diode laser locked to an external optical resonator via the Pound-Drever-Hall technique. The lock uses a phase modulation of the emitted laser light, which is obtained from an RF-Modulation of the diode current. Demodulation of the signal obtained from light reflected from the resonator yields a dispersive error signal that is used to control the grating angle and diode current. Mounted inside a vacuum chamber, the external resonator is sufficiently stable to serve as passive reference cavity during most of our experimental work. Active stabilisation to a Ti:Sapph laser that is locked to an atomic transition is implemented via a side-of-fringe lock using the piezo mounted cavity mirror. In this case, the double pass AOM is employed to tune the diode laser on resonance with the repumping transition.

In order to improve the signal to noise ratio of the fairly weak signal from the polarisation spectroscopy, we modulate the amplitude of pump beam with an AOM at a frequency of 29 kHz and filter the error signal with a lock-in amplifier. [1]

3.1.3 Laser source for the repumping transition at 663.2 nm

Laser light for the repumping of atoms from the metastable state via the $^5\mathrm{D}_4 \longrightarrow {}^7\mathrm{P}_3$ transition is provided by a self-built external cavity diode laser, which in single mode operation emits cw radiation with a total power of about 35 mW at a wavelength of 663.2 nm. The laser is set up in a Littrow configuration [79], comprising an optical grating as a part of its external cavity, which reflects the first diffraction order back into the laser diode, thus serving as wavelength selective element. A piezoelectric actuator allows to adjust the grating angle in order to facilitate the tuning of the laser wavelength. The laser wavelength is also influenced by the laser diode current and the diode temperature, the latter of which is adjustable via a Peltier element.

---

[1] In contrast to earlier works we found that a modulation frequency above 29 kHz tends to deteriorate the signal, presumably as the optical pumping of Cr vapour does not proceed quickly enough.

3.1.4 Passively stable transfer cavity

The mode of the diode laser is locked to an external optical resonator via a Pound-Drever-Hall locking scheme [109], as illustrated in figure 3.4. For this purpose we modulate the laser diode current at a frequency of 10 MHz, which results in a phase modulation of laser light at the same frequency. The demodulation of the light reflected by the optical resonator then yields a dispersive error signal, which is used to control the laser frequency. The error signal is divided into a low frequency (<15 kHz) and a high frequency component, which are fed to the controllers of the grating angle and of the diode current, respectively.

A detailed description of the design and the construction of the external resonator is provided in [110]. The resonator is set up as a confocal cavity with a length of 1 m and a resulting free spectral range of 75 MHz. The cavity mirrors posses broad band dielectric coatings with a specified reflectivity of (99 ± 0.3) % for wavelenghts between 660 nm and 920 nm, which includes both the wavelength of the repumper as well as that of the Ti:Sapph laser. The resulting finesse of the resonator has been determined to be > 120 .

One of the cavity mirrors is mounted on a commercial linear piezo actuator with a maximum travel length of 6 µm , which allows scanning of the cavity length over several cavity fringes. The resonator is designed such that it can either act as a passively stable reference cavity or as an actively stabilised transfer cavity that is locked to a reference beam from a stable laser source. The piezo mount allows to fine tune the frequency of the laser by adjusting the length of the cavity while maintaining the mode of the laser locked. Alternatively the length of the cavity can be kept fixed with an external reference signal from the same Ti:Sapph laser that is employed for the generation of the light for cooling transition as described in section 2.2 and 3.1.2, while the laser frequency is tuned with an AOM.

Passive stability of the cavity is achieved by combining thermal insulation and low-thermal expansion materials. The spacing between the cavity mirrors is maintained by rods made out of Super-Invar, which is an alloy with an extremely low thermal coefficient of expansion. The resonator assembly is kept inside an elongated stainless steel vacuum chamber that is mounted on an damped optical breadboard, which is attached to the bottom side of the optical table that holds our laser systems. The vacuum provides thermal insulation and eliminates fluctuations of the optical path length due to disturbances in the ambient air.

The pressure inside the chamber is measured by a Pirani-type pressure gauge. The flanges and the valve of the chamber are Conflat (CF) sealed, which allows to maintain high vacuum (HVAC) conditions without having a (vibrating) mechanical pump attached to the chamber. Such low pressures are, however, not always required. It turned out that even a vacuum of much lesser quality, at around 10^{-1} mbar, provides enough passive stability to maintain the locked repumper laser resonant with the atoms inside the atom guide for times intervals exceeding 30 minutes, which proved to be sufficient for most of our experimental studies.

3.2 Vacuum apparatus

Handling of ultra cold matter demands scrupulous thermal insulation from its environment. Our experiments with ultra cold chromium atoms are therefore conducted in an ultra high vacuum (UHV) environment, which prevents collisions with background gas particles.

An overview of the vacuum chamber assembly that we employ for this purpose is provided in figure 3.5, which contains two perspective drawings, each representing a different view point. The assembly consists of three main components which are further described below. Ordered from bottom to top, these are the chromium oven chamber (section 3.2.1), the Zeeman slower (section 3.2.2), and the atom guide chamber (section 3.2.3).

The entire assembly is constructed to be UHV compatible with chamber parts made from stainless steel and connected by copper sealed CF-flanges. Optical access for laser cooling and imaging is provided by a number of vacuum viewports. These are made with standard Kovar sealing glass windows, except for the MOT beam viewports, which possess laser grade fused silica windows with custom made anti-reflection v-coatings for 425 nm.

Isolation against external vibrations is provided by an damped optical table, on which the assembly is mounted. The vacuum is, accordingly, sustained only by vibration free pumps: an ion and a titanium sublimation pump attached to the atom guide chamber and an ion pump attached to the oven chamber. Initial UHV conditions are established via a bake-out at 150 °C, during which the chamber is evacuated through an angle valve with a turbo-molecular pump. After the subsequent cool-out the valve is closed and the pump disconnected. The final vacuum pressure in the atom guide chamber is measured with an ionisation gauge and reads about $5 \cdot 10^{-10}$ mbar during our experiments.

3.2.1 Chromium oven chamber

The oven chamber provides the experiment with free chromium atoms. Located at the bottom of the vacuum chamber assembly, it is built around the oven cross, a 10-way vacuum cross with eight horizontal and two vertical ports. Attached to the bottom flange of the cross is an edge welded vacuum bellow which contains a commercial high temperature effusion cell. The bellow facilitates the alignment of the cell which emits an upward directed beam of chromium atoms through the Zeeman slower into the atom guide chamber. The cell operates with a calcium stabilised zirconia crucible that is filled with metallic chromium chips and heated radiatively. The crucible temperature is measured in situ with a Pt100 sensor and is controlled by a digital temperature controller with a stability better than ±0.5 °C. A water cooled heat shield surrounds the effusion cell and absorbs its waste heat. A circular outlet aperture in the upper face of the shield allows the ascending chromium beam to pass through the shield into the oven cross.

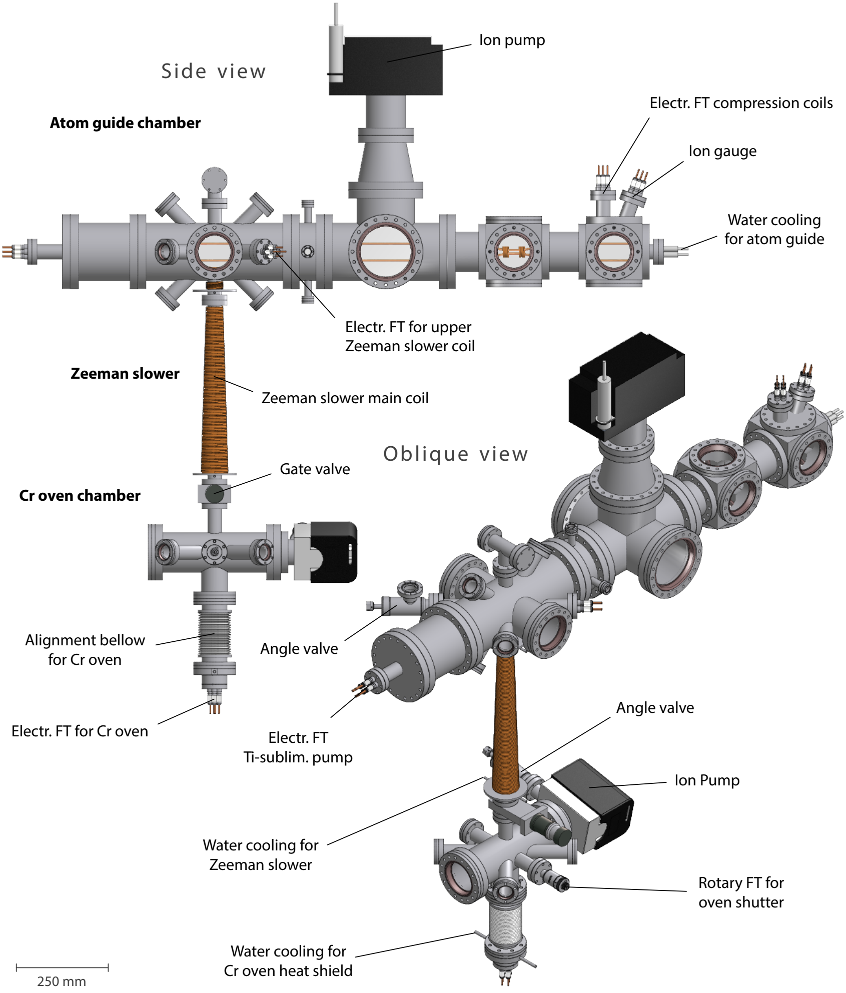
Side view
Atom guide chamber
Ion pump
Electr. FT compression coils
Ion gauge
Water cooling for atom guide
Electr. FT for upper Zeeman slower coil
Zeeman slower
Zeeman slower main coil
Oblique view
Gate valve
Cr oven chamber
Alignment bellow for Cr oven
Angle valve
Electr. FT for Cr oven
Electr. FT Ti-sublim. pump
Angle valve
Ion Pump
Water cooling for Zeeman slower
Rotary FT for oven shutter
Water cooling for Cr oven heat shield
250 mm

Figure 3.5: Perspective drawings of the UHV chamber assembly employed for our experiments with ultra cold Cr atom. The upper part of the assembly is formed by a horizontally oriented elongated chamber, the atom guide chamber, in which the MMMOT and the magnetic atom guide are operated. Free chromium atoms for the experiments are generated in the Cr oven chamber, located at the bottom of the assembly. Both chambers are interconnected by a vertically mounted Zeeman slower.

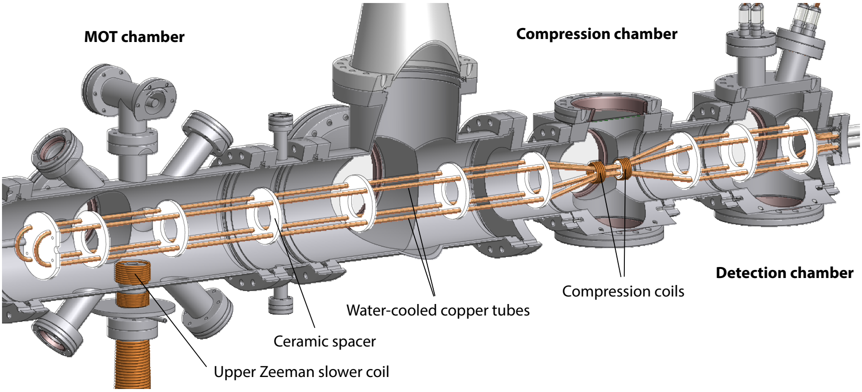

Figure 3.6: Cutaway drawing of the atom guide chamber depicting the magnetic atom guide and the magnetic coils inside the vacuum. The guide is formed from water cooled copper tubes held in place by ceramic spacers. The coils are wound from Kapton insulated copper wire retained by a vacuum compatible epoxy resin.

The oven cross offers lateral optical access to the beam, in particular throughout two orthogonal lines-of sights via four DN40 viewports mounted in a crossed configuration on opposing horizontal ports. It is employed for the collimation of the beam by operating a two-dimensional optical molasses transverse to the beam (analogue to [84]) at the centre of the cross. The beam can be blocked inside the oven chamber by a mechanical shutter that is activated via a rotary feedthrough mounted on one of the horizontal ports. A gate valve separates the oven chamber from the Zeeman slower. It is used to replenish the chromium in the effusion cell without breaking the vacuum in the Zeeman slower and the atom guide chamber. In this case the oven chamber is vented and evacuated though the angle valve at the rear port of the ion pump that is attached to the oven cross.

3.2.2 Zeeman slower

The Zeeman slower used in our experiment is a spin-flip type slower, which has been introduced in section 2.2.6. It has been adopted from an earlier experimental setup. Details on its design and on its construction are also given in [111].

A double walled tube forms the main core of the slower. It is water cooled and connected via DN40 flanges to the oven chamber at its bottom and to the atom guide chamber at its top. With a total length of 0.5 m and an inner diameter of only 15 mm the tube also acts as differential pumping stage between the oven and the atom guide chamber.

The magnetic field of the slower is generated by two Zeeman slower coils, an elongated main coil wound around the Zeeman slower tube, and a short upper coil, which is installed inside the atom guide chamber at the outlet of the Zeeman slower as shown in figure 3.6.

3.2.3 Atom guide chamber

The atom guide chamber is the principal part of the vacuum chamber assembly, due to the fact that it accommodates the magnetic atom guide, as depicted in figure 3.6 through a cutaway drawing. It is also the largest part of the vacuum chamber assembly, as shown in figure 3.5, with a total length of about 1.8 m.

The atom guide chamber consists of different chamber segments that are arranged in series along a central horizontal axis. Three of these segment, which play a central role with regard to our studies, are designated in figure 3.6. First, the MOT chamber, where the chromium atoms ascending from the Zeeman slower are transfered via a MMMOT into the magnetic atom guide (see section 3.3). Second, the compression chamber, where the transverse cooling of the guided atom beam is demonstrated (see section 5.1). Third, the detection chamber, where the physical properties of the transmitted atom beam are determined (see section 3.4).

The magnetic atom guide extends from the MOT chamber to the detection chamber along the central axis of the atom guide chamber. It is constructed from a pair of u-bend oxygen free copper tubes, which carry the electric current that generates the magnetic potential of the atom guide. The tubes each have an outer diameter of 6 mm and a bend radius of 23 mm. They are held in place by ceramic spacer disks, which also serve as electric insulators. The tube ends are each connected to a water cooled electric vacuum feedthroughs, which allows cooling water to circulate through the tubes in order to increase the maximum possible electrical current load.

The u-bend tubes are positioned side-by-side to each other, such that together they constitute the magnetic guide configuration presented in figure 2.2, with the linear tube segments serving as the quadrupole bars. The tubes are connected in series in such a way that the guide current flows through the bars in alternating opposing directions, which generates a two-dimensional magnetic quadrupole field along the central axis of the guide. Inside the MOT chamber the lateral spacing between neighbouring quadrupole bars measures 46 mm, which according to (2.8) yields a magnetic field gradient of $7.56 \cdot 10^{-2}\,\mathrm{G\,cm^{-1}}$ for a guide current of 1 A. Inside the compression chamber the lateral spacing between the bars is reduced over a length of 10 mm from 46 mm to 9 mm, which corresponds to a tapering of the magnetic guide, leading to a transverse compression of the atom beam. After a section with a length of 24 mm, the compression zone, where the spacing remains constant, the tapering of the guide is reversed, resulting in lateral spacing of 46 mm inside the detection chamber.

The compression zone is flanked by a pair of coils, the compression coils, which allow to apply a magnetic offset field inside the compression zone that is parallel to the axis of the guide, and thus perpendicular to the quadrupole field of the guide. The compression coils, whose centres are spaced 38 mm apart, each have a length of 14 mm and a diameter of 50 mm. They each posses 10 windings that are wound from Kapton insulated copper wires and are fixed with an UHV compatible epoxy resin.

3.3 Preparation of a magnetically guided ultra cold atom beam

The experimental apparatus described in section 3.1 and 3.2 allows us to prepare a high flux beam of ultra cold ^{52}Cr atoms inside the atom guide. For this purpose we employ an approach that is based on a variant of the MOT, the *moving molasses MOT* (MMMOT), which is a combination of one-dimensional optical molasses with two-dimensional MOT [70]. Following this approach, we have demonstrated the preparation of an ultra cold atom beam both in pulsed [101] and in continuous [72] mode. For the work presented in this thesis, however, only the continuous method is of relevance.

Starting point of the beam preparation is the effusion cell inside the oven chamber. We operate the cell at a temperature of 1600 °C in order to generate a hot beam of free chromium atoms. The emitted vertical atom beam is collimated by a transverse two-dimensional optical molasses, which narrows the transverse velocity distribution before the Zeeman slower. The result is an increase of the transferred atom flux by about one order of magnitude.

The optical molasses is created by two retro-reflected laser beams intersecting at a right angle above the outlet aperture of the effusion cell. Its laser light is red detuned with respect to the $^7S_3 \longrightarrow {}^7P_4$ cooling transition and has a total power of 50 mW, which is equally distributed between both laser beams.

The Zeeman slower is operated with a current of 11.1 A in the main coil and 12.6 A in the upper coil, respectively. The laser beam for the Zeeman slower has a total power of about 90 mW. It is directed into the Zeeman slower tube by a mirror inside the vacuum chamber. This prevents chromium atoms from coating the entrance viewport of the beam, which is mounted to a CF vacuum tee located on top of the MOT-chamber.

Atoms leaving the Zeeman slower are injected into the guide by a MMMOT consisting of three pairs of counter propagating laser beams that are mutually orthogonal and that intersect in a single point on the central axis of the magnetic guide. Two of the beam pairs are oriented diagonally at an angle of 45 ° with respect to the guide axis, while the third pair lies in the horizontal direction orthogonal to the guide.

The magnetic field for the MMMOT is the same as for the atom guide, which is useful in regard to the transfer of atoms from the MMMOT into the guide, as it avoids the necessity of mode-matching that is present in alternative experimental designs. It is generated by a guide current J_g of 177 A, which creates a magnetic field gradient of about 13.5 G/cm.

A relative detuning is applied between the counter propagating MOT beams in each diagonal beam pair. For atoms that move with a certain velocity v, the relative frequency detuning δ of the MOT beams vanishes due to the Doppler-shift. This corresponds to a MOT in a moving reference frame, which effectively cools the atoms into a non-zero velocity class. As a consequence, atoms can be launched into the guide with a selected velocity that is proportional to δ [70, 72].

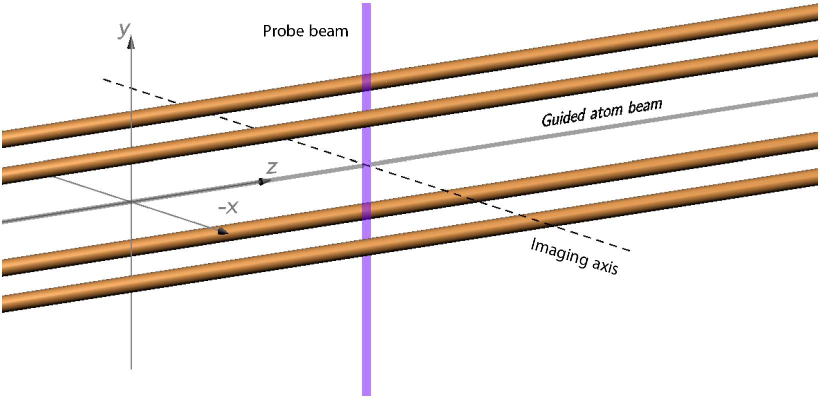

Figure 3.7: Illustration of the setup employed for the imaging of the guided atom beam. Atoms inside the guide are illuminated by retro-reflected probe beam aligned orthogonal to the atom beam along the vertical y-axis. Light scattered by the atoms is observed with a CCD-camera, which is oriented along the horizontal x-axis. The imaging axis intersects both the atom beam and the probe beam at a right angle, which suppresses the detection of stray light from the probe beam and simplifies the image analysis, in particular with regard to the spatial distribution of the atoms.

3.4 Atom beam characterisation

Our studies of the cooling with the optical molasses are based on the characterisation of the beam in terms of the total atom flux ρ, the beam velocity v_b, and the beam temperatures T_r and T_a that belong to the radial and the axial degrees of freedom, respectively. For the measurement of these quantities we employ optical detection methods that rely on the illumination of the beam with a near resonant probe beam of known intensity and on the imaging of the scattered photons with a calibrated CCD-Camera.

3.4.1 Imaging system

The characterisation of the atom beam is performed at the end section of the atom guide, which is located inside the detection chamber. As shown in figure 3.5, four DN63 vacuum viewports offer lateral optical access to the atom beam along a horizontal and a vertical axis. Figure 3.7 illustrates our setup for the imaging of the atom beam. Atoms propagating along the axis of the guide are illuminated by a probe beam, which runs vertically through the centre of the detection chamber. The probed atoms scatter light that is captured with a horizontally oriented CCD-camera. The placement of the probe beam and the CCD-camera is chosen such that the magnetic guide axis, the probe beam axis and the imaging axis mutually orthogonal. This configuration helps to minimise the detection of stray light from the probe beam. It also simplifies the analysis of the captured images.

Probe beam setup

We employ a probe beam that is resonant with the 426 nm cooling transition, which, as pointed out in section 2.1.3, is a practically closed transition that can be used scatter a multitude of photons per atom, resulting in a strong fluorescence signal.

A polarisation maintaining fibre delivers the probe beam from the laser system shown in figure 3.1 to the atom guide chamber. After the fibre outcoupler we pass the probe beam through a PCBS which results in a linear polarisation with a fixed polarisation axis. Inside the detection chamber, the probe beam is set up retro-reflected in a lin || lin configuration with the polarisation vector parallel to the guide axis. Thus, its polarisation is perpendicular to the magnetic field of the guide, which suppresses magnetic depolarisation of the atom beam as a result of optical pumping. Using a retro-reflected probe minimises the transfer of photon momentum to the probed atoms.

The optical fibre acts as spatial filter for the mode of the probe beam and yields a well-defined Gaussian beam profile. The total power of the probe beam is actively stabilised via a PID-controlled feedback loop, which is connected to the AM-input of the probe beam AOM. In order to obtain an approximately uniform probe beam intensity over a transverse cross section of the beam we expand the beam with a cylindrical lens telescope in one direction. The resulting elliptical Gaussian beam profile has of waist of 2.5 mm parallel and a waist of 13.1 mm transverse to the guide axis.

The strength of the fluorescence signal obtained from an atom inside the guide is proportional to the scattering rate R_{sc} defined in equation (2.10). For a probe with a narrow line width it depends therefore on the position of the atom inside the magnetic potential of the guide and on its velocity along the probe beam axis. (2.13) In order to obtain a signal that is independent of atomic position and velocity we utilise an artificial broadening of the probe beam by scanning its frequency far enough. By doing so every illuminated atoms emits, averaged over the exposure time of the camera, approximately the same number of photons. The fluorescence signal obtained from any given position inside the atom guide is therefore proportional to the local density of the atom beam.

The frequency scanning of the probe beam is realised by applying a linear ramp with a constant offset to the FM-input of the probe AOM. The offset is chosen such that the probe beam is resonant with the atoms at the centre of the guide, which experience practically no Zeeman shift. We use a ramp frequency of 800 Hz, which is large compared to the typical inverse exposure times used for taking spatially resolved images of the atom beam as discussed in section 3.4.2.

Camera system

Our measurements are all performed with the same CCD-camera, an iXon model 885 EMCCD camera from the manufacturer Andor, whose CCD-sensor features 1004 × 1002 pixels sized

8 µm ×8 µm . Peltier-cooling allows to maintain the temperature of the CCD below -80 °C during our measurements, which lowers the dark-noise of the CCD to a negligible level. The camera hardware supports vertical and horizontal binning of CCD-pixels, which we use to increase ratio between signal and CCD readout noise.

A 1:1 image of the illuminated atom beam is created by a camera objective consisting of a single plano-convex lens with a focal length of 75 mm and a diameter of 50 mm. We are only interested in the detection of photons with a wavelength of 426 nm. Thus we block stray light with a single-band optical bandpass filter that has a central wavelength of 427 nm and a bandwidth of 10 nm.

The camera is connected via a proprietary image acquisition board to a personal computer. An interpreter software is used to control the camera settings and the image acquisition via the *Andor Basic* script language. In order to perform automated series of measurements we trigger the camera via an external trigger signal. This allows us to synchronise the image acquisition with the other experimental settings that are controlled by the main experiment control computer.

3.4.2 Radial beam temperature

Knowledge about the distribution of energy in the transverse degrees of freedom can be obtained by measuring the lateral density of guided the atom beam. For this purpose we capture the fluorescence of the illuminated atom beam using the imaging system described in section 3.4.1.

In the employed configuration, the CCD-camera faces the atom beam from the side as shown in figure 3.7. The camera objective projects the fluorescence along the x-direction on to the CCD-sensor, which is oriented parallel to the yz-plane. The projection is 1:1, such that each object point shares with its corresponding image point the same respective yz-coordinates. We require the objective's depth of field to be large enough to cover the lateral extension of the atom beam. Then all points belonging to a straight line that is running parallel to the x-axis are mapped onto a single image point on the CCD-sensor. This is the 2D signal we acquire.

In order to determine the lateral density distribution $n(x, y)$ we regard only the CCD-signal along a vertical image section that corresponds to the z-position where the centre of the probe beam intersects with the atom guide axis. At this position, the fluorescence is approximately proportional to the atom beam density, such that for the CCD signal $s(y)$ that is obtained along the vertical y-direction holds

$$s(y) = s_0 \int\limits_{-\infty}^{\infty} dx\, n(x, y)\,, \tag{3.1}$$

with s_0 assigned to be a constant prefactor that accounts for the proportionality between the atom beam density and the observed CCD-signal.

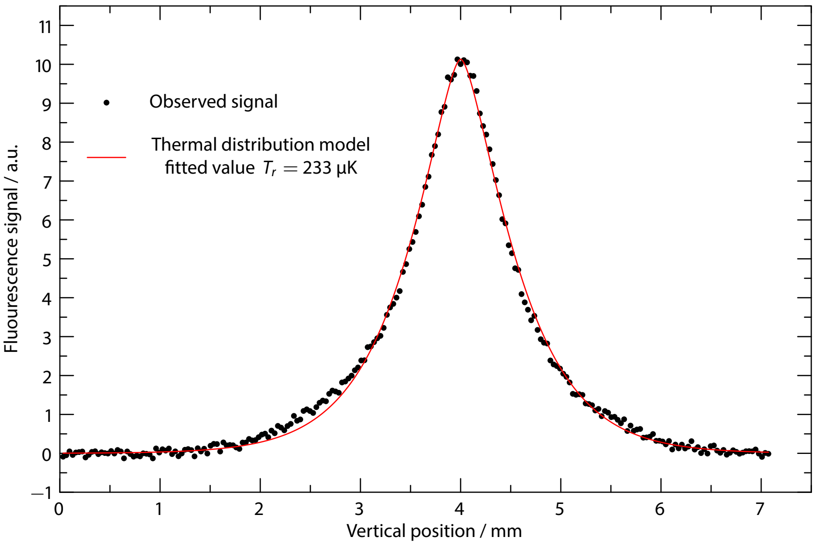

Figure 3.8: Measurement of the radial temperature T_r. A fluorescence image is taken with a CCD-camera in such a way that along the vertical axis the CCD-signal is proportional to the density of the atom beam integrated along the horizontal line-of-sight. We use non-linear regression to fit a model corresponding to a thermal radial density distribution (solid red line) to the observed fluorescence signal (black dots), which yields, according to equation (3.5) the radial beam temperature T_r as a fitted parameter.

For the analysis of the captured fluorescence images we make the heuristic assumption that the transverse positions and momenta are, as a result of the stochastic nature of the light forces inside the MMMOT, distributed according to a quasi-thermal distribution, as discussed earlier in section 2.2.1. The density distribution inside the atom guide then follows from the classical Hamiltonian $H\left(\mathbf{p},\mathbf{r}\right)$ of an atom with mass m and momentum $\mathbf{p}$ that is located inside a section of the guide with gradient b_g, which with equation (2.9) is given by [112]

$$H\left(\mathbf{p},\mathbf{r}\right) = \frac{\left|\mathbf{p}\right|^2}{2m} + m_\mathrm{J}\, g_\mathrm{J}\, \mu_\mathrm{B}\, b_\mathrm{g} \sqrt{x^2+y^2}. \tag{3.2}$$

Assuming that the atomic positions inside the guide are Boltzmann distributed according to a radial temperature T_r, the lateral density distribution $n(x,y)$ that is obtained from equation (3.2) reads

$$n(x,y) = \frac{\tilde{n}}{2\pi}\left(\frac{m_\mathrm{J}\, g_\mathrm{J}\, \mu_\mathrm{B}\, b_\mathrm{g}}{k_\mathrm{B}\, T_\mathrm{r}}\right)^2 \exp\left(-\frac{m_\mathrm{J}\, g_\mathrm{J}\, \mu_\mathrm{B}\, b_\mathrm{g}\sqrt{x^2+y^2}}{k_\mathrm{B}\, T_\mathrm{r}}\right), \tag{3.3}$$

where the constant $\tilde{n}$ represents the axial atom beam density to which $n(x,y)$ is normalised. Inserting equation 3.3 into equation 3.1 yields for the expected CCD signal

$$s(y) = \frac{s_0\, \tilde{n}}{2\pi}\left(\frac{m_\mathrm{J}\, g_\mathrm{J}\, \mu_\mathrm{B}\, b_\mathrm{g}}{k_\mathrm{B}\, T_\mathrm{r}}\right)^2 \int\limits_{-\infty}^{\infty} dx \exp\left(-\frac{m_\mathrm{J}\, g_\mathrm{J}\, \mu_\mathrm{B}\, b_\mathrm{g}\sqrt{x^2+y^2}}{k_\mathrm{B}\, T_\mathrm{r}}\right). \tag{3.4}$$

The integral above can be solved analytically [111], yielding

$$s(y) = \frac{s_0\, \tilde{n}}{\pi}\left(\frac{m_\mathrm{J}\, g_\mathrm{J}\, \mu_\mathrm{B}\, b_\mathrm{g}}{k_\mathrm{B}\, T_\mathrm{r}}\right)^2 y\, K_1\left(-\frac{m_\mathrm{J}\, g_\mathrm{J}\, \mu_\mathrm{B}\, b_\mathrm{g}}{k_\mathrm{B}\, T_\mathrm{r}}\, y\right). \tag{3.5}$$

The function K_1 represents a modified Bessel function of the second kind K_α with $\alpha = 1$, which is implemented as a special function in various numerical libraries.

Equation (3.5) represents a descriptive model that can be fitted to the CCD signal using T_r and the product $s_0\hat{n}$ as free fit parameters in order to deduce an estimate for the radial temperature T_r. An example of such a fit is provided in 3.8. It shows a conclusive agreement between the observed signal and the fitted model, which in retrospect justifies the choice of a thermal distribution as description for the radial density.

3.4.3 Beam velocity

The axial component v_z of the atomic velocity is distributed according to a distribution function $u(v_\mathrm{z})$ around mean velocity value, which represents the beam velocity v_b. As in the case of the radial density distribution, we assume that $u(v_\mathrm{z})$ is accurately described by quasi-thermal velocity distribution belonging to an axial temperature T_a. Inside the detection chamber of the atom guide there is no axial force component present. The axial

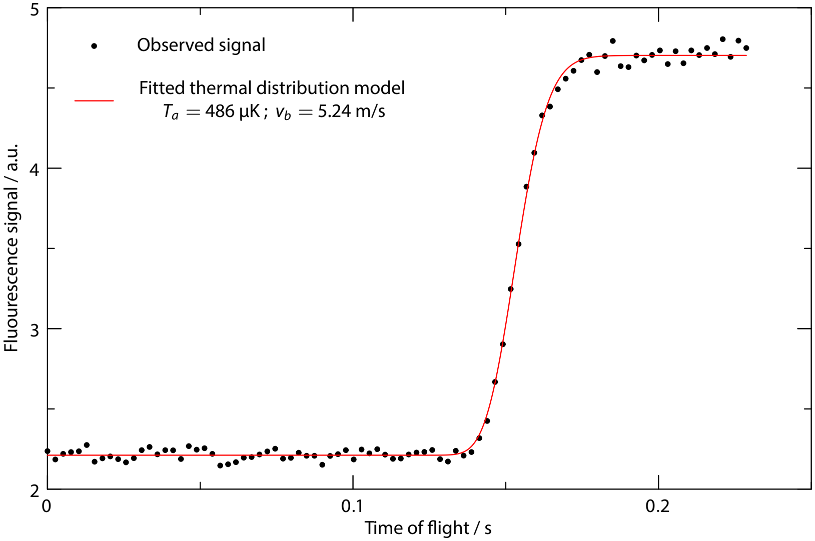

Figure 3.9: Measurement of the axial velocity distribution inside the guided atom beam by a time-of-flight method. The atom beam is blocked by a resonant laser beam some distance away from the point of observation. At the time $t = 0$ the atom beam is released. The observed fluorescence signal is recorded over time using a fast series of CCD camera frames. A descriptive model for the signal can be derived from a thermal Maxwell-Boltzmann distribution. Fitting the model presented by equation 3.8 to the time resolved signal yields an estimate for the longitudinal temperature T_r and for the average beam velocity $\mathrm{v_b}$.

velocity distribution is therefore given by a one-dimensional Maxwell-Boltzmann with mean velocity $\mathrm{v_b}$, which reads

$$u(\mathrm{v_z}) = \sqrt{\frac{m}{2\pi\, k_\mathrm{B}\, T_\mathrm{a}}}\, \exp\left(\frac{-m\left(\mathrm{v_z} - \mathrm{v_b}\right)^2}{k_\mathrm{B}\, T_\mathrm{a}}\right). \tag{3.6}$$

Using a time of flight measurement, it is possible retrieve the velocity distribution with the imaging system described in section 3.4.1. For this purpose we block the passage of atom through the atom guide beam at known distance d from the point of measurement. The block is implemented by directing resonant laser light from the side at the atom beam. The resonant light then exerts a lateral light force on the passing atoms that ejects them out of the atom guide. Thus the light acts a shutter that prevents the atom beam from further propagating into the guide. At the time $t=0$ we switch the atom beam block off. At the same moment we start to record the fluorescence of the atom beam with the CCD camera using the *kinetic series* mode of camera, which allows to take a fast series of frames, albeit only on a small sector of the CCD-sensor. From the recorded frames we obtain a fluorescence signal as a function of the observation time t by regarding the pixel count over a fixed region of interest (ROI) near the overall maximum of the fluorescence.

An example of such a time of flight measurement is provided in figure 3.9, where a series of 90 frames has been taken with a frame rate of 395 Hz at a distance of $d=0.84\,\mathrm{m}$ between the points of observation and release of the atom beam, respectively. The obtained fluorescence signal shall be described by a model function $s(t)$ that is derived from the atomic velocity distribution $u(\mathrm{v_z})$. At a time $t>0$ only atoms with an axial velocity $\mathrm{v_z} > d\,t^{-1}$ contribute to the signal, which can be expressed as

$$s(t) = s_0 + s_1 \int_0^\infty d\mathrm{v_z}\, u(\mathrm{v_z})\, \Theta\left(t - \frac{d}{\mathrm{v_z}}\right). \tag{3.7}$$

The constant s_0 represents the background signal that originates, for purely technical reasons, from the CCD-sensor itself, while the prefactor s_1 equals the maximum additional signal that is caused by the fluorescence of the atom beam.

The integral in equation 3.7 can be expressed in terms of the error function $\mathrm{erf}(x)$, which yields an closed expression for $s(t)$

$$s(t) = s_0 + \frac{s_1}{2} + \frac{s_1}{2}\,\mathrm{erf}\left[\sqrt{\frac{m}{2\, k_\mathrm{B}\, T_\mathrm{a}}}\left(\frac{d}{t} - \mathrm{v_b}\right)\right]. \tag{3.8}$$

Using $s(t)$ as a descriptive model for the experimental data, allows us to estimate T_a and $\mathrm{v_b}$. Figure 3.9 shows an example of a time-of-flight measurement. The observed signal has been fitted to $s(t)$ using s_0, s_1, T_a and $\mathrm{v_b}$ as free fit parameters. The apparent agreement between $s(t)$ and the data supports the choice of a model that is based on a thermal distribution.

3.4.4 Atom flux

The rate of atoms passing through a cross section of the atom beam defines the total atom flux φ. As each ground state atom scatters a certain number of photons upon passing the probe beam of our imaging setup, we can, in principle, deduce φ from the fluorescence that is emitted from the atom beam. In order to do so, we have to be able to determine the total photon emission rate R_{obs} from the observed fluorescence signal. In addition, we have to know how to relate R_{obs} to φ .

In order to be able to measure R_{obs}, we have calibrated the signal of our CCD-camera, including objective lens and optical filters, by using a laser beam of known intensity as a source of photons at 426 nm. Assuming isotropic emission and considering the solid angle that is covered by the objective lens, we can thus deduce the total number of photons emitted from the illuminated section of the atom beam during an exposure of the camera, which directly yields the value of R_{obs}.

The relation between R_{obs} and φ is for a given configuration of the probe beam and the atom beam determined by the average number of photons N_{ph} that are scattered by an atom during its passage through the illuminated section of the atom beam. Our probe beam is, as outlined in section 3.4.1, set up in such a way that N_{ph} is independent of the energy associated with the atom's transverse degrees of freedom. Moreover, we keep the geometry and the polarisation of the probe beams fixed during our studies. Thus, N_{ph} depends, aside from φ, only on the power P_{obs} of the probe beam and on the average axial velocity v_{obs} of the atom beam.

Using an atom beam with known atom flux φ_{ref} and known beam velocity v_{ref} as a reference, it is possible to determine the relation between R_{obs} and φ from experimental observation. We prepare such a reference atom beam by starting from a beam that consists predominantly out of meta-stable atoms, which can be obtained by finely adjusting the settings of the MOT-beams. Any remaining ground state atoms are then removed using lateral illumination with resonant laser light. In the final step, we use optical pumping via the $^5\text{D}_4 \longrightarrow {}^7\text{P}_3$ transition with laser light at 663 nm provided by the repumping laser system described in section 3.1.3 i n order to generate a ground state atom beam from the meta-stable atom beam. The repumping proceeds with the emission of exactly one photon at 428 nm per generated ground state atom. The repumping beam is positioned in such way such that the repumping takes place within the field of view of our imaging system. Hence, we are able to the infer the ground state atom beam flux P_{ref} from the measured rate of emitted photons during the repumping.

Subjecting the reference atom beam to the probe beam light yields us the atom beam velocity v_{ref} and the photon emission rate R_{ref}. We expect the photon emission rates R_{ref} and R_{obs} to increase proportional to the respective probe beam powers P_{ref} and P_{obs}, as we keep the probe beam intensity well below the saturation intensity during our studies. Furthermore, we expect the R_{ref} and R_{obs} to be inverse proportional to the respective beam velocities v_{ref}

and v_{obs}, as with increasing beam velocity each passing atom spends less time inside the probe beam during which it can contribute to the total fluorescence.

It follows from the above, that an atom beam with unknown flux φ and R_{obs}, $\mathrm{v}_{\mathrm{obs}}$ and P_{obs} known from experimental observation, relates to the reference beam with known φ_{ref}, R_{ref}, v_{ref} and P_{ref} according to

$$\frac{\varphi}{R_{\mathrm{obs}}}\frac{P_{\mathrm{obs}}}{v_{\mathrm{obs}}} = \frac{\varphi_{\mathrm{ref}}}{R_{\mathrm{ref}}}\frac{P_{\mathrm{ref}}}{v_{\mathrm{ref}}} . \tag{3.9}$$

Thus, we are able to deduce the atom flux φ via

$$\varphi = \frac{R_{\mathrm{obs}}}{R_{\mathrm{ref}}}\frac{P_{\mathrm{ref}}}{P_{\mathrm{obs}}}\frac{v_{\mathrm{obs}}}{v_{\mathrm{ref}}}\varphi_{\mathrm{ref}} . \tag{3.10}$$

3.4.5 Phase space density

Methods for the manipulation of ultra-cold atom samples are often compared in terms of the respective impact on the sample's phase space density (PSD). We derive an expression for the phase space density ρ at the centre of the atom beam that allows us to determine ρ using the experimental observables T_{r}, T_{a}, v_{b}, and φ, whose measurement has been discussed earlier in the preceding sections of this chapter.

For an atom beam that is guided inside a magnetic quadrupole field ρ can be expressed in terms of the thermal de Broglie wavelength λ_{B} and the on axis atom density n_0 [113]. At a temperature T, the phase space density is given by

$$\rho = n_0\,\lambda_{\mathrm{B}}^3 , \tag{3.11}$$

with

$$\lambda_{\mathrm{B}} = \left(\frac{2\pi\hbar^2}{m\,k_{\mathrm{B}}\,T}\right)^{1/2} . \tag{3.12}$$

The atom density n_0 follows from the lateral density $n(x,y)$ defined in equation (3.3) via $n_0 = n(0)$. With the axial density $\tilde{n}$ expressed as $\tilde{n} = \varphi v_{\mathrm{b}}^{-1}$. The atom beam in our experiment is described by two different temperatures T_{a} and T_{r}. There are, accordingly, two different thermal de Broglie wavelengths λ_{Ba} and λ_{Br} that are obtained by inserting T_{r} and T_{a} into equation (3.12), respectively. In order to obtain an expression for ρ from equation (3.11) we set $\lambda_{\mathrm{B}}^3 = \lambda_{\mathrm{Ba}}\lambda_{\mathrm{Br}}^2$, which yields

$$\rho = \frac{1}{2\pi}\frac{\varphi}{v_{\mathrm{b}}}\left(\frac{m_{\mathrm{J}}g_{\mathrm{J}}\mu_{\mathrm{B}}b_{\mathrm{g}}}{k_{\mathrm{B}}T_{\mathrm{r}}}\right)^2\left(\frac{2\pi\hbar^2}{mk_{\mathrm{B}}\left(T_{\mathrm{r}}^2T_{\mathrm{a}}\right)^{1/3}}\right)^{3/2} . \tag{3.13}$$

Purely magnetic potentials are conservative. Increasing PSD in a magnetically guided beam thus requires additional mechanisms such as dissipative light forces or evaporative cooling.

4 Continuous loading of an optical dipole trap

The capture of a moving atom by an optical dipole trap (ODT) requires, due to the conservative character of the ODT potential, that the excessive kinetic energy of the atom is removed. Typical atom velocities in the magnetic atom guide are on the order of few m/s, the amount of kinetic energy that needs to be dissipated therefore can exceed typical trap depths of an ODT by more than one order of magnitude. In this chapter we propose and analyse a loading method which employs deceleration by an additional magnetic field inside the ODT region and subsequent optical pumping to the energetically lowest Zeeman-sublevel. This process bears similarities to a single Sisyphus-cooling cycle [77, 114, 115, 116]. The feasibility and efficiency of this method is investigated by numerical simulations.

4.1 Principle of the ODT loading mechanism

In order to explain the transfer of atoms from the magnetic guide into an ODT we assume that the ODT is generated by a far red detuned Gaussian laser beam with focal waist w_0 and Rayleigh range z_R. We further assume that the optical axis of the beam coincides with the guide axis and that the focus is located at the origin of our coordinate system. For a total beam power P_0 the trap potential U_d of the ODT is then given by

$$U_\mathrm{d}(\mathbf{r}) = \frac{P_0\,\Phi_{|g\rangle}\,h}{w_0^2}\left(1+\frac{z^2}{z_\mathrm{R}^2}\right)^{-1}\exp\left(-\frac{2\rho^2}{w_0^2}\left(1+\frac{z^2}{z_\mathrm{R}^2}\right)^{-1}\right), \tag{4.1}$$

where h is Planck's constant and the parameter $\Phi_{|g\rangle}$, which describes the coupling between the trap beam and the trapped atom, is defined by equation (2.50). In the following, we regard ^{52}Cr ground state atoms trapped by a laser beam with 300 W total power, 1070 nm wavelength and a focal waist of 30 µm . For these settings equation (4.1) yields an optical trap depth of 3.6 mK.

From equation (4.1) it can be seen that the extension of the ODT in the axial direction is essentially marked by z_R and in the radial direction by w_0. An atom can be regarded as trapped inside the ODT when the sum of its kinetic energy and its potential energy is lower than the ODT potential threshold. In order to load an atom into the ODT we therefore require a process that does not only remove a sufficient amount of its initial kinetic energy. In addition, the removal has to take place in close proximity to the centre of the ODT.

Since only atoms that are in a low-field seeking Zeeman substate are transmitted inside the magnetic guide, an additional magnetic field can be used to generate a magnetic potential barrier inside the ODT that exerts a repulsive force on an atom approaching it from the guide. An atom that is decelerated by the barrier converts kinetic energy into potential energy up to the point where it either transcends the barrier or reaches a turning point of its trajectory. The position and orientation of the barrier with respect to the guide and the ODT have to

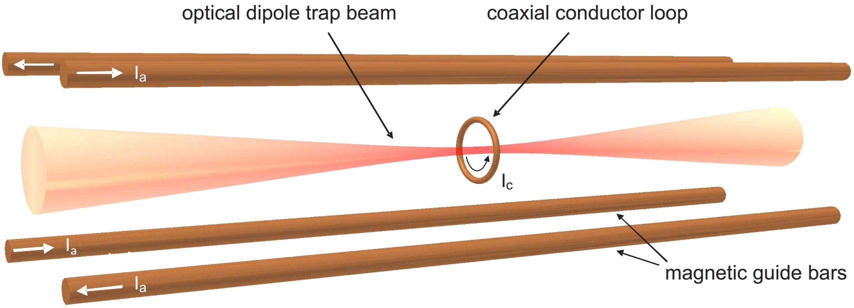

Figure 4.1: Illustration of the trap geometry we propose for continuous loading of an ODT from a magnetic guide. The current I_a that flows through the four bars in alternating directions generates a 2D magnetic quadrupole field which constitutes a magnetic guide for ultra-cold chromium atoms. The ODT is produced in the focus of an intense far red detuned laser beam that is coaxially aligned with the axis of the atom guide. Atoms approaching the centre of the ODT are decelerated by the magnetic field of a coaxial conductor loop that carries the current I_c.

be chosen such that this point of minimal axial kinetic energy lies as close as possible to the centre of the ODT. A fast optical pumping process can then be used to invert the orientation of the magnetic moment such that the decelerated atom is prepared with minimal kinetic energy in a high field seeking state. The formerly axially repulsive magnetic potential hence becomes attractive. The optical pumping process thus removes the potential energy that the atom has gained during the deceleration by the barrier. Depending on the amount of the remaining kinetic energy the atom would then be trapped in the combined potentials of the ODT and the magnetic field.

For our proposed loading scheme to be effective, it requires a suitable optical transition that allows the optical pumping to proceed both within a period much shorter than the average length of stay near the barrier peak and without causing excessive heating of the trapped atoms. For ^{52}Cr, a transition that fulfils these requirements is presented by the $^7\mathrm{S}_3 \longrightarrow {}^7\mathrm{P}_3$ transition, which is depicted in figure 2.1. The excited state has a lifetime of 33 ns. It decays with a branching ratio $> 10^3 : 1$ into the ground state. Figure 2.4 illustrates subsequent optical pumping cycles driving an atom from the $^7S_3$ $m_\mathrm{J} = +3$ to the $m_\mathrm{J} = -3$ level, the latter being a dark state. When σ^- light is used, on average 6.2 photons are scattered during a single pumping cycle, causing negligible recoil induced heating [117].

Figure 4.2 illustrates the loading scheme for ^{52}Cr. An atom in the $m_\mathrm{J} = +3$ sublevel of the $^7S_3$ ground state moves toward the ODT and is subsequently stopped at the centre of the ODT by the magnetic barrier superimposed with the ODT. At the point of return it enters a σ^--polarized pump laser beam that drives the atom quasi-instantaneously to the $m_\mathrm{J} = -3$

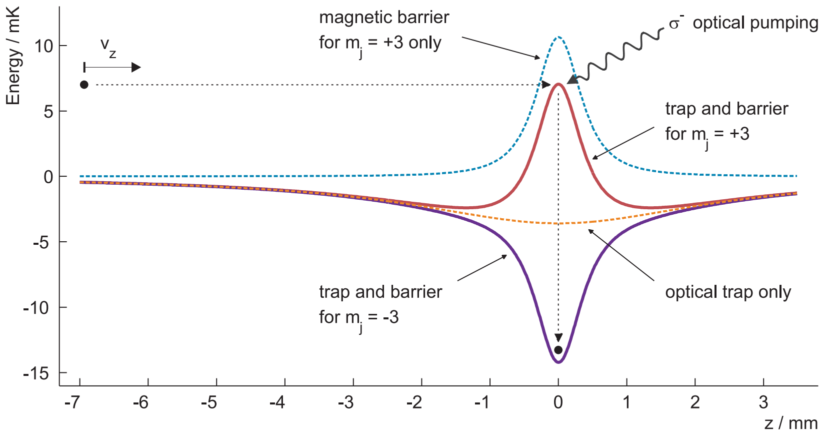

Figure 4.2: Illustration of the proposed scheme for continuously loading the ODT from the atom guide. A Cr atom in the low-field seeking $m_J = +3$ ground state approaches the centre of the ODT and is decelerated by a magnetic potential barrier. The atom thereby converts kinetic into potential energy. At the centre of the ODT, where the atom has minimised its kinetic energy, it enters a beam of σ^--polarized light, which pumps the atom to the high-field seeking $m_J = -3$ Zeeman sublevel. The pumping removes the gained potential energy and leaves the atom close to the bottom of a trap potential, which is generated by the ODT and the now attractive magnetic potential. Depending on the remaining kinetic energy, the atom remains trapped.

$^7S_3$ level. As a result, the atom is trapped by the ODT and the inverted magnetic potential.

4.2 Magnetic field configuration and trap potentials

During the preceding description of the loading scheme we have implicitly assumed the existence of a suitably shaped magnetic potential barrier. For a further analysis of the loading scheme the magnetic field configuration has to be specified in more detail. It has to be considered here, that the field $\mathbf{B}_\mathrm{m}$ that determines the shape of the potential barrier is in general a vector sum of the guide field $\mathbf{B}_\mathrm{a}$ and other additionally applied fields. An important requirement for $\mathbf{B}_\mathrm{m}$ is that its orientation has to be uniform inside the region where the optical pumping takes place in order to allow the preparation of purely σ^--polarized pump light. Moreover, while it is desirable to have a field whose strength increases steeply toward the ODT centre in axial direction, the curvature in radial direction has to be sufficiently small in order to avoid a defocusing effect on the atomic beam in either the low-field or the high-field seeking state.

A suitable magnetic field can be obtained by adding a single circular current loop positioned concentrically with respect to the ODT and the magnetic guide, as shown in figure 4.1. The magnetic field $\mathbf{B}_\mathrm{c}$ produced by the current loop near the centre of the loop, which coincides with the ODT centre, is in line with the guide axis. Starting from the centre it increases slowly

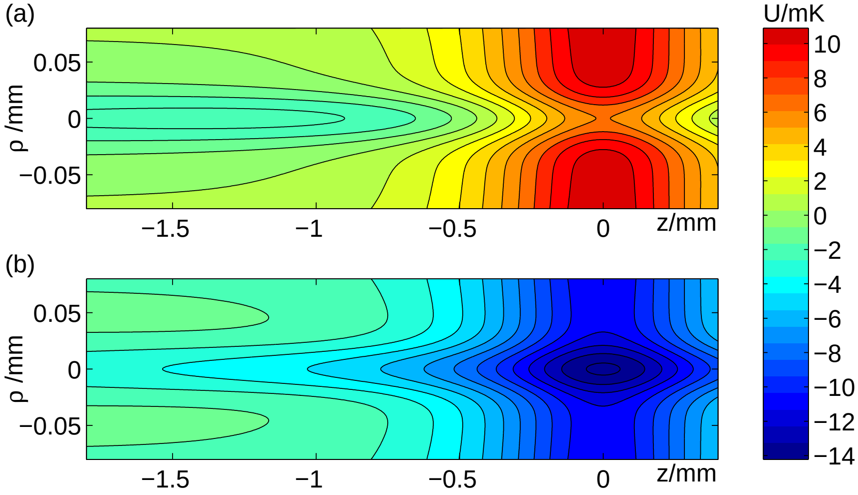

Figure 4.3: Colour coded contour plots of the combined potentials of the atom beam guide, the optical dipole trap and the deceleration loop. Values are calculated for $R = 0.5$ mm and $v_b = 1.5\,\mathrm{ms}^{-1}$. a) Potential for the low field seeking $m_J = +3$ state. The potential increases along the z-axis toward the origin. Atoms moving toward the origin are decelerated. The combined potentials of the guide and the ODT provide radial confinement. b) Potential for the high-field seeking $m_J = -3$ state, which is reached via optical pumping. Atoms can be trapped at the origin in a potential well formed by the ODT and the decelerating magnetic field.

in radial direction and decays on the length scale of the coil diameter in the axial direction. A general analytical expression for $\mathbf{B}_\mathrm{c}(\mathbf{r})$ can be given in terms of elliptical integrals [118]. Assuming the loop current I_c to be oriented positively with respect to the z-axis, $\mathbf{B}_\mathrm{c}$ is along the z-axis, for a loop radius R given by

$$\mathbf{B}_\mathrm{c}(z) = \frac{I_\mathrm{c}\mu_0}{2} \frac{R^2}{\left(R^2+z^2\right)^{3/2}} \mathbf{e}_z \,. \tag{4.2}$$

Having specified the magnetic field configuration we can express the potential U_0, in which the atoms move during the loading, in terms of the fields of $\mathbf{B}_\mathrm{a}$ and $\mathbf{B}_\mathrm{c}$ and the ODT potential U_d as

$$U_0 = \mu_\mathrm{B} g_J m_J |\mathbf{B}_\mathrm{a} + \mathbf{B}_\mathrm{c}| + U_\mathrm{d} \,. \tag{4.3}$$

The loop current has to be adjusted to the beam velocity v_b such that the total height of the potential barrier at the origin cancels the axial kinetic energy component of the arriving atoms. From equation (4.1) and (4.2) follows thus that I_c has to obey

$$\frac{m v_\mathrm{b}^2}{2} = \mu_\mathrm{B} g_J m_J \frac{I_\mathrm{c}\mu_0}{2R} + \frac{P_0\,\kappa h}{w_0^2} \tag{4.4}$$

The equations above relate the geometry of the ODT and of the atom guide with the decelerating current loop. They can be used to find optimised values for the interdependent parameters R and I_c. In a real experiment, however, there might be additional technical constraints that have to be considered. It might be difficult for example to work with extremely small coils and rather large current in an ultra high vacuum (UHV) environment. Moreover, it might be necessary to use the same coils with a range of beam velocities and an accordingly wide range of loop currents.

With the objective of providing useful guidance for the design of an experiment, we assume throughout this section a fixed loop radius of 0.5 mm and a magnetic field gradient of 350 Gcm^{-1}. From equation (4.4), it then follows that the coil current I_c depends only on the beam velocity v_b. In the following, we thus regard the magnetic barrier field and the resulting potential configuration as functions of v_b alone. For assumed beam velocities ranging from 1 m s^{-1} to 5 m s^{-1}, the loop has to carry currents between 1.3 A and 16.4 A. With technologies adapted from magnetic micro traps it should be feasible to operate a coil subject to these requirements [68].

Colour coded contour plots of total potential U_d in the xz-plane are shown in figure 4.3. An atom in the low-field seeking $m_\mathrm{J} = +3$ state experiences a potential barrier as shown figure 4.3 (a). In contrast, an atom in the high-field seeking $m_\mathrm{J} = -3$ state experiences a trap-shaped potential. In both cases the radial confinement is solely provided by the ODT. The depicted potentials correspond to a barrier height adjusted for a beam velocity of only 1.5 m s^{-1}. At higher velocities the magnetic barrier height becomes so large that the contribution from the ODT would be hardly recognisable.

4.3 Simulation of the loading process

In order to assess the feasibility and the efficiency of our proposed loading scheme we have numerically simulated the transfer of atoms from the guided atom beam into the ODT. For a given configuration of the atom beam and the trapping potential we are interested in the overall loading efficiency Λ, which we define as ratio between the fraction φ_L of the atomic flux that remains trapped in the ODT after optical pumping and the total incoming flux φ_0.

From our experimental studies we know that the radial and axial distributions of atomic velocities and positions inside the chromium atom beam typically resemble thermal distributions, which are, as outlined in section 3.4, well described by specifying the beam velocity v_b, the total flux φ_0, and the respective radial and axial beam temperatures T_r and T_z. Regarding the loading of the ODT, we restrict our studies to a potential configuration that depends only on v_b. Moreover, we make the important assumption that the densities in the atom guide and the ODT remain low enough such that inter-atomic collisions can be safely neglected during the loading process. It follows that, under these premises, Λ is density independent and can be regarded as a function of v_b, T_r and T_z alone.

Our simulations of the transfer of atoms from the atom guide into the ODT are based on the computation of a large number of individual atom trajectories and their subsequent analysis. For the computation of the trajectories we have used the expression for the total potential energy stated in equation (4.3) to obtain analytical expressions for the corresponding equations of motion. In the absence of collisions, we can for given initial conditions obtain the full 3D trajectories by numerically integrating the equations of motion on a personal computer using standard commercial mathematical software.

We then use the resulting trajectory to estimate a likely position and velocity of the atom when it undergoes the optical pumping [119]. For this purpose we require that the duration of the optical pumping process is negligibly short and that the pump beam is restricted to a narrow region near the top of the magnetic potential barrier. We then assume that as soon as the atom either has lost all its axial velocity ($v_b = 0$) or as soon as it reaches the maximum of the potential barrier ($z = 0$) it is pumped instantaneously into the high-field seeking state, where it is suddenly subject to an attractive potential. We regard the atom as successfully transferred into the ODT if the optical pumping process takes place inside the region of the final trap potential well and if the remaining total energy of the atom is lower than the trap potential threshold.

For the computation of the trajectories the atoms are all initialised at $z = -0.05\,\mathrm{m}$, which is chosen to be sufficiently far away from the ODT-centre, such that the initial potential energy distribution is only determined by the guide potential. For the initial radial distribution $n(\rho)$

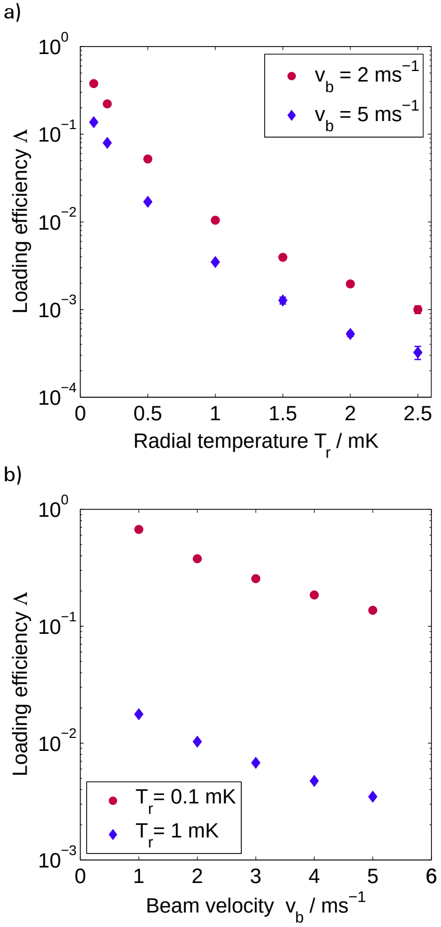

Figure 4.4: a) Calculated loading efficiency Λ as function of the initial radial temperature T_r of the atoms inside the guide. The velocities in the axial direction are assumed to be distributed according to a Maxwell-Boltzmann distribution with temperature $T_\mathrm{z} = 1$ mK offset by a beam velocity v_b of 2 m s^{-1} and 5 m s^{-1}, respectively. b) Loading efficiency as a function of the beam velocity for an axial temperature of 1 mK and values of the radial temperatures of 0.1 mK and 1 mK, respectively. A reduction of the beam velocity within range of 1 m s^{-1} to 5 m s^{-1} would only lead to a moderate enhancement of the loading efficiency.

follows from equation (3.3) by assuming $\tilde{n}=1$, which yields

$$n\left(\rho\right)=\rho\beta^{-2}\exp\left[-\frac{\rho}{\beta}\right], \tag{4.5}$$

where

$$\beta=\frac{k_{\mathrm{B}}T_{\mathrm{r}}}{\mu_{\mathrm{B}}g_{J}m_{J}\left|\nabla\left|\mathbf{B}_{\mathrm{a}}\right|\right|}. \tag{4.6}$$

The initial radial velocities v_x and v_y are distributed according to Maxwell-Boltzmann distributions with temperature T_{r}. The distribution $\nu(v_{\mathrm{z}})$ of the longitudinal velocities is described by a Maxwell-Boltzmann distribution with temperature T_{z} centred around the beam velocity v_{b}, yielding

$$\nu(v_{\mathrm{z}})=\sqrt{\frac{m}{2\pi k_{\mathrm{B}}T_{\mathrm{z}}}}\exp\left[-\frac{m\left(v_{\mathrm{z}}-v_{\mathrm{b}}\right)^{2}}{2k_{\mathrm{B}}T_{\mathrm{z}}}\right]. \tag{4.7}$$

In order to determine Λ we have at each instance calculated a large number of trajectories ($>5\cdot10^{4}$) with initial conditions randomly sampled according to the respective values of T_{r}, T_{z} and v_{b}. The number of successful transfers divided by the total number of trajectories then yields the corresponding value of Λ.

The results of our simulations are presented in figure 4.4. We have concentrated our studies on the dependence of Λ on the radial beam temperature (subfigure 4.4 (a) and on the beam velocity (subfigure 4.4 (b), respectively. With the objective to investigate the application of our loading scheme to a real experiment and to derive strategies for an optimisation of the loading rate, we have in both cases regarded parameter ranges that we deem to be experimentally accessible with present atom beam preparation methods [72, 101]. As T_{z} is typically roughly constant, we have used a, conservatively estimated, fixed value of $T_{\mathrm{z}}=1$ mK for the simulations presented in this chapter.

The dependence of Λ on T_{r} is shown in figure 4.4 (a). Two data sets are displayed, corresponding to two different beam velocities: $v_{\mathrm{b}}=2\,\mathrm{m\,s^{-1}}$ (red circles) and $v_{\mathrm{b}}=5\,\mathrm{m\,s^{-1}}$ (blue diamonds). The value of $2\,\mathrm{m\,s^{-1}}$ represents the minimal velocity at which the beam can be effectively operated, while at approximately $5\,\mathrm{m\,s^{-1}}$ the beam yields maximum atom flux [72]. Both data sets exhibit a steep increase of Λ with decreasing T_{r}. We attribute this to the energy initially stored in the transverse degrees of freedom, which cannot be dissipated with our loading scheme, and which contributes on average with $3\,\mathrm{k_{B}T_{r}}$ to the total energy remaining after optical pumping. The course of Λ as a function of T_{r} indicates that additional measures to decrease T_{r}, even if they are associated with a moderate reduction of φ_0, might be helpful in order to maximise the loading rate. At $T_{\mathrm{r}}=1$ mK, which represents the presently lowest values for the radial beam temperature [72], the graph yields $\Lambda=0.35\,\%$ for $v_{\mathrm{b}}=5\,\mathrm{m\,s^{-1}}$. Doppler cooling in the radial direction might, for instance, be used to reduce the radial temperature further to 0.125 mK, the Doppler temperature of chromium. In this case the loading efficiency would be expected to increase from 0.35 % to over 12 %.

From figure 4.4 (a) we can learn that for $v_{\mathrm{b}}=5\,\mathrm{m\,s^{-1}}$ the loading efficiency is about three times smaller than for $v_b = 2\,\mathrm{m\,s^{-1}}$. This can be explained by the different respective height of the magnetic potential barrier that is needed in order to decelerate the atoms. An increased barrier height results in an increased radial curvature and thus lowers the effective depth of the trapping potential. For this reason, our loading scheme can not be applied to arbitrarily high beam velocities. In figure 4.4 (b) the dependence of Λ on v_b is shown in more detail for two different radial temperatures, $T_r = 1\,\mathrm{mK}$ and $T_r = 0.1\,\mathrm{mK}$. The results from the simulations have to be contrasted with the experimentally observed dependence of the total flux φ_0 on v_b, which exhibits a pronounced maximum between $5\,\mathrm{m\,s^{-1}}$ and $6\,\mathrm{m\,s^{-1}}$ and a steep decrease toward slower beam velocities [72]. Regarding the optimisation of the loading rate, it appears to be evident that the decrease of φ_0 toward smaller beam velocities could possibly not be compensated by a corresponding increase of Λ. Thus it might not be advisable to reduce the beam velocity below $5\,\mathrm{m\,s^{-1}}$ at the expense of a greatly reduced total flux.

Based on the values of Λ and the reported values of φ_0 [72] we estimate for a beam velocity of $5\,\mathrm{m\,s^{-1}}$ and a radial temperature of 1 mK a loading rate of about $4 \cdot 10^6$ atoms/sec. We estimate that under these conditions it would take less than 1 s to reach a steady state with more than 10^6 atoms in the ODT. If at this point the loading process would be interrupted, this would already provide excellent starting conditions for the application of demagnetisation cooling [120]. This technique provides highly efficient cooling without loss of atoms and has shown to work best in dense and hot clouds that provide high collision rates and require easily controllable magnetic fields.

4.4 Conclusion

We have outlined a scheme for the transfer of ultra cold atoms from a magnetically guided atom beam into an optical dipole trap. The scheme compromises deceleration by a magnetic barrier superimposed with the ODT, followed by optical pumping to the energetically lowest Zeeman-sublevel. We have provided an elaborate discussion of the application of this scheme to a beam of ultra cold chromium atoms. The preparation of suitable potential field configurations for the deceleration and the trapping of the atoms have been treated. Using numerical simulations of the loading process have investigated the dependence of the loading efficiency on the initial radial beam temperature and on the beam velocity. Our simulations suggest that, based on recently reported experimental data [72], loading efficiencies of about 0.35 %, resulting in maximum loading rates of more than 10^6 atoms/sec, are feasible.

In the following chapter we demonstrate that by employing transverse laser cooling inside the magnetic guide the radial temperature of the atom beam can be further reduced, such that loading rates can be increased by an order of magnitude.

5 Laser cooling of a magnetically guided beam of ultra cold chromium atoms

This chapter presents the transverse cooling of a magnetically guided beam of ultra cold chromium atoms using a two-dimensional optical molasses. Our experiment differs in three respects from standard Doppler cooling of a free atom beam. First, the presence of a guide field splits the ground state into different Zeeman sub-states, which entails potential atom losses due to optical pumping from magnetically trapped into untrapped sub-states by the optical molasses beam. In order to suppress undesired optical pumping we therefore apply an additional magnetic offset field in the molasses region. Second, the beam that we intend to cool is already near the Doppler cooling limit. In order to enable effective cooling of the beam we use adiabatic compression by a tapering of the guide to increase the radial beam temperature before the beam enters the optical molasses. Third, the cooling is conducted on a beam that is magnetically confined in the radial direction, with the confining potential being affected by the magnetic offset field. In the following, we describe and discuss the implementation of our cooling method, its application to the atom beam and the resulting implications for the loading of a dipole trap from the beam.

5.1 Experimental implementation of the transverse cooling scheme

We conduct the transverse laser cooling of our guided ultra-cold atom beam by employing an optical molasses inside the tapered section of the guide, as illustrated by figure 5.1. The tapering is located at a distance of 0.75 m away from the MMMOT. It reduces the bar spacing from 46 mm to 9 mm, thus gradually increasing the magnetic field gradient over a distance of 100 mm from initially $13.5\,\mathrm{G\,cm^{-1}}$ to $355\,\mathrm{G\,cm^{-1}}$. The tapered section has a length of 50 mm, after which the spacing of the bars re-expands until the field gradient again reaches its original value of $13.5\,\mathrm{G\,cm^{-1}}$.

The purpose of the tapered section is to compress and, thereby, to adiabatically heat the beam before it enters the optical molasses. The optical molasses is oriented perpendicularly to the atom beam. It is generated by two pairs of retro-reflected laser beams, which both are linearly polarised in a lin || lin configuration with polarisation perpendicular to the atom beam axis, as shown in figure 5.1. The beam intensities are, within the limits of a retro reflected configuration, approximately equal. In the following, we will usually quote the peak intensity I_L of a single molasses beam. The molasses beams have identical elliptical beam profiles with respective beam waists of 13.1 mm along the guide axis and 2.5 mm perpendicular to it. An axially elongated beam profile has been chosen in order to maximise the distance over which the atom beam is illuminated, and thus the number of photons that can be scattered by an atom for a given beam intensity during its passage through the molasses beam.

The optical molasses is operated on the ${}^7\mathrm{S}_3 \longrightarrow {}^7\mathrm{P}_4$ transition of ${}^{52}\mathrm{Cr}$ at 426 nm, which is a

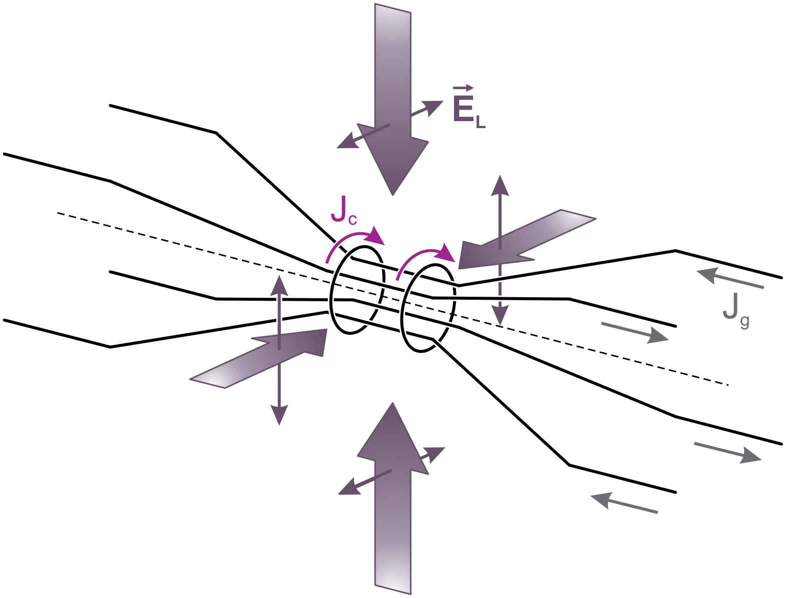

Figure 5.1: Schematic illustration (unscaled) of the optical molasses employed for transverse cooling of the atom beam in a tapered section of the magnetic atom beam guide. The current J_g, which flows in alternating opposing direction through the guide bars, generates a confining magnetic field, in which atoms are guided along central axis of the guide (dotted line). The tapering decreases the spacing between the guide bars from 46 mm to 9 mm, which results in compression and adiabatic heating of the passing atom beam. A two-dimensional optical molasses is formed by two pairs of counter propagating laser beams, which are indicated by flat arrows. The beams are linearly polarised in a lin || lin configuration with polarisation perpendicular to the axis of the guide. The optical molasses operates on the main ^{52}Cr cooling transition at a wavelength of 426 nm. A pair of coils in the centre of the tapered section, carrying a current J_c, provides a magnetic offset field in order to suppress optical pumping to untrapped states in the optical molasses.

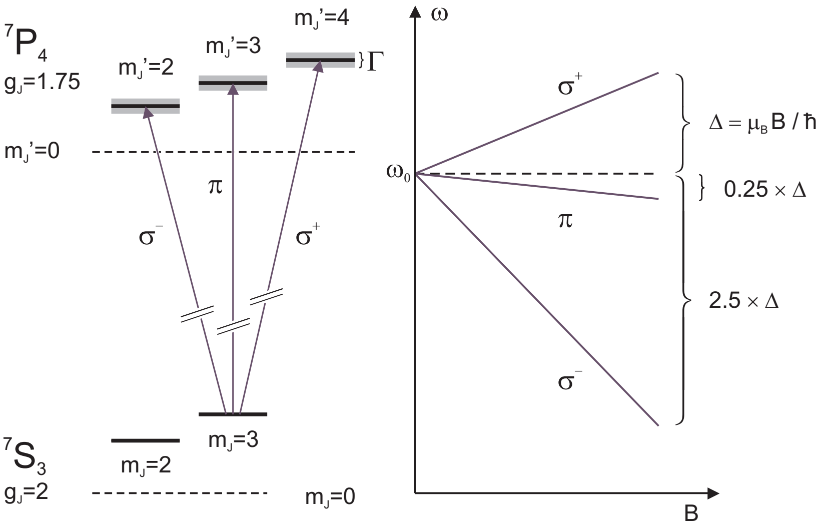

Figure 5.2: Selected Zeeman line shifts induced by an offset field B_0 for the $^7S_3 \longrightarrow {}^7P_4$ transition in ^{52}Cr that are used for the transverse cooling of the atom beam. The σ^+ transition from the $m_J = +3$ to the $m_J' = +4$ experiences a positive shift $\Delta = \mu_B B_0 \hbar^{-1}$, which amounts to $0.28\,\Gamma G^{-1}$. The corresponding σ^- and π transitions, on the contrary, experience negative shifts of -2.5 Δ and -0.25 Δ, respectively. This allows to perform Doppler cooling on the closed σ^+ transition exclusively by applying a sufficiently strong offset field B_0.

practically closed transition that is also employed for the MMMOT. It has a line width Γ of $2\pi \times 5$ MHz and a saturation intensity I_S of 8.5 mW cm^{-2}. From equation 2.9 it can be seen that only atoms with $m_J > 0$ can be confined by the magnetic field of the atom guided. In order to prevent atom losses in the optical molasses, it would therefore be desirable to scatter predominantly σ^+-polarised photons. Due to the presence of the guide field, it is, however, not possible to prepare the molasses beam in a purely σ^+-polarised state. Instead, we can employ a magnetic offset field B_0 to split the Zeeman lines far enough apart such they can be selectively addressed.

Figure 5.2 illustrates the Zeeman line shift of transitions from the $m_J = +3$ ground state. Due to a lower Landé factor of $g_J = 1.75$ in the upper level, the σ^+-transition experiences a positive shift towards higher frequencies, whereas the σ^- and π-transitions experience negative shifts. Provided that the splitting is sufficiently strong it is thus possible to tune the molasses beam near-resonant with the σ^+ and off-resonant with both σ^- and π-transitions.

The offset field is produced by a coaxial pair of identical copper coils that carry the current J_c with equal orientation. The coils are positioned concentrically with the beam axis around the centre of the tapered region, as shown in figure 5.1. The coils have an inner diameter of

42 mm and an inner spacing of 22 mm at a coil length of 15 mm. The coils thus approximate a Helmholtz coil pair configuration. We therefore regard the offset field experienced by the atoms in the optical molasses to be uniform and perpendicular to the guide field.

5.2 Experimental observation of transverse laser cooling

Our studies of the cooling with the optical molasses are based on the characterisation of the beam in terms of the total atom flux φ, the radial and axial beam temperatures T_a and T_r. The methods that we have adopted for the measurement of these beam properties are described in section 3.4. They rely on the illumination of the beam with a near resonant probe beam of known intensity and the imaging of the scattered photons with a calibrated CCD-Camera. Since the four optical molasses beams occupy a large fraction of the optical access to the tapered section of the guide, we have performed our measurement on the decompressed beam at a succeeding section of the guide, where the magnetic guiding potential is equal to the uncompressed initial potential.

5.2.1 Laser cooling with magnetic offset field

Figure 5.3 (a) presents the results from a measurement of the radial temperature as a function of the offset field B_0 and the molasses detuning δ. The beam has an initial radial temperature of 230 µK at a beam velocity of $5.2\,\mathrm{m\,s^{-1}}$. The intensity of the molasses beam was set to $I_\mathrm{L} = 0.3\,\mathrm{I_S}$. The observed temperatures are represented by a colour coded temperature map that has been obtained from interpolation between individual measurements. It can be seen that effective cooling below the initial temperature can only be achieved inside a wedge shaped region of the plot. The slopes of its borders closely match the respective Zeeman shifts of the σ^+ and π transition from the $m_\mathrm{J} = +3$ state, which are given in figure 5.2. This indicates that the magnetic offset field plays a vital role in the cooling process. Without magnetic field, the Zeeman-levels are degenerated and no cooling can be observed.

At a field of about 4.1 G, an optimal value δ_min of the detuning can be found that yields a minimum final temperature T_min of 62 µK . At this detuning the molasses is slightly red-detuned relative to the σ^+-transition ($\approx -1\,\Gamma$) [1]. For higher values of δ, the molasses beam becomes blue-detuned, which results in heating of the atom beam. Toward lower detunings, the beam becomes eventually near-resonant and blue-detuned with the π transition, which again leads to heating. When the magnetic field is increased further above 4.1 G we observe that the cooling becomes less efficient, resulting in higher final temperatures. This behaviour is caused directly by offset field, as it reduces the radial compression in the tapered section of the guide. This reduces the cooling due to the decompression after the optical molasses.

For each data point in figure 5.3 (a) we have also recorded the corresponding atom flux φ and axial temperature T_a, as explained in section 3.4.4 and 3.4.3, respectively. This allows us

---

[1] It should be noted here, that, while we can control the molasses beam frequency with a precision much better than the atomic line width Γ, we can only achieve an absolute frequency accuracy of about $0.5\,\Gamma$.

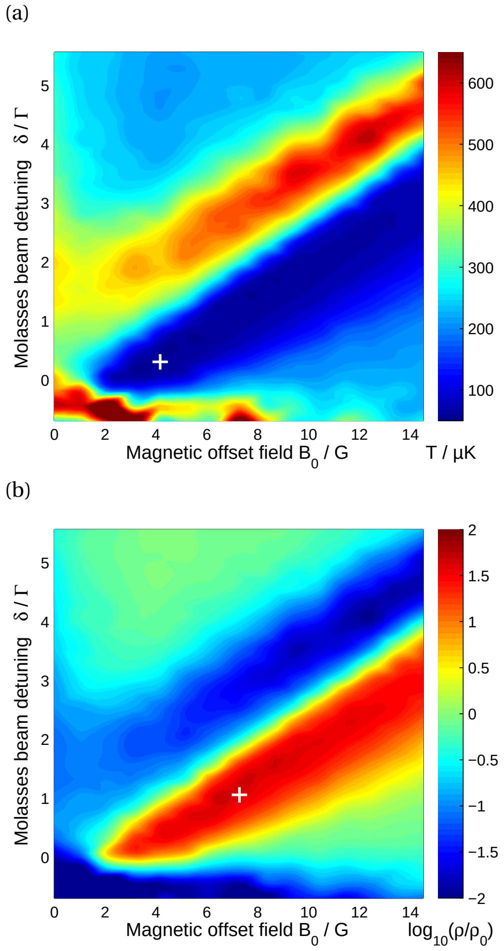

Figure 5.3: (a) Colour coded contour plot of the radial temperature of the decompressed beam after passing the tapered optical molasses section. The temperature has been recorded as function of the magnetic offset field and of molasses beam the detuning at a beam velocity of $5.2\,\mathrm{m\,s^{-1}}$ and a peak molasses beam intensity of $0.3\,I_S$. The white cross indicates the minimal radial temperature of $62\,\mu\mathrm{K}$, which has been observed for an initial temperature of $230\,\mu\mathrm{K}$. (b) Associated gain in phase space density (ρ/ρ_0) obtained by including atom flux and axial temperature data. A maximum gain of more than a factor 40 can be observed (white cross). The minimum temperature value on the left corresponds to a gain of a factor 30.

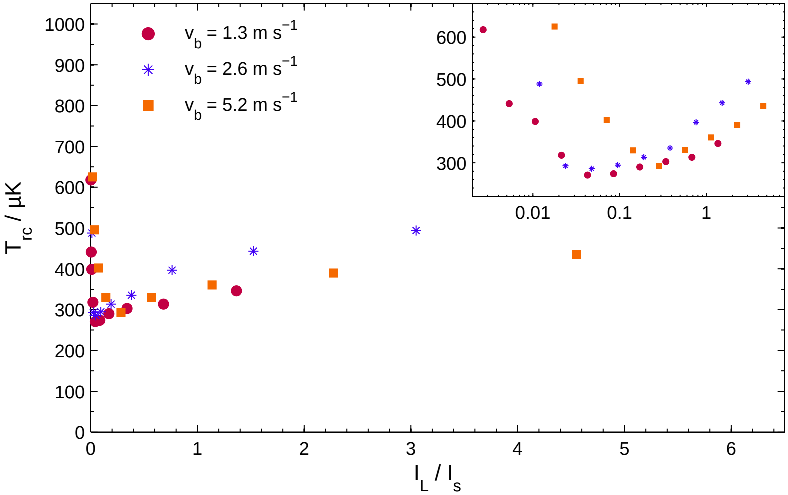

Figure 5.4: Temperature T_{rc} of the compressed atom beam over molasses beam intensity for three distinct beam velocities v_{b}. The inset displays the same data with a logarithmic intensity axes. For low intensities $I_{\mathrm{L}} < I_{\mathrm{S}}$ the beam temperature is velocity dependent and has thus not reached a steady-state during the time of passage through the optical molasses. For $I_{\mathrm{L}} \geq I_{\mathrm{S}}$ a linear increase of the final temperature due to saturation effects can be observed. The minimum observed temperature is more than two times higher than the Doppler cooling limit of an unconfined Cr atom cloud.

to deduce the associated phase space density ρ of the beam according to equation (3.13), which reads

$$\rho = \frac{1}{2\pi}\frac{\varphi}{v_{\mathrm{b}}}\left(\frac{\mu b_{\mathrm{g}}}{k_{\mathrm{B}}T_{\mathrm{r}}}\right)^2\left(\frac{2\pi\hbar^2}{m\,k_{\mathrm{B}}\,(T_{\mathrm{r}}T_{\mathrm{a}})^{1/3}}\right)^{3/2}. \tag{5.1}$$

Here m denotes the atomic mass, μ the atomic magnetic moment and k_{B} the Boltzmann constant. In figure 5.3 (a) the gain in phase space density compared to its initial value ρ_0 is presented. The gain in phase space density coincides well with the cooling of the beam. For the minimum temperature in figure 5.3 (a) we observe a gain of more than a factor 30, which yields a final phase space density of 3×10^{-8}.

Beside the molasses beam detuning and the offset field, the intensity I_{L} of the molasses beam is expected to have a significant influence on the cooling process. For low intensities, the duration of the passage through the optical molasses might be insufficient for the beam to reach a steady state temperature, which should then manifest itself as a strong intensity dependence of the final temperature. High intensities with $I_{\mathrm{L}} \geq I_{\mathrm{S}}$ might lead to a specific intensity dependence due to saturation effects [95].

5.2.2 Intensity dependence of the laser cooling process

In figure 5.4 we present the results from an investigation of the intensity dependence of the radial temperature at three different beam velocities. We conducted our measurements at a fixed magnetic offset field of 23.4 G. The molasses beams had a detuning relative to the Zeeman shifted σ^+ line of $-1.25\,\Gamma$, which for the chosen offset field corresponds to a detuning of about $+7\,\Gamma$ to the π transition.

Regarding the temperature values presented in figure 5.4 it should be noted that they refer the temperature T_{rc} of the compressed beam inside the tapered section of the guide, in contrast to the values given in figure 5.3, which reflect the temperatures of the uncompressed beam inside the detection chamber. They values for T_{rc} have been deduced from the measured uncompressed temperature values via a conversion that is based on numerical simulations of the decompression process. For this purpose we have calculated a large number of atom trajectories with initial values randomly sampled according to a thermal distribution very similar to the numerical simulation for the loading of the ODT that are outlined in section 4.3.

From figure 5.4 it can be seen that for the lowest intensities in the plot, the final temperature decreases with increasing intensity. In addition, lower beam velocities, which are equivalent to a higher number of scattered photons, lead, for the same intensity, to lower final temperatures. Both observations combined provide firm evidence that in the case of the two lowest velocities for $I_{\mathrm{l}} \lesssim 0.04\,I_{\mathrm{s}}$ and in the case of $v_{\mathrm{b}} = 5.2\ \mathrm{ms}^{-1}$ for $I_{\mathrm{l}} \lesssim 0.2\,I_{\mathrm{s}}$ the atom beam does not reach a steady state. When the intensity is increased above these values, we find that the final temperatures do not further decrease. At the same time, we observe that the temperature curves for all regarded beam velocities begin to coincide. We interpret this as a strong indication that the beam has entered a steady state regime.

Finally, for intensities exceeding $0.5\,I_{\mathrm{s}}$, the radial temperature increases approximately linearly with the beam intensity, which we attribute to the beginning saturation of the cooling transition [95]. The minimum final temperature of about 270 μK considerably higher than the Doppler limit 125 μK , that would be expected for an optical molasses. We suppose that this might be due to the presence of the strong magnetic field gradient in the tapered section, which is more than 25 times higher than the typical magnetic field gradients in a chromium MOT.

5.3 Conclusion

A method for the transverse cooling of a magnetically guided atom beam has been presented. We have demonstrated that by magnetic compression followed by transverse Doppler cooling in an optical molasses and subsequent decompression can be employed to increase the phase space density of an ultra cold atom beam resulting in final temperatures below the Doppler cooling limit. Our results are directly applicable to the loading of an optical dipole trap as suggested in [121]. For an experimentally realised beam with a final radial temperature of

63 µK , a beam velocity of 1.2 ms^{-1} and a longitudinal temperature of 250 µK , we estimate based on [121] a loading efficiency of more than 5 %, corresponding to a loading rate of over 10^7 atoms s^{-1}. Compared to the typical production rate of chromium atoms in Cr-BEC [52], which is 3×10^3 atoms s^{-1} this would provide an excellent starting point for a significant improvement of the Cr-BEC production rate.

6 Summary and outlook

Over the past century the development of atomic physics has been strongly intertwined with the development of atomic beam sources in the direction of an extended available range and a tighter control of internal and external atomic states. Today, quantum degenerate atom beam sources, which contain macroscopic numbers of atoms in the same quantum state, both reside at and extend beyond the outermost frontier of our technical capabilities and conceptual understanding. In particular, the realisation of a truly continuous atom laser, remains, over fifteen years after the demonstration of the first pulsed atom laser through outcoupling from a BEC, still a formidable scientific challenge.

Slow and intense guided beams of ultra cold atoms, which are obtained by the transfer of atoms out of a MOT into a magnetic atom guide, have in recent years been investigated as promising bases from which a continuous atom laser might be reached, either via evaporative cooling inside the guide or via the pumping of a perpetuated large BEC that could serve as an atom laser reservoir. Both pathways would benefit from atom beam sources capable of providing large numbers of atoms at a high phase space density.

In this thesis we have examined two problems that concern the efficient transfer of ultra cold atoms from a magnetically guided atom beam into an optical dipole trap, which might be employed for high throughput and even continuous BEC production. The first problem was posed by the capture of atoms by the ODT, which requires the dissipation of their kinetic energies in a way that permits the accumulation of a large number atoms inside the ODT. The second problem arose from the requirement to modify an existing chromium atom beam apparatus such that the transverse beam temperature is reduced substantially below the temperature of the MOT, from which the atom beam is generated. This requirement became apparent as a result from the assessment of the first problem.

In regard to the first problem we have proposed a loading scheme that dissipates the directed kinetic energy of a captured atom via deceleration by a magnetic potential barrier followed by optical pumping to the energetically lowest Zeeman sublevel. The proposal includes a detailed specification of a suitable magnetic barrier field that complies with realistically assumed experimental constraints. In order to assess the applicability of the loading scheme, we have performed numerical simulations of the loading process by calculating large numbers of trajectories of atoms propagating in the potential that arises from the combined magnetic and the optical fields of the guide, the potential barrier and the ODT. The obtained trajectories allowed us to deduce the loading efficiency Λ for a representative range of atom beam velocities and temperatures. We could show that the efficiency of the loading process does not prohibitively decrease with increasing beam velocity, which means that our scheme is capable of dissipating kinetic energies that are much larger than the total depth of the ODT. We found, however, that the loading efficiency is strongly linked to the radial temperature of the initial atom beam. It became evident that in order to obtain appreciable transfer rates the radial temperature atom beam had to be reduced below MOT temperatures.

In order to address the resulting second problem we have, based on an existing magnetically guided chromium atom beam experiment, implemented a transverse laser cooling scheme that can be operated in a fully continuous manner inside the magnetic field of the guide. The approach that we have developed employs radial magnetic compression to adiabatically heat the atom beam. The resulting increase in radial temperature allows to extract heat from the atom beam by a two-dimensional transverse optical molasses, which is combined with a magnetic offset field in order to prevent atom losses via optical pumping into untrapped states. We have validated this approach through experimental studies. We were able to demonstrate that by a suitable choice of the magnetic offset field, the cooling beam intensity and detuning, atom losses and longitudinal heating can be avoided. After decompression of the cooled atom beam we observe final temperatures below 65 µK , with an associated increase of phase space density by more than a factor of 30.

The results obtained from both our theoretical and experimental studies allow us to draw conclusions about the feasibility of the loading of an ODT from a magnetically guided atom beam. For an atom beam with a final radial temperature of 63 µK , a beam velocity of $1.2\,\mathrm{m\,s^{-1}}$ and a longitudinal temperature of 250 µK , we can expect a loading efficiency of more than 5 %, which would corresponding to a loading rate of over 10^7 atoms $\mathrm{s^{-1}}$. Compared to the typical production rate of chromium atoms in Cr-BEC [52], which is 3×10^3 atoms $\mathrm{s^{-1}}$ this would provide an excellent starting point for a significant improvement of the Cr-BEC production rate. It has to be noted here, that a recently published experiment succeeded in implementing the proposed loading scheme [122]. It has found a striking agreement between the predicted and the observed loading rates.

One open question is the optimal use of the high loading rate we now can achieve. Future experiments may exploit the high loading rate in ODTs, for example, in order to create extremely large chromium BECs. One promising direction to reach this goal is to further optimize geometries of the dipole trap to improve evaporative cooling and demagnetisation cooling, and to make full use of the loading rate we achieved.

An open question remains the generalisation of the transverse cooling scheme that we have used for chromium atoms to other atomic species. While evaporative cooling does not allow to reach a BEC with chromium in the magnetic guide, laser cooling of other atomic species may help to bring an atom beam into a state where evaporative cooling becomes feasible, opening further directions to a quantum degenerate atom beam.

Bibliography

[1] C. E. Wieman, D. E. Pritchard and D. J. Wineland. “Atom cooling, trapping, and quantum manipulation”. *Rev. Mod. Phys.* 71, S253–S262, 1999.

[2] R. Campargue, ed. *Atomic and molecular beams: the state of the art 2000*. Berlin: Springer, 2001.

[3] L. Dunoyer. “Sur la réalisation d’un rayonnement matériel d’origine purement thermique. Cinétique expérimentale”. *Le Radium* 8, pp. 142–146, 1911.

[4] W. Gaede. “Demonstration einer rotierenden Quecksilberluftpumpe”. *Phys. Z.* 6, pp. 758–760, 1905.

[5] O. Stern. “Zur Methode der Molekularstrahlen. I”. *Z. Phys. A: Hadrons Nucl.* 39, pp. 751–763, 1926.

[6] F. Knauer and O. Stern. “Zur Methode der Molekularstrahlen. II”. *Z. Phys. A: Hadrons Nucl.* 39, pp. 764–779, 1926.

[7] W. Gerlach and O. Stern. “Der experimentelle Nachweis der Richtungsquantelung im Magnetfeld”. *Z. Phys. A: Hadrons Nucl.* 9, pp. 349–352, 1922.

[8] W. Gerlach and O. Stern. “Das magnetische Moment des Silberatoms”. *Z. Phys. A: Hadrons Nucl.* 9, pp. 353–355, 1922.

[9] N. F. Ramsey. “Molecular beams: our legacy from Otto Stern”. *Z. Phys. D: At. Mol. Clusters* 10, pp. 121–125, 1988.

[10] I. I. Rabi, J. R. Zacharias, S. Millman and P. Kusch. “A New Method of Measuring Nuclear Magnetic Moment”. *Phys. Rev.* 53, pp. 318–318, 1938.

[11] I. I. Rabi, S. Millman, P. Kusch and J. R. Zacharias. “The Molecular Beam Resonance Method for Measuring Nuclear Magnetic Moments The Magnetic Moments of ${}_3\mathrm{Li}^6$, ${}_3\mathrm{Li}^7$ and ${}_9\mathrm{F}^{19}$”. *Phys. Rev.* 55, pp. 526–535, 1939.

[12] W. E. Lamb and R. C. Retherford. “Fine Structure of the Hydrogen Atom by a Microwave Method”. *Phys. Rev.* 72, pp. 241–243, 1947.

[13] P. Kusch and H. M. Foley. “The Magnetic Moment of the Electron”. *Phys. Rev.* 74, pp. 250–263, 1948.

[14] N. F. Ramsey. “A New Molecular Beam Resonance Method”. *Phys. Rev.* 76, pp. 996–996, 1949.

[15] L. Essen and J. V. Parry. “An Atomic Standard of Frequency and Time Interval: A Cæsium Resonator”. *Nature* 176, pp. 280–282, 1955.

[16] B. Guinot and E. Felicitas Arias. “Atomic time-keeping from 1955 to the present”. *Metrologia* 42, p. 20, 2005.

[17] J. P. Gordon, H. J. Zeiger and C. H. Townes. “Molecular Microwave Oscillator and New Hyperfine Structure in the Microwave Spectrum of NH_3”. *Phys. Rev.* 95, pp. 282–284, 1954.

[18] H. M. Goldenberg, D. Kleppner and N. F. Ramsey. “Atomic Hydrogen Maser”. *Phys. Rev. Lett.* 5, pp. 361–362, 1960.

[19] T. W. Hänsch, M. D. Levenson and A. L. Schawlow. “Complete Hyperfine Structure of a Molecular Iodine Line”. *Phys. Rev. Lett.* 26, pp. 946–949, 1971.

[20] C. Bordé. “Spectroscopie d’absorption saturée de diverses molécules au moyen des lasers à gaz carbonique et à protoxyde d’azot”. *C. R. Acad. Sci. Ser. B* 271, pp. 371–374, 1970.

[21] F. Biraben, B. Cagnac and G. Grynberg. “Experimental Evidence of Two-Photon Transition without Doppler Broadening”. *Phys. Rev. Lett.* 32, pp. 643–645, 1974.

[22] M. D. Levenson and N. Bloembergen. “Observation of Two-Photon Absorption without Doppler Broadening on the 3S-5S Transition in Sodium Vapor”. *Phys. Rev. Lett.* 32, pp. 645–648, 1974.

[23] T. W. Hänsch, K. C. Harvey, G. Meisel and A. L. Schawlow. “Two-photon spectroscopy of Na 3s-4d without Doppler broadening using a cw dye laser”. *Opt. Commun.* 11, pp. 50–53, 1974.

[24] C. Wieman and T. W. Hänsch. “Doppler-Free Laser Polarization Spectroscopy”. *Phys. Rev. Lett.* 36, pp. 1170–1173, 1976.

[25] J. L. Hall and C. Bordé. “Measurement of Methane Hyperfine Structure Using Laser Saturated Absorption”. *Phys. Rev. Lett.* 30, pp. 1101–1104, 1973.

[26] J. L. Hall, C. J. Bordé and K. Uehara. “Direct Optical Resolution of the Recoil Effect Using Saturated Absorption Spectroscopy”. *Phys. Rev. Lett.* 37, pp. 1339–1342, 1976.

[27] K. Uehara and J. L. Hall. “Hyperfine splitting of the $^{13}CH_4$ line at 3.39 µm observed by laser-saturated absorption”. *Opt. Lett.* 4, pp. 214–215, 1979.

[28] S. N. Bagayev, L. S. Vasilenko, V. G. Goldort, A. K. Dmitriyev, A. S. Dychkov and V. P. Chebotayev. “A tunable laser at λ=3.39 µm with line width of 7 Hz used in investigating a hyperfine structure of the $F_2^{(2)}$ line of methane”. *Applied Physics* 13, pp. 291–297, 1977.

[29] A. Ashkin. “Atomic-Beam Deflection by Resonance-Radiation Pressure”. *Phys. Rev. Lett.* 25, pp. 1321–1324, 1970.

[30] R. Schieder, H. Walther and L. Wöste. “Atomic beam deflection by the light of a tunable dye laser”. *Opt. Commun.* 5, pp. 337–340, 1972.

[31] J. E. Bjorkholm, R. R. Freeman, A. Ashkin and D. B. Pearson. “Observation of Focusing of Neutral Atoms by the Dipole Forces of Resonance-Radiation Pressure”. *Phys. Rev. Lett.* 41, pp. 1361–1364, 1978.

[32] E. Arimondo, H. Lew and T. Oka. “Deflection of a Na beam by resonant standing-wave radiation”. *Phys. Rev. Lett.* 43, pp. 753–757, 1979.

[33] J.-L. Picqué and J.-L. Vialle. “Atomic-beam deflection and broadening by recoils due to photon absorption or emission”. *Opt. Commun.* 5, pp. 402–406, 1972.

[34] R. Frisch. “Experimenteller Nachweis des Einsteinschen Strahlungsrückstoßes”. *Z. Phys.* 86, pp. 42–48, 1933.

[35] J. V. Prodan, W. D. Phillips and H. Metcalf. “Laser Production of a Very Slow Monoenergetic Atomic Beam”. *Phys. Rev. Lett.* 49, pp. 1149–1153, 1982.

[36] J. Prodan, A. Migdall, W. D. Phillips, I. So, H. Metcalf and J. Dalibard. “Stopping atoms with laser light”. *Phys. Rev. Lett.* 54, pp. 992–995, 1985.

[37] W. Ertmer, R. Blatt, J. L. Hall and M. Zhu. “Laser Manipulation of Atomic Beam Velocities: Demonstration of Stopped Atoms and Velocity Reversal”. *Phys. Rev. Lett.* 54, pp. 996–999, 1985.

[38] D. J. Wineland, R. E. Drullinger and F. L. Walls. “Radiation-Pressure Cooling of Bound Resonant Absorbers”. *Phys. Rev. Lett.* 40, pp. 1639–1642, 1978.

[39] W. Neuhauser, M. Hohenstatt, P. Toschek and H. Dehmelt. “Optical-Sideband Cooling of Visible Atom Cloud Confined in Parabolic Well”. *Phys. Rev. Lett.* 41, pp. 233–236, 1978.

[40] S. Chu, L. Hollberg, J. E. Bjorkholm, A. Cable and A. Ashkin. “Three-dimensional viscous confinement and cooling of atoms by resonance radiation pressure”. *Phys. Rev. Lett.* 55, pp. 48–51, 1985.

[41] A. L. Migdall, W. D. Phillips, J. V. Prodan, T. H. Bergeman and H. J. Metcalf. “First observation of magnetically trapped neutral atoms”. *Phys. Rev. Lett.* 54, pp. 2596–2599, 1985.

[42] S. Chu, J. E. Bjorkholm, A. Ashkin and A. Cable. “Experimental Observation of Optically Trapped Atoms”. *Phys. Rev. Lett.* 57, pp. 314–317, 1986.

[43] E. L. Raab, M. Prentiss, A. Cable, S. Chu and D. E. Pritchard. “Trapping of neutral sodium atoms with radiation pressure”. *Phys. Rev. Lett.* 59, pp. 2631–2634, 1987.

[44] N. Masuhara, J. M. Doyle, J. C. Sandberg, D. Kleppner, T. J. Greytak, H. F. Hess and G. P. Kochanski. “Evaporative cooling of spin-polarized atomic hydrogen”. *Phys. Rev. Lett.* 61, pp. 935–938, 1988.

[45] H. Pauly. *Atom, Molecule, and Cluster Beams II : Cluster Beams, Fast and Slow Beams, Accessory Equipment and Applications*. Berlin: Springer, 2000. P. 374.

[46] Bose. “Plancks Gesetz und Lichtquantenhypothese”. *Z. Phys.* 26, pp. 178–181, 1924.

[47] A. Einstein. “Quantentheorie des einatomigen idealen Gases”. *Sitzungsber. Preuss. Akad. Wiss., Phys.-Math. Kl.* Pp. 261–267, 1924.

[48] A. Einstein. “Quantentheorie des einatomigen idealen Gases. Zweite Abhandlung”. *Sitzungsber. Preuss. Akad. Wiss., Phys.-Math. Kl.* Pp. 3–14, 1925.

[49] M. H. Anderson, J. R. Ensher, M. R. Matthews, C. E. Wieman and E. A. Cornell. “Observation of Bose-Einstein Condensation in a Dilute Atomic Vapor”. *Science* 269, pp. 198–201, 1995.

[50] K. B. Davis, M.-O. Mewes, M. R. Andrews, N. J. van Druten, D. S. Durfee, D. M. Kurn and W. Ketterle. “Bose-Einstein condensation in a gas of sodium atoms”. *Phys. Rev. Lett.* 75, pp. 3969–3973, 1995.

[51] T. Lahaye, C. Menotti, L. Santos, M. Lewenstein and T. Pfau. “The physics of dipolar bosonic quantum gases”. *Rep. Prog. Phys.* 72, p. 126401, 2009.

[52] A. Griesmaier, J. Werner, S. Hensler, J. Stuhler and T. Pfau. “Bose-Einstein Condensation of Chromium”. *Phys. Rev. Lett.* 94, p. 160401, 2005.

[53] A. Griesmaier, J. Stuhler and T. Pfau. “Production of a chromium Bose-Einstein condensate”. *Appl. Phys. B: Lasers Opt.* 82, pp. 211–216, 2006.

[54] J. Werner, A. Griesmaier, S. Hensler, J. Stuhler, T. Pfau, A. Simoni and E. Tiesinga. “Observation of Feshbach Resonances in an Ultracold Gas of ^{52}Cr”. *Phys. Rev. Lett.* 94, 183201, p. 183201, 2005.

[55] A. Griesmaier, J. Stuhler, T. Koch, M. Fattori, T. Pfau and S. Giovanazzi. “Comparing Contact and Dipolar Interactions in a Bose-Einstein Condensate”. *Phys. Rev. Lett.* 97, 250402, p. 250402, 2006.

[56] T. Koch, T. Lahaye, J. Metz, B. Fröhlich, A. Griesmaier and T. Pfau. “Stabilization of a purely dipolar quantum gas against collapse”. *Nat. Phys.* 4, pp. 218–222, 2008.

[57] T. Lahaye, J. Metz, B. Fröhlich, T. Koch, M. Meister, A. Griesmaier, T. Pfau, H. Saito, Y. Kawaguchi and M. Ueda. “d-Wave Collapse and Explosion of a Dipolar Bose-Einstein Condensate”. *Phys. Rev. Lett.* 101, 080401, p. 080401, 2008.

[58] T. Lahaye, T. Koch, B. Fröhlich, M. Fattori, J. Metz, A. Griesmaier, S. Giovanazzi and T. Pfau. “Strong dipolar effects in a quantum ferrofluid”. *Nature* 448, pp. 672–675, 2007.

[59] R. J. C. Spreuww, T. Pfau, U. Janicke and M. Wilkens. “Laser-like Scheme for Atomic-Matter Waves”. *Europhys. Lett.* 32, pp. 469–474, 1995.

[60] M. O. Mewes, M. R. Andrews, D. M. Kurn, D. S. Durfee, C. G. Townsend and W. Ketterle. “Output coupler for Bose-Einstein condensed atoms”. *Phys. Rev. Lett.* 78, pp. 582–585, 1997.

[61] B. P. Anderson and M. A. Kasevich. “Macroscopic quantum interference from atomic tunnel arrays”. *Science* 282, pp. 1686–1689, 1998.

[62] I. Bloch, T. Hansch and T. Esslinger. “Atom laser with a cw output coupler”. *Phys. Rev. Lett.* 82, pp. 3008–3011, 1999.

[63] E. W. Hagley, L. Deng, M. Kozuma, J. Wen, K. Helmerson, S. L. Rolston and W. D. Phillips. “A well-collimated quasi-continuous atom laser”. *Science* 283, pp. 1706–1709, 1999.

[64] G. Cennini, G. Ritt, C. Geckeler and M. Weitz. “All-optical realization of an atom laser”. *Phys. Rev. Lett.* 91, p. 240408, 2003.

[65] H. Friedburg. “Optische Abbildung mit neutralen Atomen”. *Z. Phys.* 130, pp. 493–512, 1951.

[66] H. Friedburg and W. Paul. “Optische Abbildung mit neutralen Atomen”. *Naturwissenschaften* 38, pp. 159–160, 1951.

[67] E. A. Hinds and I. G. Hughes. “REVIEW ARTICLE: Magnetic atom optics: mirrors, guides, traps, and chips for atoms”. *J. Phys. D: Appl. Phys.* 32, p. 119, 1999.

[68] J. Fortagh and C. Zimmermann. “Magnetic microtraps for ultracold atoms”. *Rev. Mod. Phys.* 79, pp. 235–289, 2007.

[69] B. K. Teo and G. Raithel. “Loading mechanism for atomic guides”. *Phys. Rev. A: At. Mol. Opt. Phys.* 63, p. 031402, 2001.

[70] P. Cren, C. F. Roos, A. Aclan, J. Dalibard and D. Guery-Odelin. “Loading of a cold atomic beam into a magnetic guide”. *Eur. Phys. J. D* 20, pp. 107–116, 2002.

[71] T. Lahaye, J. M. Vogels, K. J. Gunter, Z. Wang, J. Dalibard and D. Guery-Odelin. “Realization of a magnetically guided atomic beam in the collisional regime”. *Phys. Rev. Lett.* 93, p. 093003, 2004.

[72] A. Griesmaier, A. Aghajani-Talesh, M. Falkenau, J. Sebastian, A. Greiner and T. Pfau. “A high flux of ultra-cold chromium atoms in a magnetic guide”. *J. Phys. B: At. Mol. Opt. Phys.* 42, p. 145306, 2009.

[73] E. Mandonnet, A. Minguzzi, R. Dum, I. Carusotto, Y. Castin and J. Dalibard. “Evaporative cooling of an atomic beam”. *Eur. Phys. J. D* 10, pp. 9–18, 2000.

[74] N. P. Robins, C. Figl, M. Jeppesen, G. R. Dennis and J. D. Close. “A pumped atom laser”. *Nat. Phys.* 4, pp. 731–736, 2008.

[75] A. P. Chikkatur, Y. Shin, A. E. Leanhardt, D. Kielpinski, E. Tsikata, T. L. Gustavson, D. E. Pritchard and W. Ketterle. “A Continuous Source of Bose-Einstein Condensed Atoms”. *Science* 296, pp. 2193–2195, 2002.

[76] H. Haken and H. C. Wolf. *Atom- und Quantenphysik*. 3rd. Berlin: Springer, 1987.

[77] H. J. Metcalf and P. v. Straten. *Laser cooling and trapping*. New York: Springer, 1999.

[78] C. J. Foot. *Atomic Physics*. Oxford University Press, 2006.

[79] W. Demtröder. *Laserspektroskopie*. 5th. Berlin: Springer, 2007.

[80] *CRC Handbook of Chemistry and Physics*. http://www.hbcpnetbase.com. CRC Press, Taylor & Francis Group.

[81] K. Heilig and D. Wendlandt. “Isotope shift in Cr I”. *Phys. Lett. A* A 25, p. 277, 1967.

[82] B. Furmann, A. Jarosz, D. Stefanska, J. Dembuynski and E. Stachowska. “Isotope shift in chromium”. *Spectrochim. Acta, Part B* 60, pp. 33–40, 2005.

[83] J. J. McClelland, R. E. Scholten, E. C. Palm and R. J. Celotta. “Laser-focused Atomic Deposition”. *Science* 262, pp. 877–880, 1993.

[84] R. E. Scholten, R. Gupta, J. J. McClelland, R. J. Celotta, M. S. Levenson and M. G. Vangel. “Laser collimation of a chromium beam”. *Phys. Rev. A: At. Mol. Opt. Phys.* 55, pp. 1331–1338, 1997.

[85] A. Bell, J. Stuhler, S. Locher, S. Hensler, J. Mlynek and T. Pfau. “A magneto-optical trap for chromium with population repumping via intercombination lines”. *Europhys. Lett.* 45, pp. 156–161, 1999.

[86] C. Bradley, J. McClelland, W. Anderson and R. Celotta. “Magneto-optical trapping of chromium atoms”. *Phys. Rev. A: At. Mol. Opt. Phys.* 61, p. 053407, 2000.

[87] W. Ketterle, D. S. Durfee and D. M. Stamper-Kurn. “Making, probing and understanding Bose-Einstein condensates”. *eprint arXiv:cond-mat/9904034*, 1999.

[88] W. Wing. “On neutral particle trapping in quasistatic electromagnetic fields”. *Prog. Quantum Electron.* 8, pp. 181–199, 1984.

[89] C. Doppler. “Ueber das farbige Licht der Doppelsterne und einiger anderer Gestirne des Himmels.” In: *Abh. der königl. böhm. Ges. der Wissenschaften*. Vol. Bd. 2. Folge V. 1842. Pp. 465–482.

[90] T. E. Barrett, S. W. Dapore-Schwartz, M. D. Ray and G. P. Lafyatis. “Slowing atoms with σ^{-} polarized light”. *Phys. Rev. Lett.* 67, pp. 3483–3486, 1991.

[91] A. Witte, T. Kisters, F. Riehle and J. Helmcke. “Laser cooling and deflection of a calcium atomic beam”. *J. Opt. Soc. Am. B: Opt. Phys.* 9, pp. 1030–1037, 1992.

[92] M. Walhout, H. J. Megens, A. Witte and S. L. Rolston. “Magneto-optical trapping of metastable xenon: Isotope-shift measurements”. *Phys. Rev. A: At. Mol. Opt. Phys.* 48, p. 879, 1993.

[93] T. W. Hänsch and A. L. Schawlow. “Cooling of gases by laser radiation”. *Opt. Commun.* 13, p. 68, 1975.

[94] D. Wineland and H. Dehmelt. “Proposed $10^{14}\Delta\upsilon < \upsilon$ Laser Fluorescence Spectroscopy on Ti+ Mono-Ion Oscillator III”. *Bull. Am. Phys. Soc.* 20, p. 637, 1975.

[95] P. Lett, W. Phillips, S. Rolston, C. Tanner, R. Watts and C. Westbrook. “Optical molasses”. *J. Opt. Soc. Am. B: Opt. Phys.* 6, pp. 2084–2107, 1989.

[96] H. Friedrich. *Theoretical Atomic Physics*. 3rd. Springer, 2006.

[97] R. Grimm, M. Weidemuller and Y. B. Ovchinnikov. “Optical dipole traps for neutral atoms”. In: *Adv. At. Mol. Opt. Phy.* Academic Press Inc., 2000.

[98] S. Hensler, J. Werner, A. Griesmaier, P. O. Schmidt, A. Görlitz, T. Pfau, S. Giovanazzi and K. Rzaewski. “Dipolar relaxation in an ultra-cold gas of magnetically trapped chromium atoms”. *Appl. Phys. B: Lasers Opt.* 77, pp. 765–772, 2003.

[99] S. Hassani. *Mathematical physics : a modern introduction to its foundations*. New York: Springer, 1999.

[100] The National Institute of Standards and Technology. *NIST Atomic Spectra Database*. http://physics.nist.gov/asd. The National Institute of Standards and Technology.

[101] A. Greiner, J. Sebastian, P. Rehme, A. Aghajani-Talesh, A. Griesmaier and T. Pfau. “Loading chromium atoms in a magnetic guide”. *J. Phys. B: At. Mol. Opt. Phys.* 40, F77–F84, 2007.

[102] A. Greiner. “Erzeugung eines lasergekühlten Atomstrahls in einem Magnetleiter : eine intensive Quelle für die Atomlithographie”. PhD thesis. Universität Stuttgart, 2008.

[103] R. Stützle. “Atomlithographie mit dissipativen Lichtmasken”. Diplomathesis. Universität Konstanz, Fachbereich Physik, 2001.

[104] T. W. Hansch and B. Couillaud. “Laser frequency stabilization by polarization spectroscopy of a reflecting reference cavity”. *Opt. Commun.* 35, pp. 441–444, 1980.

[105] D. de Oliveira Maionchi, W. Campos and J. Frejlich. “Angular alignment of a polarization-maintaining optical fiber”. *Opt. Eng.* 40, pp. 1260–1264, 2001.

[106] T. T. Aalto, M. Harjanne and M. Kapulainen. “Method for the rotational alignment of polarization-maintaining optical fibers and waveguides”. *Opt. Eng.* 42, pp. 2861–2867, 2003.

[107] P. Rehme. “Laden eines Wellenleiters mit lasergekühlten Chromatomen”. Diplomathesis. Universität Stuttgart, Fachbereich Physik, 2006.

[108] P. Christian. “Stabilisierung eines Lasersystems zur Laserkühlung von Chromatomen”. Diplomathesis. Universität Stuttgart, Fachbereich Physik, 2009.

[109] R. W. Drever, J. L. Hall, F. V. Kowalski, J. Hough, G. M. Ford, A. J. Munley and H. Ward. “Laser phase and frequency stabilization using an optical resonator”. *Appl. Phys. B: Lasers Opt.* 31, pp. 97–105, 1983.

[110] M. Meister. “Setup of a stable reference cavity for laser spectroscopy”. Diplomathesis. Universität Stuttgart, Fachbereich Physik, 2008.

[111] J. Stuhler. “Kontinuierliches Laden einer Magnetfalle mit lasergekühlten Chromatomen”. PhD thesis. Universität Konstanz, 2001.

[112] W. Nolting. *Grundkurs Theoretische Physik 6: Statistische Physik*. 6th. Berlin: Springer, 2007.

[113] T. Lahaye and D. Guéry-Odelin. “Kinetics of the evaporative cooling of an atomic beam”. *Phys. Rev. A: At. Mol. Opt. Phys.* 73, p. 063622, 2006.

[114] H. Gauck, M. Hartl, D. Schneble, H. Schnitzler, T. Pfau and J. Mlynek. “Quasi-2D gas of laser cooled atoms in a planar matter waveguide”. *Phys. Rev. Lett.* 81, pp. 5298–5301, 1998.

[115] A. Ruschhaupt and J. G. Muga. “Atom diode: A laser device for a unidirectional transmission of ground-state atoms”. *Phys. Rev. A: At. Mol. Opt. Phys.* 70, p. 061604, 2004.

[116] M. G. Raizen, A. M. Dudarev, Q. Niu and N. J. Fisch. “Compression of Atomic Phase Space Using an Asymmetric One-Way Barrier”. *Phys. Rev. Lett.* 94, 053003, p. 053003, 2005.

[117] A. Griesmaier. “Dipole-dipole interaction in a degenerate quantum gas: Bose-Einstein condensation of chromium atoms”. PhD thesis. Universität Stuttgart, 2006.

[118] G. Lehner. *Elektromagnetische Feldtheorie für Ingenieure und Physiker*. Berlin: Springer, 2008.

[119] W. L. Power, T. Pfau and M. Wilkens. “Loading atoms into a surface trap: simulations of an experimental scheme”. *Opt. Commun.* 143, pp. 125–132, 1997.

[120] M. Fattori, T. Koch, S. Goetz, A. Griesmaier, S. Hensler, J. Stuhler and T. Pfau. “Demagnetization cooling of a gas”. *Nat. Phys.* 2, pp. 765–768, 2006.

[121] A. Aghajani-Talesh, M. Falkenau, A. Griesmaier and T. Pfau. “A proposal for continuous loading of an optical dipole trap with magnetically guided ultra cold atoms”. *J. Phys. B: At. Mol. Opt. Phys.* 42, p. 245302, 2009.

[122] M. Falkenau, V. V. Volchkov, J. Rührig, A. Griesmaier and T. Pfau. “Continuous Loading of a Conservative Potential Trap from an Atomic Beam”. *Phys. Rev. Lett.* 106, 163002, p. 163002, 2011.